Simulation of Aircraft Aeroelasticity

Thesis submitted in accordance with the requirements of
the University of Liverpool for the degree of Doctor in Philosophy
by

Adam Swift

M.Eng.[Mechanical], Liverpool 2007

April 2011

Declaration

I confirm that the thesis is my own work, that I have not presented anyone else's work as my own and that full and appropriate acknowledgement has been given where reference has been made to the work of others.

……………………………………………………………

Adam Swift

April 2011

Abstract

Aeroelastic phenomena such as flutter can have a detrimental effect on aircraft performance and can lead to severe damage or destruction. Buffet leads to a reduced fatigue life and therefore higher operating costs and a limited performance envelope. As such the simulation of these aeroelastic phenomena is of utmost importance. Computational aeroelasticity couples computational fluid dynamics and computational structural dynamics solvers through the use of a transformation method. There have been interesting developments over the years towards more efficient methods for predicting the flutter boundaries based upon the stability of the system of equations.

This thesis investigates the influence of transformation methods on the flutter boundary predition and considers the simulation of shock-induced buffet of a transport wing. This involves testing a number of transformation methods for their effect on flutter boundaries for two test cases and verifying the flow solver for shock-induced buffet over an aerofoil. This will be followed by static aeroelastic calculations of an aeroelastic wing.

It is shown that the transformation methods have a significant effect on the predicted flutter boundary. Multiple transformation methods should be used to build confidence in the results obtained, and extrapolation should be avoided. CFD predictions are verified for buffet calculations and the mechanism behind shock-oscillation of the BGK No. 1 aerofoil is investigated. The use of steady calculations to assess if a case may be unsteady is considered. Finally the static aeroelastic response of the ARW-2 wing is calculated and compared against experimental results.

Acknowledgement

I would like to thank my supervisors Professor Ken Badcock and Professor George Barakos and all the members of the CFD lab, both past and present, at the University of Liverpool. It has been a privilege to work with you all.

I would like to thank the members of the R&T group at BAE Systems Warton for their support and encouragement that helped make my annual placements so productive. I am especially grateful to Mark Lucking for his guidance and support during these placements.

I would like to thank my family and friends for their their patience and support. I am especially grateful to Maryam for her unwavering love and patience.

I am grateful for the financial support of the Engineering and Physical Sciences Research Council (EPSRC) and BAE SYSTEMS through a case award. I would also like to extend my gratitude to the 2nd UK Applied Aerodynamics Consortium for providing computing time on HPCx and HECTOR.

Publications

"Computational Study of the BGK No. 1 Aerofoil Buffet", A. Swift and K.J. Badcock, submitted to the Aeronautical Journal.

"Investigation into the Effect of Transformation Methods on Flutter Boundary Predictions", A. Swift and K.J. Badcock, submitted to the Aeronautical Journal.

"Transonic Aeroelastic Simulation for Envelope Searches and Uncertainty Analysis", K.J. Badcock, S. Timme, S. Marques, H. Khodaparast, M. Pradina, J.E. Mottershead, A. Swift and A. Da Ronch, Progress in Aerospace Sciences (online), June 2011.

"Framework for Establishing the Limits of Tabular Aerodynamic Models for Flight Dynamics Analysis", M. Ghoreyshi, K. Badcock, A. Da Ronch, S. Marques, A. Swift and N. Ames, Journal of Aircraft, 48(1), 2011.

"Inter-grid Transfer Influence on Transonic Flutter Predictions", A. Swift and K. Badcock, AIAA-2010-3049, April 2010.

"Framework for Establishing the Limits of Tabular Aerodynamic Models for Flight Dynamics Analysis", M. Ghoreyshi, K. Badcock, A. Da Ronch, S. Marques, A. Swift and N. Ames, AIAA-2009-6273, August 2009.

Contents

List of Tables

List of Figures

Nomenclature

Acronyms	Definition
AGARD	The Advisory Group for Aerospace Research and Development.
AMB	Aeroelastic Multi-Block solver.
ARW-2	Aeroelastic Research Wing 2.
BEM	Boundary Element Method.
BGK	Bauer-Garabedian-Korn aerofoil.
BILU	Block Incomplete Lower-Upper factorisation.
BSM	Beam Stick Model.
CAE	Computational Aeroelasticity.
CFD	Computational Fluid Dynamics.
CFL	Courant-Friedrichs-Lewy number.
CPU	Central Processing Unit.
CSD	Computational Structural Dynamics.
CVT	Constant Volume Tetrahedron.
DAST	Drones for Aerodynamic and Structural Testing.
DES	Detached Eddy Simulation.
DNS	Direct Numerical Simulation.
DOF	Degrees of Freedom.
FFT	Fast Fourier Transform.
FPS	Finite Plate Splines.
GVT	Ground Vibration Test.
HIRENASD	High Reynolds Number Aero-Structural Dynamics.

IIM	Inverse Isoparametric Mapping.
IMQ	Inverse Multiquadrics.
IPS	Infinite Plate Splines.
LANTRIN	Low Altitude Navigation and Targeting Infrared for Night.
LCO	Limit Cycle Oscillation.
LES	Large Eddy Simulation.
LIF	Laser Induced Fluorescence.
MDO	Multi-Disciplinary Optimisation.
MQ	Multiquadrics.
MUSCL	Monotone Upstream-centred Schemes for Conservation Laws.
NAE	National Aeronautical Establishment (Canada).
NASA	National Aeronautics and Space Administration.
NUBS	Non-Uniform B-Spline.
NURBS	Non-Uniform Rational Basis Spline.
ONERA	Office National d'Études et de Recherches Aérospatiales (French aerospace research centre).
RANS	Reynolds Averaged Navier-Stokes.
RBF	Radial Basis Functions.
SDM	Standard Dynamics Model.
TDT	Transonic Dynamics Tunnel.
TFI	Transfinite Interpolation.
TPS	Thin Plate Splines.
URANS	Unsteady Reynolds Averaged Navier-Stokes.
USA	United States of America.

Symbols	**Definition**
$\dot{q}_x$, $\dot{q}_y$, $\dot{q}_z$	Heat fluxes.
$\dot{q}$	Rate of volumetric heat addition per unit mass.

ℓ, u_ℓ, τ_ℓ	Length, velocity and time scales.
$\mathbf{dx}$	Displacements.
$\mathbf{f_i}$	Blending functions.
$\mathbf{F}$	Forces.
$\mathbf{f}$	Time dependent external force vector.
$\mathbf{F}$, $\mathbf{G}$, $\mathbf{H}$	Flux vectors in the x, y amd z directions.
$\mathbf{p}$	Complex eigenvector.
$\mathbf{R}$	Vector of residuals.
$\mathbf{W}$	Solution vector of conserved variables.
$\mathbf{w}$	Vector of unknowns.
$\mathbf{X}$	Eigenvectors.
$\mathbf{x}$	Coordinates.
$\mathbf{x}$, $\dot{\mathbf{x}}$, $\ddot{\mathbf{x}}$	Time dependent displacement, velocity and acceleration vectors.
$\overline{f}$	Mean part of a flow variable.
$\tilde{f}$	Mass averaged flow variable.
C	Viscous damping matrix.
c	Chord.
C'_N	RMS values of the normal-force fluctuations.
C_k	Kolmogorov constant.
C_L	Lift coefficient.
c_p	Specific heat at constant pressure.
c_v	Specific heat at constant volume.
E	Total energy.
e	Specific internal energy.
$E(\kappa)$	Spectral distribution of energy.
f	Arbitrary flow variable.
f	Frequency.

f'	Fluctuating part of a flow variable.
f''	Fluctuating part of a flow variable.
f_i	Body forces.
H	Total enthalpy.
h	Specific internal enthalpy.
I	Identity matrix.
J	Jacobian.
K	Stiffness matrix.
k	Reduced frequency.
k	Specific turbulent kinetic energy.
k_{ij}	Edge spring stiffness.
k_x, k_y, k_z	Norm biasing coefficients.
L	Length.
M	Mass matrix.
M_η, C_η, K_η	Modal mass, damping and stiffness matrices.
n	Number of degrees of freedom.
$N_i(\xi, \eta)$	Shape functions.
p	Pressure.
$p(\mathbf{x})$	Linear polynomial.
Pr	Prandtl number.
Pr_T	Turbulent Prandtl number.
R	Rotation matrix.
R	Specific gas constant.
$r(\xi)$	Blending function.
r^2	Non-zero parameter for MQ.
Re	Reynolds number.
Re_T	Turbulent Reynolds number.
T	Temperature.

T	Transformation matrix.
t	Time.
T_0	Reference temperature = 288.16K.
T_p	Period of shock oscillation.
U	Velocity.
u, v, w	Velocity components in the x, y, z directions.
u_d	Speed of downstream pressure wave propagation.
u_u	Speed of upstream pressure wave propagation.
W	Virtual work.
x, y, z	Cartesian coordinates.
x_s	Time-mean shock position.
$\mathrm{s}(\mathbf{x})$	Interpolant.

Greek Symbols	**Definition**
α, β, γ	CVT constants.
α_i	Coefficients.
η, $\dot{\eta}$, $\ddot{\eta}$	Modal coordinate.
η, u_η, τ_η	Kolmogorov scales of length, velocity and time.
κ	Thermal conductivity.
κ	Wavenumber.
λ	Eigenvalues.
μ	Dynamic viscosity.
μ	Schur solver parameter (altitude).
μ_0	Reference viscosity = 1.7894×10^{-5}.
μ_T	Turbulent eddy viscosity.
ν	Kinematic viscosity.
Φ	Modal matrix.
Ψ	Displacement mapping to virtual surface.
ψ, ϕ, ω	Blending functions.

ρ	Density.
ρ	Support radius.
τ_{ij}	Shear Stresses.
τ_{ij}^R	Reynolds stresses.
ε	Rate of dissipation.
ξ, η, ζ	Local co-ordinate system.
$d\alpha$	Rotation about the beam.

Subscripts	**Definition**
∞	Freestream value.
f	Fluid.
ff	Fluid-fluid.
fs	Fluid-structure.
i	Inviscid.
i, j, k	Indices=1,2,3,. . . .
L	Laminar.
s	Structure.
sf	Structure-fluid.
ss	Structure-structure.
T	Turbulent.
v	Viscous.

Superscripts	**Definition**
$\hat{}$	Mapped quantity.
e	Indicates structural node is a member of that element.
n	Current time-step.
$n+1$	Next time-step.
R	Reynolds stress.
$*$	Dimensional variable.

Chapter 1

Introduction

1.1 Aeroelasticity

Aeroelasticity involves the interaction of aerodynamic, elastic and inertial forces. The subject can be traced back to before the first powered flight of the Wright Brothers. The Langley Monoplane that flew a few days before the Wright Brother's famous flight is suspected to have crashed due to aeroelastic divergence of the rear wing, which was insufficiently torsionally stiff [16]. The Wright Brothers used the flexibility in the wings of their aircraft to control roll and this concept was revisited for the NASA X-53 Active Aeroelastic Wing in 2004 that was based on the F/A-18 fighter jet. A brief history of the first fifty years of aeroelasticity was given by Collar [17]. The main areas of interest to aeroelasticians are the interaction of aerodynamic and elastic forces to form static aeroelasticity, and the interaction of all three forces to form dynamic aeroelasticity. This can be extended to include the effect of control systems, which gives rise to aeroservoelasticity, and the effect of heating (important for hypersonic applications) to give rise to aerothermoelasticity. Aeroelasticity is not solely concerned with aircraft (although the focus of this thesis), but effects the design of structures such as bridges (Tacoma Narrows Bridge for example), powerplant cooling towers, Formula 1 racing cars, wind turbines, turbomachinary etc.

Static aeroelasticity is the coupling between the aerodynamic and elastic forces and is time independent. Since an aircraft structure is flexible the aerodynamic loads will deform the aircraft structure, which in turn will change the aerodynamic loads acting on it. For static aeroelasticity the aerodynamic loads and the elastic restoring forces will come to an equilibrium and the resulting deformed shape will have an influence on the generated lift and drag. As such airframe manufacturers put significant work into designing the jig (or manufactured) shape of an aircraft so that at cruise the aircraft will deform into an optimised design shape. Avoiding errors in the jig shape is very important due to the large impact the jig shape has on the drag produced [18].

There are negative static aeroelastic effects that are of concern. These are divergence and control surface reversal. If a wing is assumed to have a finite torsional stiffness, a twist along the wing will be induced when an aerodynamic load is applied. For high torsional stiffness or low airspeed (a small aerodynamic load) this twist angle will be small. However as the airspeed increases, and therefore the aerodynamic load, so will the twist angle. At a critical speed the aerodynamic pitching moment exceeds the elastic restoring moment and the wing is twisted beyond its ultimate strength, leading to structural failure. This is the static aeroelastic phenomenon of divergence.

The aim of a control surface is to modify the lift or moment of the lifting surface. If the lifting surface is flexible then control surface reversal can occur. An example of this is if an aileron is deflected in order to achieve a certain roll rate, this will augment the lift on the outboard portion of the wing. If the wing is sufficiently stiff then this will be successful. However if the airspeed and therefore the aerodynamic loads are large enough the twisting of the wing will lead to a reduction of lift. Since this is opposite to the desired command the controls have effectively reversed. Near this critical speed the effect of the control surface and the twisting cancel leaving little control authority. Control surface reversal effected the Supermarine Spitfire during the Second World War, which could happen when the pilot tried to roll during a dive. The fighter had originally been designed for a control surface reversal speed of 580 mph, which during a dive could be exceeded. This resulted in the pilots rolling in the opposite direction than intended. This was later fixed by stiffening the wings to give it a theoretical control reversal speed of 825 mph.

Dynamic aeroelasticity is concerned with oscillatory and transient effects. There are four main dynamic aeroelastic phenomenon, which are flutter, limit cycle oscillation (LCO), control surface buzz and buffet.

Flutter is where two structural vibration modes couple in the aeroelastic system causing the structure to extract energy from the airflow, possibly leading to the destruction of the aircraft. The first recorded flutter incident was on a Handley Page O/400 twin engined biplane bomber in 1916. The mechanism was the coupling of the fuselage torsion mode and an antisymmetric elevator mode. Since the elevators were independently connected to the control stick the solution was to connect the elevators together using a torque tube [16]. Flutter can occur locally, for example panel flutter where an oscillating shockwave causes the structural panel below it to flutter. Control surface limit cycle oscillation leading to wing flutter is believed to be responsible for the crash of a F-117 stealth fighter at an airshow in Maryland, USA in 1997. This was found to be caused by four out of five fasteners missing in the left wing, this reduced the torsional stiffness of the elevator. The reduced torsional stiffness caused a limit cycle oscillation of the elevator, which caused the wing to flutter [19]. A history of flutter can be found in ref. [16].

Limit cycle oscillation is a type of flutter, which is a self sustaining limited amplitude oscillation with the amplitude limited due to non-linearities. Both the F-16 and F/A-18 have encountered limit cycle oscillations at high subsonic and transonic speeds for certain store configurations with AIM-9 missiles at the wing tips and heavy stores on the outboard pylons [20]. Limit cycle oscillations can damage stores, reduce their fatigue life and targeting effectiveness [20].

Control surface buzz is similar to limit cycle oscillation in that the amplitude of the oscillations are limited, however the mechanism behind it is different. It is caused by the interaction of a shock wave, boundary layer and control surface rotation mode. There are two main types of control surface buzz, the first is caused by buffet of the control surface by the separated flow due to shock-boundary layer interaction upstream and the second type is due to shock wave oscillation on the control surface itself with no separation involved.

Buffeting is defined as the structural response to the aerodynamic excitation produced by separated flows. Buffet can be caused by massive separation over a lifting surface (stall buffet), separation due to shock/boundary-layer interaction (Mach number buffet) or vortex breakdown. Related to buffet is transonic buffet (also refered to as shock buffet), this is an aerodynamic phenomenon in which a shockwave is generated over a lifting surface that interacts with the boundary-layer causing partially or fully separated flow. This results in a self-sustained oscillating flow field and occurs without structural motion, however the frequency of shock oscillation is usually in the range of the low-frequency modes of an elastic structure which would lead to buffeting.

One of the first records of buffet dates back to 21^{st} July 1930 where a commercial aeroplane crashed at Meopham, Kent. In this case the aircraft flew into a cloud and shortly afterwards came down in pieces, the subsequent investigation found that there was a strong updraft in the area. This caused the angle of attack to increase sharply leading to massive separation over the wing. The tail was situated in this region of highly unsteady separated flow and therefore subjected to intense forced vibrations that ultimately caused the tail to fail [21]. This accident was an example of stall buffet. A more modern example was on the American F-15 fighter jet caused by leading edge separation at angles of attack of over 22 degrees, which excited the first torsion mode [22]. In 1998 the cost of repairing and replacing F-15 vertical tails due to fatigue was estimated to be $5-6 million per year [4], in addition to the loss of flight readiness. This type of buffet is caused by the separation over wings, the F-16 had severe damage to ventral fins positioned at the underside of the rear fuselage caused by the upstream separation of the airflow over the LANTRIN targeting pods [4]. This is shown in the Figure 1.1 and the extensive damage to the ventral can be seen.


(a) F-16 with ventral fins and LANTRIN pod

(b) Ventral fin failure

Figure 1.1: F-16 ventral fin failure (from ref. [4])

Shock-induced boundary-layer separation causes an aerodynamic unsteadiness. At certain conditions this shockwave can exhibit self-excited oscillations along with separation and reattachment. This dynamic separation and reattachment excites the structure and in some cases can be severe enough to threaten the structural integrity of the aircraft. An example of this type of buffet is the Aeroelastic Research Wing (ARW-2) which exhibits shock boundary-layer interaction that leads to buffeting of the structure over a small region of Mach numbers [23]. During windtunnel tests, certain flow conditions could not be tested since the buffeting was so severe that the safety of the wing was not guaranteed.

The final type of buffet is caused by vortex breakdown, which has generated a large amount interest. This interest has been caused by the move to highly agile aircraft capable of performing high angle of attack maneuvers. At high angles of attack many modern aircraft feature high energy vortices generated by leading edge extensions, wing, canards etc. and these vortices can become unstable and burst. Once burst a wake of highly turbulent flow imparts unsteady loading to the tail of the aircraft that excites the structural modes of the aircraft component. This excitation is generally at low frequencies that match or are close to the first bending and torsion modes of the tail. The high dynamic response impacts the fatigue life and in rare cases threatens the structural safety of the component. The most researched aircraft that suffers from this type of buffet is the F/A-18. The vortices are generated by the leading edge extension and breakdown ahead of the vertical tails at angles of attack of 25° and higher [24] (see Figure 1.2) with the buffet loads on the vertical tail reaching 450g during test flights [25].

This type of buffet is very much an unsolved problem for modern fighter jets with the EF-2000 type fighter [26, 27], F-22 [28, 29] and the F-35 [30] suffering from different levels of buffet.

Dryden Flight Research Center EC89-0096-149 Photographed 1990
F-18 HARV flow-visualization smoke marks vortex flows
along the leading edge extension. NASA photo

Figure 1.2: Vortex breakdown over the F/A-18 (from ref. [5])

Buffet effects all aircraft, both civil and military, however the causes and flight regimes are different. Figure 1.3 gives a comparison of the flight envelope for the buffet criteria for a civil transport aircraft and a military fighter jet. Buffet is split into different levels of severity denoted as light, moderate and heavy. Civil aircraft are designed to cruise below buffet onset and maneuver to at least 1.3g without any buffeting [6]. It is allowed to enter the buffet region for short periods during rare severe gusts, but it should not create any structural or control issues. Military fighters fly much further below the buffet boundary, but for performance reasons will frequently maneuver deep inside the buffet region. This can lead to a significant reduction in the fatigue life of the aircraft [6].

Over the years many potential solutions to buffet have been proposed, the simplest being to limit the flight envelope. On the F/A-18, streamline fences were introduced on the upper surface of the leading edge extension to reduce the buffet loads, which although significantly reducing the buffet loads also caused a slight loss in lift. This solution was less effective at higher angles of attack [24]. Piezoelectric actuators have been fitted to the tail of aircraft to actively control the tail. There are other solutions such as active control surfaces, sucking and blowing to control vortices and finally stiffening the structure. There have been hybrid approaches such as combining active control surfaces and piezoelectric

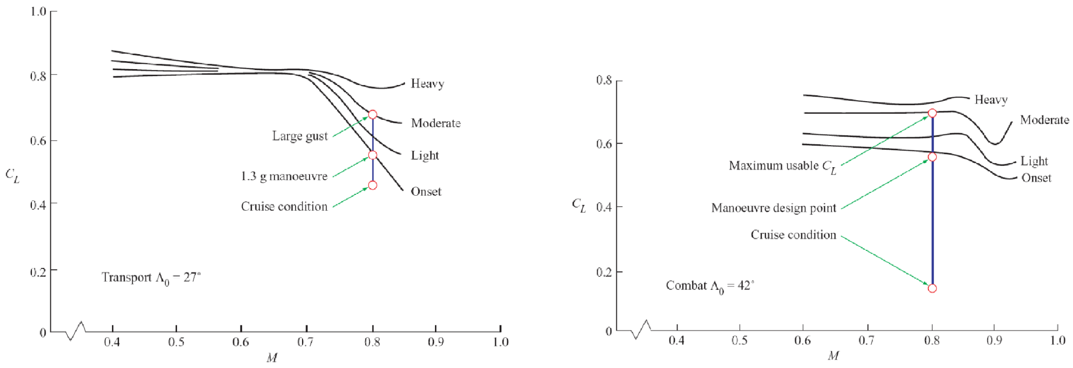

(a) Civil transport aircraft (b) Military fighter aircraft

Figure 1.3: Buffeting criteria (from ref. [6])

actuators to control vertical tails [25], which resulted in a 60% reduction in the buffeting for a 8% weight penalty.

Aircraft airworthiness regulations require that an aircraft is demonstrated to be free from aeroelastic instabilities (especially flutter) under flight conditions using a margin of safety of 15%. Flutter is an aeroelastic phenomenon that can be prevented through proper design, such as ensuring the bending and torsion mode frequencies remain separated [31] and decoupling modes. This should be backed up by flutter analysis throughout the design process. This is achieved using windtunnel models and computational analysis and, once a prototype has been manufactured, ground vibration and flight tests [32]. The number of cases that need to be analysed for a modern transport aircraft was estimated to be between five to ten thousand cases [33]. Throughout the life of the aircraft any changes to the structure that may impact the flutter boundary, require the flight envelope to be demonstrated safe again. Military combat aircraft are typically fitted with deployable stores both internally and externally with each combination requiring the flight envelope to be cleared. An example is the F/A-18E that was estimated to have 400,000 possible store combinations [34]. As such it is not feasible to fly this number of flight conditions, so the most critical combinations must be identified prior to flight testing [35]. Clearance is further complicated by the transonic dip phenomenon, where the flutter boundary moves closer to the flight envelope due to the formation of shockwaves. An example is shown in Figure 1.4 for the BAE Systems Hawk advanced jet trainer with the flutter boundary calculated using a weakened structural model by a linear method (NASTRAN) and by non-linear CFD (Euler equations) [7].

In summary aeroelastic phenomenon have generally been seen to have a negative impact on aircraft with flutter leading to severe damage or destruction of the aircraft or a component. Buffet leads to a reduced fatigue life and therefore

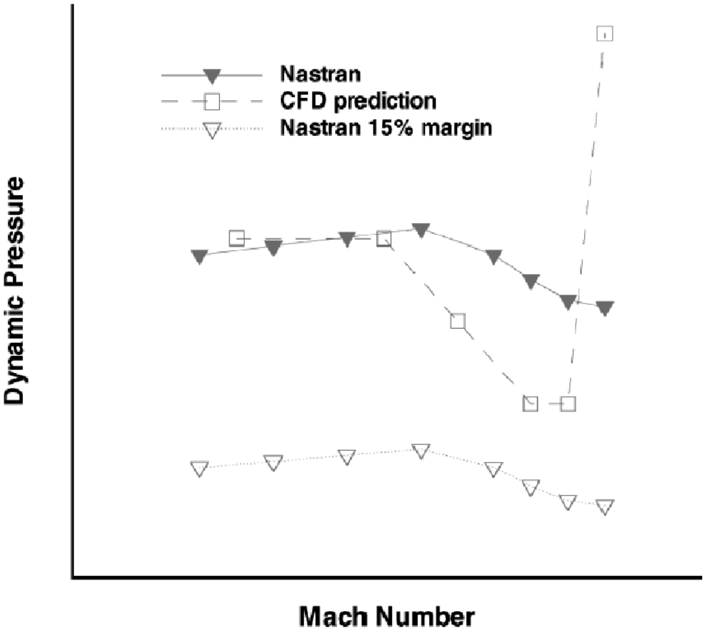

Figure 1.4: Comparison between the flutter boundaries predicted using the linear method and the wing-only configuration for the weakened structural model. (from ref. [7])

higher operating costs. This all adds to the complexity of clearing an aircraft's flight envelope. However in more recent years aeroelasticity has been used in multidisciplinary optimisation routines to attempt to take advantage of the reduced structural weight possible when aeroelasticity is taken into account [36]. As mentioned previously, the X-53 Aeroelastic Research Wing has attempted to make use of aeroelasticity to increase the control authority of the aircraft. Also by taking aeroelasticity into account the drag produced can be reduced through the definition of a jig shape.

1.2 Prediction of Flutter

The standard methods for calculating flutter have been the k and p-k methods. Both of these methods work by coupling linear aerodynamics and linear structural mechanics and then solving an eigenvalue problem. In the k method the aerodynamics are introduced into a vibration analysis using complex inertial terms, the p-k method introduces the aerodynamics as frequency dependent stiffness and damping terms. These methods are explained in reference [37]. The linear aerodynamics usually come from the doublet lattice method for subsonic flow. The doublet lattice method is based upon potential flow, which assumes the flow is incompressible, inviscid, irrotational and that the angle of attack is small with thin lifting surfaces. Therefore this method does not capture non-linearities in the flow due to shockwaves, boundary-layers and flow separation. This methodology is implemented in commercial packages such as NASTRAN and performs well inside its region of applicability and as such is the industry standard that all other methods are compared against.

However in the transonic regime as previously mentioned there is the transonic dip in the flutter boundary. This cannot be captured using linear aerodynamics due to the nonlinearities caused by the formation of shockwaves. To overcome this problem there has been a move towards unsteady nonlinear aerodynamics, which can be predicted by, for example, the Euler equations. This has focused on time-marching calculations and the technology which has been developed to allow these calculations will be covered in more detail in the next section. In these time-marching calculations the system is given an initial perturbation and the temporal response is calculated to determine its growth or decay to infer the system stability. This has been shown to be effective at calculating the flutter boundary, for the example of a wing [7] and for a full aircraft [38]. However this approach is unfeasible for the use of clearing a flight envelope due to the computational expense.

In recent years there has been an effort to reduce the cost of flutter calculations at the University of Liverpool and this has lead to the development of the Schur code [39, 40, 41]. This solver computes the onset of flutter as a stability problem for the steady state of the coupled system. It assumes Hopf Bifurcation, which is when stability is lost as the coupled system's Jacobian matrix has a pair of eigenvalues that cross the imaginary axis. This system is solved using the Schur complement and has been parallelised to allow realistically large problems to be computed. The method has been found to be about two orders of magnitude faster than the time domain approaches. For the flutter calculations in this thesis the Schur solver will be used and the solver is presented in more detail in Section 2.8.

1.3 Computational Aeroelasticity

Computational aeroelasticity (CAE) refers to the coupling of computational fluid dynamics (CFD) and computational structural dynamics (CSD). Over the past forty years the aerodynamic models have increased in fidelity from the transonic small disturbance in the 1970's, through the Euler equations in the 1980's to the Reynolds-averaged Navier-Stokes equations (RANS) in the 1990's. In more recent years detached eddy simulation (DES) and large eddy simulation (LES) are starting to be used. A more through review of CFD can be found in reference

[42].

There are two methodologies for computational aeroelasticity, the monolithic and the partitioned approaches. In the monolithic approach the governing equations are reformulated to combine the fluid and structural equations, which are then solved and integrated in time simultaneously. The partitioned approach is more commonly used and uses separate aerodynamic and structural solvers. This necessitates a method of transferring the aerodynamic loads to the structure and the displacements to the aerodynamic solver. Since there are issues with solving the system of equations in the monolithic approach, the partitioned approach has seen considerable effort in solving the various technological challenges required to make this approach work. The partitioned approach can be extended to include additional disciplines in a straight-forward manner, whereas the monolithic approach requires the governing equations to be reformulated to include the additional discipline. The main technological challenges for the partitioned approach are,

- how to deform the CFD mesh
- how to sequence the aerodynamic and structural solvers
- how to transfer the loads and displacements between solvers

These technological challenges have all been solved to various degrees.

A number of solutions to mesh movement have been proposed including remeshing, spring analogy, boundary element method (BEM), transfinite interpolation, Delaunay mapping and radial basis functions (RBF). Remeshing is where the entire mesh is regenerated at each time step and the solution is interpolated to the new grid, however this is a computationally expensive method. Batina [43] introduced the concept of the "Spring Analogy" for unstructured grids. The spring analogy works by replacing all the element edges with springs that have a stiffness, which is the inverse of the edge length. When the boundary is deformed the system of springs is iterated over to update the grid deformation. This was improved by Farhat *et al.* [44] through the addition of torsional springs in addition to the linear springs to prevent zero or negative areas/volumes in the mesh. A detailed analysis of the spring analogy and its relationship to elliptic grid generation is given by Blom [45]. The spring analogy can be used for structured meshes, but it is relatively costly compared to transfinite interpolation (TFI). Transfinite interpolation is an algebraic grid deformation technique that interpolates the grid points in the computational domain using prescribed points along the boundaries. An example implementation can be found in reference [46]. Chen and Jadic [47] proposed an exterior BEM solver, which assumes that the

CFD mesh is modelled as an infinite elastic medium with a deformable hollow slit that is the CFD surface mesh. This method is significantly more robust than the spring analogy, but has a higher computational cost. Delaunay mapping was proposed by Liu *et al.* [48] and was shown to be an order of magnitude faster than the spring analogy. The algorithm can be summarised as 1) using the surface mesh and a number of boundary points a Delaunay graph is generated, 2) all the CFD grid points are assigned an element from the Delaunay graph and the area/volume ratio coefficients are calculated, 3) as the CFD surface deforms the Delaunay graph is deformed, 4) the deformed CFD mesh can then be calculated using the previously computed area/volume ration coefficients. If the Delaunay graph elements intersect one another then the deformation is split recursively into equal amounts and applied in steps. This approach can be applied to any grid topology including hybrid grids. Radial basis functions were proposed for mesh deformation by de Boor *et al.* [49]. Radial basis functions are described in Chapter 3 as a transformation method, but can be applied as a mesh movement scheme by using the deforming surface mesh instead of the structural model to drive the volume mesh instead of the surface mesh. Rendall and Allen [2] commented that the quality of RBF was as good as the spring analogy and only required matrix multiplications at each time step, but was expensive in terms of data required with the matrix size being $N_{\text{surface points}} \times N_{\text{volume points}}$. This method was parallelised by Rendall and Allen [50] and improved through the use of a greedy algorithm to reduce the number of centres used for the mesh movement.

Solver sequencing was largely solved by Farhat and Lesoinne [51] and the references therein. Presented were a number of approaches to sequencing for both serial and parallel calculations.

The transfer of data between solvers has been approached by many researchers over the years and is still an active topic of research. The most commonly used transfer method is infinite plate splines (IPS) developed by Harder and Desmarais [52] in 1972 and is used in the commercial package NASTRAN. Since then a number of methods have been proposed and these are covered in Chapter 3. However current methods still struggle with extrapolation beyond the planform of the structural model.

1.4 Thesis Organisation

The objective of this work is to investigate the influence of transformation methods on the flutter boundary and to consider the simulation of shock-induced buffet of a transport wing. This involves testing a number of transformation methods for their effect on flutter boundaries, verifying the flow solver for shock-induced buffet over an aerofoil and then for static aeroelastic calculations of an aeroelastic wing. Reviews of these topics can be found in their respective chapters (Chapter 3 for transformation methods, Chapter 5 for shock-induced buffet of an aerofoil and Chapter 6 for shock-induced buffet of a transport wing).

Chapter 2 introduces the formulation of the solvers to be used in this work. This includes the Aeroelastic Multiblock (AMB) flow solver and the Schur solver for fast flutter boundary calculations.

Chapter 3 introduces transformation methods and a description of their formulation. A different approach to transformation is proposed called the rigid ribs approach that is used for beam stick models.

Chapter 4 presents the evaluation of the transformation methods, both for mode shape reconstruction and their effect on flutter boundary predictions. This is shown using two test case, the Goland and the multi-disciplinary optimisation (MDO) wings. The effect of changing the direction of extrapolation for a beam stick model is also presented.

Chapter 5 is devoted to the calculation of buffet over the BGK No. 1 aerofoil to verify the AMB solver for shock-induced buffet. In this chapter a number of convergence studies are presented to find the effect of various parameters on the solver and solution. This is followed by an estimate of the buffet boundary using steady state calculations. The estimated buffet boundary is then verified using unsteady calculations and the mechanism for the shock oscillation is investigated.

Chapter 6 presents the static aeroelasticity of the Aeroelastic Research Wing (ARW-2) to verify that the aeroelastic deformation and aerodynamics can be captured by the AMB solver. This is followed by a buffet search using steady state calculations to find possible buffet cases.

Chapter 7 concludes the thesis and offers suggestions for future work. The appendices offer more detailed formulations of some of the transformation methods presented in Chapter 3.

Chapter 2

Formulation

2.1 Navier-Stokes Equations

The equations in differential conservative form are presented.

Continuity Equation

This is derived from the principle of conservation of mass.

$$\frac{\partial\rho}{\partial t}+\frac{\partial(\rho u)}{\partial x}+\frac{\partial(\rho v)}{\partial y}+\frac{\partial(\rho w)}{\partial z}=0 \tag{2.1}$$

where ρ is the density, u, v, w are the velocity components in the x, y, z directions and t is time.

Momentum Equations

These equations are derived from Newton's second law. The equation for the x component of momentum is

$$\frac{\partial(\rho u)}{\partial t}+\frac{\partial(\rho uu)}{x}+\frac{\partial(\rho uv)}{y}+\frac{\partial(\rho uw)}{z}=-\frac{\partial p}{\partial x}+\frac{\partial\tau_{xx}}{\partial x}+\frac{\partial\tau_{yx}}{\partial y}+\frac{\partial\tau_{zx}}{\partial z}+\rho f_x \tag{2.2}$$

for the y component

$$\frac{\partial(\rho v)}{\partial t}+\frac{\partial(\rho vu)}{x}+\frac{\partial(\rho vv)}{y}+\frac{\partial(\rho vw)}{z}=-\frac{\partial p}{\partial y}+\frac{\partial\tau_{xy}}{\partial x}+\frac{\partial\tau_{yy}}{\partial y}+\frac{\partial\tau_{zy}}{\partial z}+\rho f_y \tag{2.3}$$

and for the z component

$$\frac{\partial(\rho w)}{\partial t}+\frac{\partial(\rho wu)}{x}+\frac{\partial(\rho wv)}{y}+\frac{\partial(\rho ww)}{z}=-\frac{\partial p}{\partial z}+\frac{\partial\tau_{xz}}{\partial x}+\frac{\partial\tau_{yz}}{\partial y}+\frac{\partial\tau_{zz}}{\partial z}+\rho f_z \tag{2.4}$$

where τ_{ij} are the shear stresses and f_i are the body forces.

Energy Equation

This equation is derived from the principle of conservation of energy.

$$
\begin{aligned}
&\frac{\partial(\rho E)}{\partial t}+\frac{\partial(\rho uH)}{\partial x}+\frac{\partial(\rho vH)}{\partial y}+\frac{\partial(\rho wH)}{\partial z}=\rho\dot{q}-\left(\frac{\partial\dot{q}_x}{\partial x}+\frac{\partial\dot{q}_y}{\partial y}+\frac{\partial\dot{q}_z}{\partial z}\right)\\
&+\frac{\partial(u\tau_{xx})}{\partial x}+\frac{\partial(u\tau_{yx})}{\partial y}+\frac{\partial(u\tau_{zx})}{\partial z}+\frac{\partial(v\tau_{xy})}{\partial x}+\frac{\partial(v\tau_{yy})}{\partial y}+\frac{\partial(v\tau_{zy})}{\partial z}\\
&+\frac{\partial(w\tau_{xz})}{\partial x}+\frac{\partial(w\tau_{yz})}{\partial y}+\frac{\partial(w\tau_{zz})}{\partial z}+\rho(f_xu+f_yv+f_zw)
\end{aligned}
\tag{2.5}
$$

where $\dot{q}$ is the rate of volumetric heat addition per unit mass, $\dot{q}_i$ are the heat fluxes, the total energy is given by $E=e+\frac{u^2+v^2+w^2}{2}$ and the total enthalpy is given by $H=E+\frac{p}{\rho}$.

Additional Equations

Since air is a Newtonian fluid the shear stresses are given by

$$
\begin{array}{ll}
\tau_{xx}=2\mu\frac{\partial u}{\partial x}+\lambda(\frac{\partial u}{\partial x}+\frac{\partial v}{\partial y}+\frac{\partial w}{\partial z}) & \tau_{yy}=2\mu\frac{\partial v}{\partial y}+\lambda(\frac{\partial u}{\partial x}+\frac{\partial v}{\partial y}+\frac{\partial w}{\partial z})\\
\tau_{zz}=2\mu\frac{\partial w}{\partial z}+\lambda(\frac{\partial u}{\partial x}+\frac{\partial v}{\partial y}+\frac{\partial w}{\partial z}) & \tau_{xy}=\tau_{yx}=\mu\left(\frac{\partial v}{\partial x}+\frac{\partial u}{\partial y}\right)\\
\tau_{xz}=\tau_{zx}=\mu\left(\frac{\partial u}{\partial z}+\frac{\partial w}{\partial x}\right) & \tau_{yz}=\tau_{zy}=\mu\left(\frac{\partial w}{\partial y}+\frac{\partial v}{\partial z}\right)
\end{array}
\tag{2.6}
$$

where $\lambda=-\frac{2}{3}\mu$ and the laminar viscosity, μ, is given by Sutherland's law,

$$
\mu=\mu_0\left(\frac{T}{T_0}\right)^{\frac{3}{2}}\frac{T_0+110}{T+110}
\tag{2.7}
$$

where T is temperature, μ_0 is the reference viscosity at the reference temperature, T_0 and are taken as $\mu_0=1.7894\times10^{-5}$kg/ms and $T_0=288.16$K. Fourier's law of heat conduction states that

$$
\dot{q}_x=-\kappa\frac{\partial T}{\partial x}\qquad\dot{q}_y=-\kappa\frac{\partial T}{\partial y}\qquad\dot{q}_z=-\kappa\frac{\partial T}{\partial z}
\tag{2.8}
$$

where κ is the thermal conductivity. So for a given time and location, the Navier-Stokes equation have the variables ρ, u, v, w, p, e and T to solve for and only five equations. By assuming that air is a perfect gas an additional equation can be specified

$$
p=\rho RT
\tag{2.9}
$$

where R is the specific gas constant. If the gas is assumed to be a calorically perfect gas then

$$
e=c_vT,\quad h=c_pT
\tag{2.10}
$$

where c_v is the specific heat at constant volume and c_p is the specific heat at constant pressure. Then the heat fluxes can be rewritten as

$$\dot{q}_x = -\frac{\mu}{Pr}\frac{\partial h}{\partial x} \qquad \dot{q}_y = -\frac{\mu}{Pr}\frac{\partial h}{\partial y} \qquad \dot{q}_z = -\frac{\mu}{Pr}\frac{\partial h}{\partial z} \tag{2.11}$$

where $Pr = \frac{c_p \mu}{\kappa}$ is the Prandtl number. For most aerodynamic applications it is usual to neglect the body forces and the volumetric heating. Body forces are assumed to be negligible, therefore the terms ρf_i from the momentum equations and $\rho(f_x u + f_y v + f_z w)$ from the energy equation are neglected. Volumetric heating is assumed to be negligible, therefore $\rho\dot{q}$ from the energy equation is neglected.

2.2 Turbulence

When the Reynolds number is sufficiently low the fluid flows with no disruption between layers. This type of flow is called laminar. As the Reynolds number is increased the flow becomes unstable and transitions to a turbulent flow. A turbulent flow has rapid fluctuations in velocity and pressure and is inherently three-dimensional and unsteady. Turbulence has a range of scales that are linked to structures in the flow called turbulent eddies. This can be seen in Figure 2.1 of a laser induced florescence image of a submerged turbulent jet. There are large scale eddies of the order of the jet width as well as much smaller eddies.

Turbulent eddies are local swirling motions where the vorticity is large. The largest eddies interact with and extract energy from the mean flow by a process called vortex stretching. The mean velocity gradients distort the eddies if they are aligned in a direction in which the mean velocity gradients can stretch them. Each turbulent eddy has a characteristic length, ℓ, velocity, u_ℓ and time, τ_ℓ scale associated to it. For the larger eddies their Reynolds number tends to be large (on the order of the mean flow) suggesting that they are dominated by inertial forces. The smaller eddies are also stretched, but mainly by slightly larger eddies as opposed to the mean flow. This leads to a cascade of energy from the larger eddies to the smaller eddies. An energy spectrum of turbulence is shown in Figure 2.2. It can be seen that most of the energy is contained in the larger eddies and as such are referred to as the energy containing eddies. The largest eddies are unaffected by viscosity and depend on their velocity and length scales. Dimensional analysis gives the spectral energy content as

$$E(\kappa) \propto u_\ell^2 \ell \tag{2.12}$$

where κ is the wavenumber from a Fourier decomposition. As such the largest eddies are expected to be highly anisotropic. At the other end of the scale the

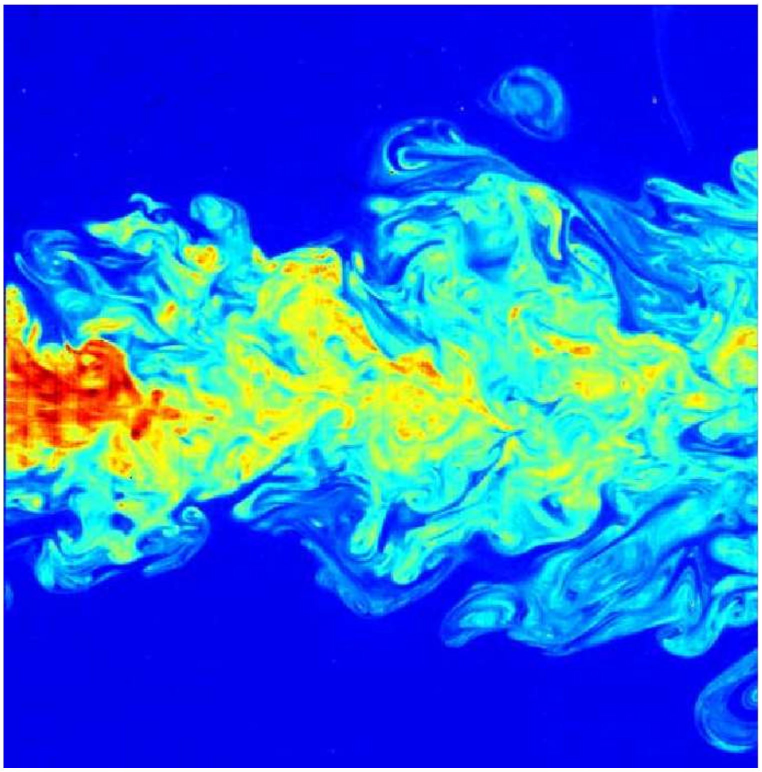

Figure 2.1: False-colour image of the far-field of a submerged turbulent jet using laser induced fluorescence (LIF). (from ref. [8])

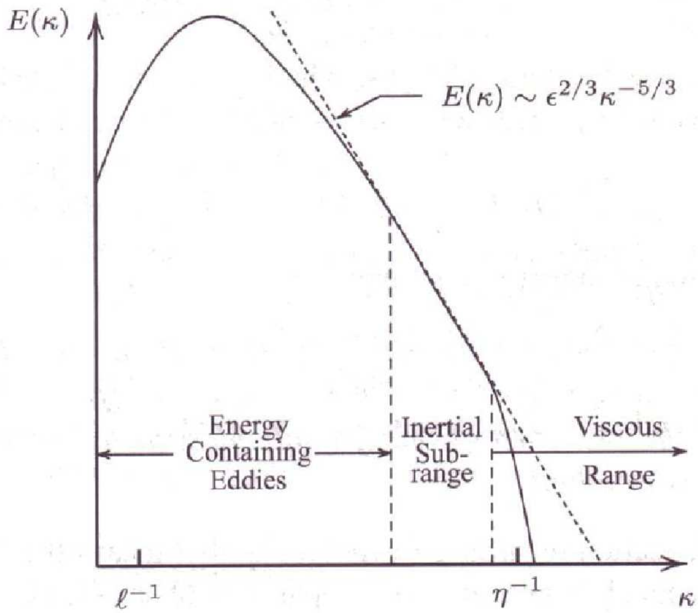

Figure 2.2: Energy spectrum for a turbulent flow, log-log scales. (from ref. [9])

smallest eddies contain the least energy and are dominated by viscous forces. The smallest of these scales of turbulence are called the Kolmogorov scales of length, η, velocity, u_η and time, τ_η. The Kolmogorov scales can be derived using dimensional analysis and are only dependent on the rate of dissipation, ε and the kinematic viscosity, ν and are given by

$$\eta = \left(\frac{\nu^3}{\varepsilon}\right)^{1/4}, \quad u_\eta = (\varepsilon\nu)^{1/4}, \quad \tau_\eta = \left(\frac{\nu}{\varepsilon}\right)^{1/2} \tag{2.13}$$

The smallest of the turbulent scales is fixed by viscous dissipation of energy, but is still many times larger than any molecular scale, as such turbulence is a continuum phenomenon. However the rate of dissipation is controlled by the rate at which these smallest eddies receive energy from the larger eddies. Through dimensional analysis the ratio of the scales can be obtained based upon the turbulent Reynolds number, $Re_T = \frac{k^{1/2}l}{\nu}$,

$$\frac{\ell}{\eta} \sim Re_T^{3/4}, \quad \frac{u_\ell}{u_\eta} \sim Re_T^{1/4}, \quad \frac{\tau_\ell}{\tau_\eta} \sim Re_T^{1/2} \tag{2.14}$$

This shows that as the Reynolds number increases so does the range of scales in the flow. Kolmogorov argued that the spectral energy of the smallest scales should be a function of the rate of dissipation and the kinematic viscosity. Through dimensional analysis

$$E(\kappa = 1/\eta) \propto \varepsilon^{5/4}\nu^{1/4} \tag{2.15}$$

The diffusive action of the viscous stress tends to smear out any anisotropic behaviour in the smallest eddies leading to the smallest eddies being isotropic. In Figure 2.2 the smallest eddies are referred to as the viscous range. In Figure 2.2 there is an intermediate range of eddies referred to as the inertial subrange. These eddies were assumed by Kolmogorov to be large enough to unaffected by viscosity, but small enough to be expressed as a function of energy dissipation, so through dimensional analysis

$$E(\kappa) = C_k\varepsilon^{2/3}\kappa^{-5/3} \qquad \text{for } \frac{1}{l} \ll \kappa \ll \frac{1}{\eta} \tag{2.16}$$

where C_k is the Kolmogorov constant. This is also known as Kolmogorov's -5/3 law.

Large eddies carry smaller scale eddies with them as they move with the flow and the lifetime of eddies can be as much as 30 times the characteristic length of the flow. This means that the current state of a turbulent flow depends upon the upstream history and cannot be uniquely defined by the local strain rate tensor. Finally viscous and turbulent flows are always diffusive and the diffusion is dominated by the large eddies. These large eddies cause increased mixing of mass, momentum and energy and is called turbulent mixing.

The rate of dissipation, ε has been used throughout this section and its definition is

$$\varepsilon = -\frac{dk}{dt} \tag{2.17}$$

where k is the specific kinetic energy of the fluctuating velocity.

2.3 The Closure Problem

The Navier-Stokes equations can be solved for turbulent flow in a number of ways. Direct numerical simulation (DNS) solves the equations directly using a sufficiently fine grid and time step to resolve all the turbulent eddies, however this is hugely expensive and it is infeasible for realistic geometries and Reynolds numbers with current computer hardware. Another approach is to use large eddy simulation (LES), where the large eddies are directly simulated and the small eddies are approximated using a sub-grid-scale model. This method is still too expensive to use for realistic geometries and Reynolds numbers with current computer hardware, but it is being used more and more in research. The next simplification is Deattached Eddy Simulation (DES). In this method LES is used for the majority of the flow, but as the wall is approached the LES method requires a large number of grid points and tends towards DNS levels of refinement. To overcome this DES applies Reynolds Averaged Navier-Stokes in the boundary-layer region, which reduces the computational cost. The final method of solving the Navier-Stokes equations for turbulent flows is the Reynolds Averaged Navier-Stokes (RANS), also called Unsteady Reynolds Averaged Navier-Stokes (URANS) when applied to unsteady flows. This is the cheapest method and it will be shown below that the Reynolds averaging procedure causes a closure problem, which then requires a turbulence model to close the system of equations. The calculations to be presented in this thesis use the RANS/URANS approach. The cost in terms of grid size and time steps and level of empiricism was estimated by Spalart [1] in 2000 and is shown in Table 2.1. This gives an idea of the relative cost of each method and when it will be applied to a whole aircraft case assuming an increase in computer power by a factor of five every five years. The time steps column is the number of time steps each method needs for the flow to travel six times the span of the aircraft.

Table 2.1: Summary of Solution Method Costs (from Ref. [1])

Method	Empiricism	Grid Size	Time Steps	Estimated Ready
URANS	Strong	10^7	$10^{3.5}$	1995
DES	Strong	10^8	10^4	2000
LES	Weak	$10^{11.5}$	$10^{6.7}$	2045
DNS	None	10^{16}	$10^{7.7}$	2080

2.3.1 Reynolds Averaging

Reynolds averaging can be used to simplify the Navier-Stokes equations to the RANS equations. This is achieved through Reynolds decomposition. Reynolds decomposition involves splitting the instantaneous flow variables into a mean and unsteady fluctuation components. There are three methods of averaging: time, spatial and ensemble averaging. The method used here is time averaging. This is illustrated with a generic flow variable f, which is split into a mean, $\overline{f}$ and an unsteady fluctuation due to turbulence, f'.

$$f = \overline{f} + f' \tag{2.18}$$

The time average $\overline{f}$ is calculated by

$$\overline{f} = \frac{1}{\Delta t}\int_t^{t+\Delta t} f dt \tag{2.19}$$

noting that

$$\overline{f'} = \frac{1}{\Delta t}\int_t^{t+\Delta t} f' dt \equiv 0 \tag{2.20}$$

The time average of the product of two flow variables $\overline{fg}$ is given by $\overline{f}\overline{g}+\overline{f'g'}$, because the average of the product of two fluctuating components is not necessarily zero.

2.3.2 Favre Mass Averaging for Compressible Flow

The above Reynolds averaging approach can be used for compressible flow, however it leads to a very complex system of equations. To avoid this Favre mass averaging is used. Favre mass averaging defines mass averaged variables, so for a generic flow variable f the mass averaged variable, $\tilde{f}$ is

$$\tilde{f} = \frac{\overline{\rho f}}{\overline{\rho}} \tag{2.21}$$

where $\overline{\rho}$ is the time averaged density. In a similar way to Reynolds averaging the flow variables can be decomposed into mass averaged $\tilde{f}$ and fluctuating f'' parts.

$$f = \tilde{f} + f'' \tag{2.22}$$

It is important to note that the time averages of the double primed fluctuating quantities are not equal to zero, however the time average of $\overline{\rho f''}$ is equal to zero. This procedure is a mathematical simplification that removes the density fluctuations from the averaged equations, but it does not remove the effect of the density fluctuations from the turbulence. To get to the Favre averaged Navier-Stokes equations the following flow variables are substituted into the Navier-Stokes equations given by Equations 2.1 to 2.5 and then time averaged.

$$\begin{array}{lll}
u = \tilde{u} + u'' & v = \tilde{v} + v'' & w = \tilde{w} + w'' \\
e = \tilde{e} + e'' & h = \tilde{h} + h'' & T = \tilde{T} + T'' \\
\dot{q_x} = \dot{q_{Lx}} + \dot{q_x}' & \dot{q_y} = \dot{q_{Ly}} + \dot{q_y}' & \dot{q_z} = \dot{q_{Lz}} + \dot{q_z}' \\
\rho = \overline{\rho} + \rho' & p = \overline{p} + p' &
\end{array}$$

The resulting Favre averaged Navier-Stokes equations are then

Continuity Equation

$$\frac{\partial \overline{\rho}}{\partial t} + \frac{\partial(\overline{\rho}\tilde{u})}{\partial x} + \frac{\partial(\overline{\rho}\tilde{v})}{\partial y} + \frac{\partial(\overline{\rho}\tilde{w})}{\partial z} = 0 \tag{2.23}$$

Momentum Equations

In the x direction

$$\begin{aligned}
\frac{\partial(\overline{\rho}\tilde{u})}{\partial t} + \frac{\partial(\overline{\rho}\tilde{u}\tilde{u})}{\partial x} + \frac{\partial(\overline{\rho}\tilde{u}\tilde{v})}{\partial y} + \frac{\partial(\overline{\rho}\tilde{u}\tilde{w})}{\partial z} = &-\frac{\partial \overline{p}}{\partial x} + \frac{\partial(\overline{\tau_{xx}} + \tau_{xx}^R)}{\partial x} + \frac{\partial(\overline{\tau_{yx}} + \tau_{yx}^R)}{\partial y} \\
&+ \frac{\partial(\overline{\tau_{zx}} + \tau_{zx}^R)}{\partial z}
\end{aligned} \tag{2.24}$$

In the y direction

$$\begin{aligned}
\frac{\partial(\overline{\rho}\tilde{v})}{\partial t} + \frac{\partial(\overline{\rho}\tilde{v}\tilde{u})}{\partial x} + \frac{\partial(\overline{\rho}\tilde{v}\tilde{v})}{\partial y} + \frac{\partial(\overline{\rho}\tilde{v}\tilde{w})}{\partial z} = &-\frac{\partial \overline{p}}{\partial y} + \frac{\partial(\overline{\tau_{xy}} + \tau_{xy}^R)}{\partial x} + \frac{\partial(\overline{\tau_{yy}} + \tau_{yy}^R)}{\partial y} \\
&+ \frac{\partial(\overline{\tau_{zy}} + \tau_{zy}^R)}{\partial z}
\end{aligned} \tag{2.25}$$

In the z direction

$$\begin{aligned}
\frac{\partial(\overline{\rho}\tilde{w})}{\partial t} + \frac{\partial(\overline{\rho}\tilde{w}\tilde{u})}{\partial x} + \frac{\partial(\overline{\rho}\tilde{w}\tilde{v})}{\partial y} + \frac{\partial(\overline{\rho}\tilde{w}\tilde{w})}{\partial z} = &-\frac{\partial \overline{p}}{\partial z} + \frac{\partial(\overline{\tau_{xz}} + \tau_{xz}^R)}{\partial x} + \frac{\partial(\overline{\tau_{yz}} + \tau_{yz}^R)}{\partial y} \\
&+ \frac{\partial(\overline{\tau_{zz}} + \tau_{zz}^R)}{\partial z}
\end{aligned} \tag{2.26}$$

Energy Equation

$$\begin{aligned}
&\frac{\partial(\overline{\rho}E)}{\partial t} + \frac{\partial(\overline{\rho}\tilde{u}H)}{\partial x} + \frac{\partial(\overline{\rho}\tilde{v}H)}{\partial y} + \frac{\partial(\overline{\rho}\tilde{w}H)}{\partial z} = \qquad (2.27)\\
&-\left(\frac{\partial}{\partial x}\left[\dot{q_{Lx}} + \dot{q_{Tx}}\right] + \frac{\partial}{\partial y}\left[\dot{q_{Ly}} + \dot{q_{Ty}}\right] + \frac{\partial}{\partial z}\left[\dot{q_{Lz}} + \dot{q_{Tz}}\right]\right)\\
&+\frac{\partial}{\partial x}\left[\tilde{u}(\overline{\tau_{xx}} + \tau^R_{xx}) + \tilde{v}(\overline{\tau_{yx}} + \tau^R_{yx}) + \tilde{w}(\overline{\tau_{zx}} + \tau^R_{zx})\right]\\
&+\frac{\partial}{\partial y}\left[\tilde{u}(\overline{\tau_{xy}} + \tau^R_{xy}) + \tilde{v}(\overline{\tau_{yy}} + \tau^R_{yy}) + \tilde{w}(\overline{\tau_{zy}} + \tau^R_{zy})\right]\\
&+\frac{\partial}{\partial z}\left[\tilde{u}(\overline{\tau_{xz}} + \tau^R_{xz}) + \tilde{v}(\overline{\tau_{yz}} + \tau^R_{yz}) + \tilde{w}(\overline{\tau_{zz}} + \tau^R_{zz})\right] \qquad (2.28)
\end{aligned}$$

where E and H are redefined as $E = \tilde{e} + \frac{\tilde{u}^2+\tilde{v}^2+\tilde{w}^2}{2} + k$ and $H = \tilde{h} + \frac{\tilde{u}^2+\tilde{v}^2+\tilde{w}^2}{2} + k$. The mean viscous stresses are given by

$$\begin{array}{ll}
\overline{\tau_{xx}} = 2\mu\frac{\partial\tilde{u}}{\partial x} - \frac{2}{3}\mu(\frac{\partial\tilde{u}}{\partial x} + \frac{\partial\tilde{v}}{\partial y} + \frac{\partial\tilde{w}}{\partial z}) & \overline{\tau_{yy}} = 2\mu\frac{\partial\tilde{v}}{\partial y} - \frac{2}{3}\mu(\frac{\partial\tilde{u}}{\partial x} + \frac{\partial\tilde{v}}{\partial y} + \frac{\partial\tilde{w}}{\partial z})\\
\overline{\tau_{zz}} = 2\mu\frac{\partial\tilde{w}}{\partial z} - \frac{2}{3}\mu(\frac{\partial\tilde{u}}{\partial x} + \frac{\partial\tilde{v}}{\partial y} + \frac{\partial\tilde{w}}{\partial z}) & \overline{\tau_{xy}} = \overline{\tau_{yx}} = \mu\left(\frac{\partial\tilde{v}}{\partial x} + \frac{\partial\tilde{u}}{\partial y}\right)\\
\overline{\tau_{xz}} = \overline{\tau_{zx}} = \mu\left(\frac{\partial\tilde{u}}{\partial z} + \frac{\partial\tilde{w}}{\partial x}\right) & \overline{\tau_{yz}} = \overline{\tau_{zy}} = \mu\left(\frac{\partial\tilde{w}}{\partial y} + \frac{\partial\tilde{v}}{\partial z}\right)
\end{array} \qquad (2.29)$$

The Reynolds stresses τ^R_{ij} are given by

$$\begin{array}{ll}
\overline{\rho}\tau^R_{xx} = -\overline{\rho u''u''} & \overline{\rho}\tau^R_{yy} = -\overline{\rho v''v''}\\
\overline{\rho}\tau^R_{zz} = -\overline{\rho w''w''} & \overline{\rho}\tau^R_{xy} = \tau^R_{yx} = -\overline{\rho u''v''}\\
\overline{\rho}\tau^R_{xz} = \overline{\rho}\tau^R_{zx} = -\overline{\rho u''w''} & \overline{\rho}\tau^R_{yz} = \overline{\rho}\tau^R_{zy} = -\overline{\rho v''w''}
\end{array} \qquad (2.30)$$

and the heat flux components (subscripts L and T are for laminar and turbulence respectively) are

$$\begin{array}{ll}
\dot{q}_{Lx} = -\frac{\mu}{Pr}\frac{\partial\tilde{h}}{\partial x} & \dot{q}_{Tx} = -\frac{\mu_T}{Pr_T}\frac{\partial\tilde{h}}{\partial x}\\
\dot{q}_{Ly} = -\frac{\mu}{Pr}\frac{\partial\tilde{h}}{\partial y} & \dot{q}_{Ty} = -\frac{\mu_T}{Pr_T}\frac{\partial\tilde{h}}{\partial y}\\
\dot{q}_{Lz} = -\frac{\mu}{Pr}\frac{\partial\tilde{h}}{\partial z} & \dot{q}_{Tz} = -\frac{\mu_T}{Pr_T}\frac{\partial\tilde{h}}{\partial z}
\end{array} \qquad (2.31)$$

where μ_T is the turbulent eddy viscosity and Pr_T is the turbulent Prandtl number. This introduces six more unknowns that need to be modeled to close the problem. For general three-dimensional flows there are 6 unknown mean-flow properties, density, pressure, enthalpy and the three velocities, as well as six Reynolds-stress unknowns, which brings the total number of unknowns to twelve. There are only five equations to solve and so more equations are required to close the problem. This is referred to as the closure problem.

2.3.3 Boussinesq's Approximation

One common approach to solve the closure problem is using the Boussinesq approximation. This is based on an analogy between the Reynolds stresses and the viscous stresses. This leads to the equations for the Reynolds stresses being rewritten in the form

$$\begin{aligned}
\overline{\rho}\tau^R_{xx} &= -\overline{\rho u'' u''} = 2\mu_T\left(\tfrac{\partial\tilde{u}}{\partial x} - \tfrac{1}{3}\left(\tfrac{\partial\tilde{u}^2}{\partial x} + \tfrac{\partial\tilde{v}^2}{\partial x} + \tfrac{\partial\tilde{w}^2}{\partial x}\right)\right) - \tfrac{2}{3}\overline{\rho}k \\
\overline{\rho}\tau^R_{yy} &= -\overline{\rho v'' v''} = 2\mu_T\left(\tfrac{\partial\tilde{v}}{\partial y} - \tfrac{1}{3}\left(\tfrac{\partial\tilde{u}^2}{\partial x} + \tfrac{\partial\tilde{v}^2}{\partial x} + \tfrac{\partial\tilde{w}^2}{\partial x}\right)\right) - \tfrac{2}{3}\overline{\rho}k \\
\overline{\rho}\tau^R_{zz} &= -\overline{\rho w'' w''} = 2\mu_T\left(\tfrac{\partial\tilde{w}}{\partial z} - \tfrac{1}{3}\left(\tfrac{\partial\tilde{u}^2}{\partial x} + \tfrac{\partial\tilde{v}^2}{\partial x} + \tfrac{\partial\tilde{w}^2}{\partial x}\right)\right) - \tfrac{2}{3}\overline{\rho}k \\
\overline{\rho}\tau^R_{xy} &= \overline{\rho}\tau^R_{yx} = -\overline{\rho u'' v''} = 2\mu_T\left(\tfrac{1}{2}\left(\tfrac{\partial\tilde{u}}{\partial y} + \tfrac{\partial\tilde{v}}{\partial x}\right) - \tfrac{1}{3}\left(\tfrac{\partial\tilde{u}^2}{\partial x} + \tfrac{\partial\tilde{v}^2}{\partial x} + \tfrac{\partial\tilde{w}^2}{\partial x}\right)\right) - \tfrac{2}{3}\overline{\rho}k \\
\overline{\rho}\tau^R_{xz} &= \overline{\rho}\tau^R_{zx} = -\overline{\rho u'' w''} = 2\mu_T\left(\tfrac{1}{2}\left(\tfrac{\partial\tilde{u}}{\partial z} + \tfrac{\partial\tilde{w}}{\partial x}\right) - \tfrac{1}{3}\left(\tfrac{\partial\tilde{u}^2}{\partial x} + \tfrac{\partial\tilde{v}^2}{\partial x} + \tfrac{\partial\tilde{w}^2}{\partial x}\right)\right) - \tfrac{2}{3}\overline{\rho}k \\
\overline{\rho}\tau^R_{yz} &= \overline{\rho}\tau^R_{zy} = -\overline{\rho v'' w''} = 2\mu_T\left(\tfrac{1}{2}\left(\tfrac{\partial\tilde{v}}{\partial z} + \tfrac{\partial\tilde{w}}{\partial y}\right) - \tfrac{1}{3}\left(\tfrac{\partial\tilde{u}^2}{\partial x} + \tfrac{\partial\tilde{v}^2}{\partial x} + \tfrac{\partial\tilde{w}^2}{\partial x}\right)\right) - \tfrac{2}{3}\overline{\rho}k
\end{aligned} \tag{2.32}$$

where k is the specific turbulent kinetic energy given by

$$\overline{\rho}k = \frac{1}{2}\overline{\rho u'' u''} \tag{2.33}$$

The two main assumptions used in the Boussinesq approximation are that the Reynolds stresses can be defined at each point in space and time by mean velocity gradients and that the turbulent eddy viscosity is a scalar property of the flow with the relationship between the Reynolds stresses and the mean velocity gradients being linear. This approximation reduces the number of additional unknowns from six to one. The majority of turbulence models calculate this turbulent eddy viscosity as a function of velocity and length scales. There are a number of limitations of using this approximation. When a turbulent boundary-layer is perturbed from its equilibrium state a new equilibrium state is not reached for at least ten boundary-layer thicknesses downstream [9]. This observation means that the Boussinesq approximation along with the equilibrium approximations implicit in algebraic models will not provide an accurate description of separated flow. The Boussinesq approximation is not valid for flows over curved surfaces due to significant streamline curvature, which gives rise to uneven normal Reynolds stresses. Flows that are three-dimensional can cause the Boussinesq approximation not to be valid, this can be demonstrated in straight non-circular ducts where the turbulence model using this approximation fails to predict secondary motions. Flows which have large changes in mean strain rate such as separation cannot be described by the Boussinesq approximation. Although the Boussinesq approximation may not be valid in these flow conditions many turbulence models using this approximation have been successfully applied to these flow conditions.

2.3.4 Vector Form

The Navier-Stokes equations (in this case the Favre mass averaged form) can be written in vector form,

$$\frac{\partial \mathbf{W}}{\partial t} + \frac{\partial(\mathbf{F}_i - \mathbf{F}_v)}{\partial x} + \frac{\partial(\mathbf{G}_i - \mathbf{G}_v)}{\partial y} + \frac{\partial(\mathbf{H}_i - \mathbf{H}_v)}{\partial z} = 0 \tag{2.34}$$

where $\mathbf{W}$ is the solution vector of conserved variables given by

$$\mathbf{W} = \begin{pmatrix} \overline{\rho} \\ \overline{\rho}\tilde{u} \\ \overline{\rho}\tilde{v} \\ \overline{\rho}\tilde{w} \\ \overline{\rho}\tilde{E} \end{pmatrix} \tag{2.35}$$

The inviscid vectors are given by

$$\mathbf{F}_i = \begin{pmatrix} \overline{\rho}\tilde{u} \\ \overline{\rho}\tilde{u}\tilde{u} + \overline{p} \\ \overline{\rho}\tilde{v}\tilde{u} \\ \overline{\rho}\tilde{w}\tilde{u} \\ \overline{\rho}\tilde{u}\tilde{H} \end{pmatrix} \quad \mathbf{G}_i = \begin{pmatrix} \overline{\rho}\tilde{v} \\ \overline{\rho}\tilde{u}\tilde{v} \\ \overline{\rho}\tilde{v}\tilde{v} + \overline{p} \\ \overline{\rho}\tilde{w}\tilde{v} \\ \overline{\rho}\tilde{v}\tilde{H} \end{pmatrix} \quad \mathbf{H}_i = \begin{pmatrix} \overline{\rho}\tilde{w} \\ \overline{\rho}\tilde{u}\tilde{w} \\ \overline{\rho}\tilde{v}\tilde{w} \\ \overline{\rho}\tilde{w}\tilde{w} + \overline{p} \\ \overline{\rho}\tilde{w}\tilde{H} \end{pmatrix} \tag{2.36}$$

The viscous vector are given by

$$\begin{aligned}
\mathbf{F}_v &= \frac{1}{Re}\begin{pmatrix} 0 \\ \overline{\tau_{xx}} + \tau_{xx}^R \\ \overline{\tau_{xy}} + \tau_{xy}^R \\ \overline{\tau_{xz}} + \tau_{xz}^R \\ \tilde{u}(\overline{\tau_{xx}} + \tau_{xx}^R) + \tilde{v}(\overline{\tau_{xy}} + \tau_{xy}^R) + \tilde{w}(\overline{\tau_{xz}} + \tau_{xz}^R) - (\dot{q_{Lx}} + \dot{q_{Tx}}) \end{pmatrix} \\
\mathbf{G}_v &= \frac{1}{Re}\begin{pmatrix} 0 \\ \overline{\tau_{yx}} + \tau_{yx}^R \\ \overline{\tau_{yy}} + \tau_{yy}^R \\ \overline{\tau_{yz}} + \tau_{yz}^R \\ \tilde{u}(\overline{\tau_{yx}} + \tau_{yx}^R) + \tilde{v}(\overline{\tau_{yy}} + \tau_{yy}^R) + \tilde{w}(\overline{\tau_{yz}} + \tau_{yz}^R) - (\dot{q_{Ly}} + \dot{q_{Ty}}) \end{pmatrix} \\
\mathbf{H}_v &= \frac{1}{Re}\begin{pmatrix} 0 \\ \overline{\tau_{zx}} + \tau_{zx}^R \\ \overline{\tau_{zy}} + \tau_{zy}^R \\ \overline{\tau_{zz}} + \tau_{zz}^R \\ \tilde{u}(\overline{\tau_{zx}} + \tau_{zx}^R) + \tilde{v}(\overline{\tau_{zy}} + \tau_{zy}^R) + \tilde{w}(\overline{\tau_{zz}} + \tau_{zz}^R) - (\dot{q_{Lz}} + \dot{q_{Tz}}) \end{pmatrix}
\end{aligned} \tag{2.37}$$

where Re is the Reynolds number.

2.3.5 Non-dimensional Form

The Navier-Stokes equations can be non-dimensionalised using the following relationships

$$\begin{array}{llllll} x = \frac{x^*}{L^*}, & y = \frac{y^*}{L^*}, & z = \frac{z^*}{L^*}, & u = \frac{u^*}{U_\infty^*}, & v = \frac{v^*}{U_\infty^*}, & w = \frac{w^*}{U_\infty^*}, \\ \rho = \frac{\rho^*}{\rho_\infty^*}, & p = \frac{p^*}{\rho_\infty^* U_\infty^{*2}}, & t = \frac{t^*}{L^*/U_\infty^*}, & T = \frac{T^*}{T_\infty^*}, & e = \frac{e^*}{U_\infty^{*2}}, & \mu = \frac{\mu^*}{\mu_\infty^*} \end{array} \tag{2.38}$$

where the superscript * denotes a dimensional variable and L^* is usually taken to be the root chord. This allows the characteristic parameters such as Reynolds number, Mach number etc. to be varied independently of the flow variables.

2.3.6 Curvilinear Form

The Navier-Stokes equations can be rewritten in curvilinear form [10], this makes solving the equations on a body-fitted grid easier. If the physical region of interest is described by a Cartesian co-ordinate system x, y, z then a mapping is defined onto a computational domain ξ, η, ζ (a unit cube), the transformation can be written as

$$\xi = \xi(x, y, z), \quad \eta = \eta(x, y, z), \quad \zeta = \zeta(x, y, z), \quad t = t \tag{2.39}$$

and the Jacobian determinant of the transformation can be written as

$$J = \frac{\partial(\xi, \eta, \zeta)}{\partial(x, y, z)} \tag{2.40}$$

Then the Equations 2.34 are given by

$$\frac{\partial \hat{\mathbf{W}}}{t} + \frac{\partial(\hat{\mathbf{F}}_i - \hat{\mathbf{F}}_v)}{\partial \xi} + \frac{\partial(\hat{\mathbf{G}}_i - \hat{\mathbf{G}}_v)}{\partial \eta} + \frac{\partial(\hat{\mathbf{H}}_i - \hat{\mathbf{H}}_v)}{\partial \zeta} = 0 \tag{2.41}$$

where

$$\begin{aligned}
\hat{\mathbf{W}} &= \frac{1}{J}\mathbf{W} \\
\hat{\mathbf{F}}_i &= \frac{1}{J}\left(\xi_x \mathbf{F}_i + \xi_y \mathbf{G}_i + \xi_z \mathbf{H}_i\right) \\
\hat{\mathbf{G}}_i &= \frac{1}{J}\left(\eta_x \mathbf{F}_i + \eta_y \mathbf{G}_i + \eta_z \mathbf{H}_i\right) \\
\hat{\mathbf{H}}_i &= \frac{1}{J}\left(\zeta_x \mathbf{F}_i + \zeta_y \mathbf{G}_i + \zeta_z \mathbf{H}_i\right) \\
\hat{\mathbf{F}}_v &= \frac{1}{J}\left(\xi_x \mathbf{F}_v + \xi_y \mathbf{G}_v + \xi_z \mathbf{H}_v\right) \\
\hat{\mathbf{G}}_v &= \frac{1}{J}\left(\eta_x \mathbf{F}_v + \eta_y \mathbf{G}_v + \eta_z \mathbf{H}_v\right) \\
\hat{\mathbf{H}}_v &= \frac{1}{J}\left(\zeta_x \mathbf{F}_v + \zeta_y \mathbf{G}_v + \zeta_z \mathbf{H}_v\right)
\end{aligned} \tag{2.42}$$

2.4 Turbulence Modelling

If the Boussinesq approximation has been used then the eddy viscosity needs to be calculated using a turbulence model. Wilcox defines an ideal turbulence model as a model that introduces the minimum complexity whilst capturing the essence of the relevant physics. The models for the Favre mass averaged Navier-Stokes equations can be split into two categories, those that use the Boussinesq approximation and those that do not. This section will concentrate on a Boussinesq approximation model. The turbulence model that will be presented here is SST two equation model.

2.4.1 Menter SST k-ω Model

The Menter SST k-ω model [53] is a combination of the k-ω and k-ϵ models. It was observed that the k-ω model performed very well in the viscous sublayer of the boundary-layer and predicts the skin-friction and velocity profiles near the wall well. The model has good numerical stability and is better than the k-ϵ model in the log layer of the boundary-layer, especially for flows with adverse pressure gradients and compressible flows. However the k-ω model is sensitive to freestream values of ω and it fails to predict accurately pressure induced separation. The k-ϵ model is insensitive to freestream values of ω and performs well for predicting free shear flows. The k-ϵ model is insensitive to adverse pressure gradients, but overestimates the wall shear stress delaying the point of separation. The SST model combines the k-ω and k-ϵ models using a blending function F_1 that is 1 in the viscous sub-layer and 0 away from the surface. This allows the k-ω model to be used in the near wall region and the k-ϵ model in free shear flows with the advantages of both models whilst avoiding their weaknesses. The SST model also uses the basic idea behind the Johnson-King model, to enforce Bradshaw's observation that the principal turbulent shear stress is proportional to the turbulent kinetic energy in the wake region of the boundary-layer. By enforcing this proportionality introduces a lag effect into the equations that accounts for the transport of principal turbulent shear stress. This is achieved by defining the eddy viscosity as shown in Equation 2.43 with a limiter and adding a blending function F_2, which is 1 for boundary layer flows and 0 for free shear layers. The SST model is a major improvement over the k-ω and k-ϵ models for adverse pressure gradients and separating flows.

Eddy Viscosity

$$\mu_T = \frac{a_1 \overline{\rho} k}{\tilde{\omega}}, \quad \underbrace{\tilde{\omega} = max\left\{a_1\omega, \quad \Omega F_2\right\}}_{\text{Stress Limiter}} \tag{2.43}$$

Turbulent Kinetic Energy Equation

$$\underbrace{\frac{\partial}{\partial t}(\overline{\rho} k)}_{\text{Rate of change of } k} + \underbrace{\frac{\partial}{\partial x_j}(\overline{\rho}\tilde{u}_j k)}_{\text{Convection}} = \underbrace{\overline{\rho}\tau_{ij}\frac{\partial \tilde{u}_i}{\partial x_j}}_{\text{Production}} - \underbrace{\beta^* \overline{\rho} k \omega}_{\text{Dissipation}} + \underbrace{\frac{\partial}{\partial x_j}\left[\left(\mu + \sigma_k \frac{\overline{\rho} k}{\omega}\right)\frac{\partial k}{\partial x_j}\right]}_{\text{Diffusion}} \tag{2.44}$$

Specific Dissipation Rate Equation

$$\underbrace{\frac{\partial}{\partial t}(\overline{\rho}\omega)}_{\text{Rate of change of } \omega} + \underbrace{\frac{\partial}{\partial x_j}(\overline{\rho}\tilde{u}_j \omega)}_{\text{Convection}} = \underbrace{\gamma \frac{\omega}{k}\rho\tau_{ij}\frac{\partial \tilde{u}_i}{\partial x_j}}_{\text{Production}} - \underbrace{\beta \overline{\rho}\omega^2}_{\text{Dissipation}} + \underbrace{\frac{\partial}{\partial x_j}\left[\left(\mu + \sigma_w \frac{\overline{\rho} k}{\omega}\right)\frac{\partial \omega}{\partial x_j}\right]}_{\text{Diffusion}}$$

$$+ \underbrace{2(1-F_1)\sigma_{w2}\frac{\overline{\rho}}{\omega}\frac{\partial k}{\partial x_j}\frac{\omega}{x_j}}_{\text{Cross-diffusion}} \tag{2.45}$$

Closure Coefficients

$$a_1 = 0.31, \quad \kappa = 0.41, \quad \beta^* = \frac{9}{100} \tag{2.46}$$

the remaining closure coefficients are a blend of the k-ω and k-ε coefficients using the equation

$$\phi = F_1 \phi_1 + (1 - F_1)\phi_2 \tag{2.47}$$

where ϕ is a quantity to be blended and the subscripts 1 and 2 stand for k-ω and k-ε coefficients respectively.

$$F_1 = \tanh(arg_1^4), \quad arg_1 = \min\left(\max\left(\frac{\sqrt{k}}{\beta^*\omega y}, \frac{500\nu}{y^2\omega}\right), \frac{4\rho\sigma_{w2}k}{CD_{kw}y^2}\right)$$

$$CD_{kw} = max\left(2\sigma_{w2}\frac{\overline{\rho}}{\omega}\frac{\partial k}{\partial x_j}\frac{\omega}{x_j}, 10^{-20}\right) \tag{2.48}$$

The coefficients for the k-ω part are

$$\sigma_{k1} = 0.85, \quad \sigma_{w1} = 0.5, \quad \beta_1 = 0.075, \quad \gamma_1 = \frac{\beta_1}{\beta^*} - \frac{\sigma_{w1}\kappa^2}{\sqrt{\beta^*}} \tag{2.49}$$

The coefficients for the k-ε part are

$$\sigma_{k2} = 1.0, \quad \sigma_{w2} = 0.856, \quad \beta_2 = 0.0828, \quad \gamma_2 = \frac{\beta_2}{\beta^*} - \frac{\sigma_{w2}\kappa^2}{\sqrt{\beta^*}} \tag{2.50}$$

and finally

$$F_2 = \tanh(arg_2^2), \quad arg_2 = \max\left(\frac{2\sqrt{k}}{\beta^*\omega y}, \frac{500\nu}{y^2\omega}\right) \tag{2.51}$$

Additional improvements have been suggested by Menter *et al.* [54], they are a production limiter

$$P_k = \overline{\rho}\tau_{ij}\frac{\partial \tilde{u}_i}{\partial x_j} \quad \rightarrow \quad \tilde{P}_k = \min\left(P_k, 10\beta^* \rho k \omega\right) \tag{2.52}$$

and vorticity is replaced with strain rate in Equation 2.43. However these improvements are not implemented in the current solver.

2.5 Flow Solver

All the computations to be presented were performed using the Aeroelastic Multi-Block (AMB) in-house flow solver [55]. A wide variety of problems have been studied using this code including cavity flows, delta-wing aerodynamics, rotorcraft problems, flutter[7] and control surface buzz[10]. The governing equations are discretised using a cell-centred finite volume solver combined with an implicit dual-time stepping method. In this manner, the solution marches in pseudo-time for each real time-step to achieve fast convergence. The discretisation of the convective terms uses Osher's upwind scheme. Monotone upstream-centred schemes for conservation laws (MUSCL) interpolation is used to provide nominally second-order accuracy and the van Albada limiter is also applied to remove any spurious oscillations across shock waves. Central differencing is used to discretise the viscous terms, with the resulting non-linear system of equations generated being solved by integration in pseudo-time using a second-order backward difference. A Generalised Conjugate Gradient method is then used in conjunction with a Block Incomplete Lower-Upper (BILU) factorisation as a preconditioner to solve the linear system of equations, which is obtained from a linearisation in pseudo-time. A number of turbulence models are available in the solver as well as large-eddy simulation (LES) and detached eddy simulation (DES), however for the calculations presented throughout the RANS equations were solved using a turbulence model.

2.6 Mesh Movement

The mesh is deformed using a hybrid approach where the block vertices are deformed using the spring analogy and the mesh is deformed inside each block using transfinite interpolation (TFI).

2.6.1 Spring Analogy of Block Vertices

The spring analogy has been used by many researchers over the years to deform unstructured [43, 45] and structured meshes. However for structured grids there are more efficient methods of mesh deformation, such as TFI. With this in mind the spring analogy was used to deform the block vertices and TFI was used for the edges, faces and volumes. The spring analogy works by assuming each block edge is a spring with a stiffness that is the inverse of its length. To ensure that the blocks do not skew or invert additional springs were added diagonally inside the blocks. For the ith vertex connected to the jth vertex by the edge ij, the stiffness is given by

$$k_{ij} = \frac{1}{\sqrt{(x_i - x_j)^2 + (y_i - y_j)^2 + (z_i - z_j)^2}} \tag{2.53}$$

The displacement at the ith vertex is calculated iteratively by

$$\mathbf{dx}_i^{n+1} = \frac{\sum_{j=1}^{m_i} k_{ij} \mathbf{dx}_j^n}{\sum_{j=1}^{m_i} k_{ij}} \tag{2.54}$$

where the ith vertex is connected to m other vertices (denoted by j) using the current displacements (superscript n) for the update the displacement (superscript $n + 1$). The Dirichlet boundary condition is used (fixed displacements at the boundaries). Once the displacements have been converged adequately then the updated vertex coordinates are given by

$$\mathbf{x}_i^{\text{new}} = \mathbf{x}_i^{\text{old}} + \mathbf{dx}_i^{\text{converged}} \tag{2.55}$$

Once the block vertices have been updated the block edges can be updated using TFI with the block vertices as boundary conditions. Then the block faces are interpolated using TFI with the updated block edges as boundary conditions. Finally the block volumes are updated via TFI from the new block faces.

2.6.2 TFI of Block Edges

TFI is an algebraic method of grid deformation that is computationally efficient and easily implemented [46]. To update the block edges the updated block vertices are used as boundary conditions. The nodes along a block edge are transformed into a unit computational space (a line with local coordinate ξ) and inside this space the displacements are calculated using linear interpolation. The blending function $r(\xi)$ along the line can be calculated using

$$r(\xi) = \frac{\text{length of edge from the first node to the current node}}{\text{length of edge}} \tag{2.56}$$

and therefore the displacements along the edge can be calculated from the edge vertices,

$$\mathbf{dx}(\xi) = \mathbf{dx}(0)[1 - r(\xi)] + \mathbf{dx}(1)r(\xi) \tag{2.57}$$

Finally the updated coordinates of a given node are obtained by

$$\mathbf{x}(\xi) = \mathbf{x}_{initial}(\xi) + \mathbf{dx}(\xi) \tag{2.58}$$

2.6.3 TFI of Block Faces

Now the updated positions of the block edges are known, they can now be used as the boundary conditions for updating the block faces [10]. The faces can be transformed to a unit square with local coordinates (ξ,η) to allow the displacement to be interpolated using linear blending functions.

$$\mathbf{dx}(\xi,\eta) = \mathbf{f}_1(\xi,\eta) + \mathbf{f}_2(\xi,\eta) \tag{2.59}$$

where

$$\mathbf{f}_1(\xi,\eta) = [1 - r_1(\xi)]\mathbf{dx}(0,\eta) + r_3(\eta)\mathbf{dx}(1,\eta) \tag{2.60}$$

and

$$\mathbf{f}_2(\xi,\eta) = [1 - r_4(\eta)]\left[\mathbf{dx}(\xi,0) - \mathbf{f}_1(\xi,0)\right] + r_2(\eta)\left[\mathbf{dx}(\xi,1) - \mathbf{f}_1(\xi,1)\right] \tag{2.61}$$

The blending functions r_i along each edge are calculated in the same manner as before, using Equation 2.56. Finally the updated coordinates of a given node are obtained by

$$\mathbf{x}(\xi,\eta) = \mathbf{x}_{initial}(\xi,\eta) + \mathbf{dx}(\xi,\eta) \tag{2.62}$$

2.6.4 TFI of Block Volumes

Each block is bounded by six updated faces with the displacements known at all their nodes [10]. The face numbering are given in Figure 2.3. Linear blending is used between pairs of faces.

$$\mathbf{dx}(\xi,\eta,\zeta) = \mathbf{f}_1(\xi,\eta,\zeta) + \mathbf{f}_2(\xi,\eta,\zeta) + \mathbf{f}_3(\xi,\eta,\zeta) \tag{2.63}$$

where

$$\mathbf{f}_1(\xi,\eta,\zeta) = (1-\psi)\mathbf{dx}(0,\eta,\zeta) + \psi\mathbf{dx}(1,\eta,\zeta) \tag{2.64}$$

$$\mathbf{f}_2(\xi,\eta,\zeta) = (1-\phi)\left[\mathbf{dx}(\xi,0,\zeta) - \mathbf{f}_1(\xi,0,\zeta)\right] + \phi\left[\mathbf{dx}(\xi,1,\zeta) - \mathbf{f}_1(\xi,1,\zeta)\right] \tag{2.65}$$

$$\mathbf{f}_3(\xi,\eta,\zeta) = (1-\omega)\left[\mathbf{dx}(\xi,\eta,0) - \mathbf{f}_2(\xi,\eta,0)\right] + \omega\left[\mathbf{dx}(\xi,\eta,1) - \mathbf{f}_2(\xi,\eta,1)\right] \tag{2.66}$$

The blending functions, ψ, ϕ and ω are given by

$$\psi = (1-r_\eta)(1-r_\zeta)r_1 + (1-r_\eta)r_\zeta r_2 + r_\eta(1-r_\zeta)r_3 + r_\eta r_\zeta r_4 \tag{2.67}$$

$$\phi = (1-r_\zeta)(1-r_\xi)r_1 + (1-r_\zeta)r_\xi r_2 + r_\zeta(1-r_\xi)r_3 + r_\zeta r_\xi r_4 \tag{2.68}$$

$$\omega = (1-r_\xi)(1-r_\eta)r_1 + (1-r_\xi)r_\eta r_2 + r_\xi(1-r_\eta)r_3 + r_\xi r_\eta r_4 \tag{2.69}$$

$$\tag{2.70}$$

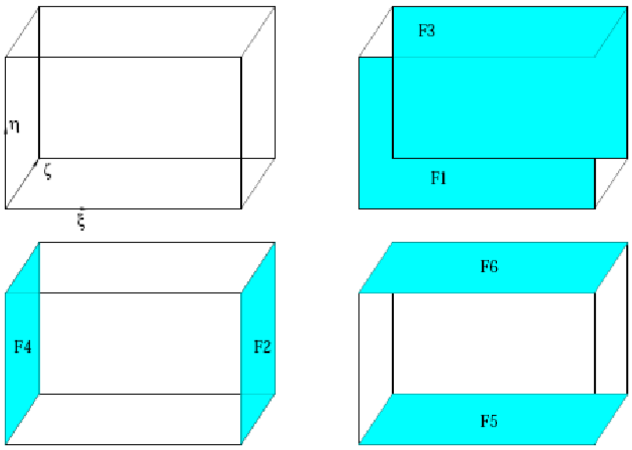

Figure 2.3: Faces of the block volume (from ref. [10])

where

$$r_\xi = \frac{r_1 + r_2 + r_3 + r_4}{4} \tag{2.71}$$

$$r_\eta = \frac{r_5 + r_6 + r_7 + r_8}{4} \tag{2.72}$$

$$r_\zeta = \frac{r_9 + r_{10} + r_{11} + r_{12}}{4} \tag{2.73}$$

$$\tag{2.74}$$

and the blending functions along each edge r_i are calculated as before using Equation 2.56. Finally the update coordinates of a given node is calculated using

$$\mathbf{x}(\xi, \eta, \zeta) = \mathbf{x}_{initial}(\xi, \eta, \zeta) + \mathbf{dx}(\xi, \eta, \zeta) \tag{2.75}$$

2.7 Structural Solver

If a structure is modelled as linear then it is possible to model the deformation as a summation of the modes of deformation. This approximation allows an n degrees of freedom structural model to be written as a second order linear ordinary differential equation

$$M\ddot{\mathbf{x}} + C\dot{\mathbf{x}} + K\mathbf{x} = \mathbf{f} \tag{2.76}$$

where M is the mass matrix, C is the viscous damping matrix and K is the stiffness matrix, all of size $n \times n$. Also $\mathbf{x}$ is the time dependent displacements and $\mathbf{f}$ is the time dependent external force vector both of size n. To calculate the undamped free vibration characteristics, Equation 2.76 is rewritten as

$$M\ddot{\mathbf{x}} + K\mathbf{x} = 0 \tag{2.77}$$

This equation can be solved subsituting $\mathbf{x} = \mathbf{X}e^{i\omega t}$ into Equation 2.77. The solution is

$$[K - \omega^2 M]\mathbf{X} = 0 \tag{2.78}$$

This is the premultiplied by M^{-1} to get

$$[M^{-1}K - \omega^2 M^{-1}M]\mathbf{X} = 0 \tag{2.79}$$

Let $A = M^{-1}K$ and $\lambda = \omega^2$. This leads to an eigen problem to be solved.

$$[A - \lambda I]\mathbf{X} = 0 \tag{2.80}$$

This can be solved to give the eigenvalues λ and the eigenvectors $\mathbf{X}$, which are the mode shapes. The mode shapes are usually put in to a modal matrix $\Phi = [\mathbf{X}_1, \mathbf{X}_2 \ldots, \mathbf{X}_N]$ and are mass normalised to give $\Phi^T M \Phi = I$. Because the system is assumed to be linear, its characteristics can be determined once prior to any aeroelastic calculations.

Equation 2.76 can be transformed into modal space by using $\mathbf{x} = \Phi\eta$ where η is the modal coordinate. First by premultiplying by Φ^T and then substituting $\mathbf{x} = \Phi\eta$ into Equation 2.76 to get

$$M_\eta \ddot{\eta} + C_\eta \dot{\eta} + K_\eta \eta = \Phi^T \mathbf{f} \tag{2.81}$$

where $M_\eta = \Phi^T M \Phi$ is the modal mass matrix, $C_\eta = \Phi^T C \Phi$ is the modal damping matrix and $K_\eta = \Phi^T K \Phi$ is the modal stiffness matrix. The modal mass and stiffness matrices are diagonal because the modes of vibration are orthogonal with respect to the mass and stiffness matrices. The modal damping matrix is diagonal if the damping is proportional. By ignoring damping the equation for the i^{th} mode is

$$\ddot{\eta}_i + \omega_i^2 \eta_i = \mathbf{\Phi}_i^T \mathbf{f_s} \tag{2.82}$$

where $\mathbf{f}_s$ is the external force vector acting on the structure. This equation can be solved for η_i using a Runge-Kutta scheme and the structural deformation at a given time step with p modes is given by

$$\mathbf{x} = \sum_{i=1}^{p} \mathbf{\Phi}_i \eta_i \tag{2.83}$$

2.8 Schur Code

Aeroelastic calculations can be simulated by coupling the fluid and the structural solvers together and marching through time. This method is computationally expensive. The Schur solver views the problem of computing flutter onset as a stability problem for a steady state of the coupled problem [41]. The semi-discrete form of the coupled CFD-CSD system is written as

$$\frac{d\mathbf{w}}{dt} = \mathbf{R}(\mathbf{w}, \mu) \tag{2.84}$$

where

$$\mathbf{w} = [\mathbf{w}_f, \mathbf{w}_s]^T \tag{2.85}$$

is a vector containing the fluid unknowns ($\mathbf{w}_f$) and the structural unknowns ($\mathbf{w}_s$), and

$$\mathbf{R} = [\mathbf{R}_f, \mathbf{R}_s]^T \tag{2.86}$$

is a vector containing the fluid residual ($\mathbf{R}_f$) and the structural residual ($\mathbf{R}_s$). The residual also depends on a parameter μ (in this case μ is altitude) which is independent of $\mathbf{w}$. An equilibrium $\mathbf{w}_0$ of this system satisfies $\mathbf{R}(\mathbf{w}_0, \mu) = 0$.

The linear stability of equilibria of Equation 2.84 is determined by eigenvalues of the Jacobian matrix $J = \partial\mathbf{R}/\partial\mathbf{w}$. The Schur solver does a stability analysis based on the coupled system Jacobian which includes the Jacobian of the CFD residual with respect to the CFD and structural unknowns. The calculation of the Jacobian J is most conveniently done by partitioning the matrix as

$$J = \begin{bmatrix} \frac{\partial\mathbf{R}_f}{\partial\mathbf{w}_f} & \frac{\partial\mathbf{R}_f}{\partial\mathbf{w}_s} \\ \frac{\partial\mathbf{R}_s}{\partial\mathbf{w}_f} & \frac{\partial\mathbf{R}_s}{\partial\mathbf{w}_s} \end{bmatrix} = \begin{bmatrix} J_{ff} & J_{fs} \\ J_{sf} & J_{ss} \end{bmatrix} \tag{2.87}$$

The details of the Jacobian calculation are given in references [39] and [40].

It is conventional in aircraft aeroelasticity for the structure to be modelled by a small number of modes, which leads to the number of the fluid unknowns being far greater than the structural unknowns. This means that the Jacobian matrix has a large sparse block J_{ff} surrounded by thin strips for J_{fs} and J_{sf}. As described in reference [41] the stability calculation is formulated as an eigenvalue problem, focussing on eigenvalues of the coupled system that originate from the uncoupled block J_{ss}.

The coupled system eigenvalue problem is written as

$$\begin{bmatrix} J_{ff} & J_{fs} \\ J_{sf} & J_{ss} \end{bmatrix} \mathbf{p} = \lambda\mathbf{p} \tag{2.88}$$

where $\mathbf{p} = [\mathbf{p}_f, \mathbf{p}_s]^T$ and λ are the complex eigenvector and eigenvalue respectively. The eigenvalue λ (assuming it is not an eigenvalue of J_{ff}) satisfies [56] the nonlinear eigenvalue problem

$$S(\lambda)\mathbf{p}_s = \lambda\mathbf{p}_s \tag{2.89}$$

where $S(\lambda) = J_{ss} - J_{sf}(J_{ff} - \lambda I)^{-1} J_{fs}$.

The nonlinear Equation 2.89 is solved using Newton's method. Each iteration requires the formation of the residual, $S(\lambda)\mathbf{p}_s - \lambda\mathbf{p}_s$ and its Jacobian matrix. The calculation of the correction matrix, $J_{sf}(J_{ff} - \lambda I)^{-1}J_{fs}$, is required to form the Jacobian matrix with respect to $\mathbf{p}_s$ and λ. This can be achieved through $2n$ solutions of a linear system against $J_{ff} - \lambda I$, one for each column of J_{sf} with n being the number modes retained. These solutions are then multipled against J_{sf}. Now, for each value of the bifurcation parameter, there are multiple solutions of the nonlinear system in Equation 2.89, and so the cost of forming the correction matrix at each Newton step, for each solution and for a range of structural parameters becomes too high. To overcome this the expansion

$$(J_{ff} - \lambda I) = J_{ff}^{-1} + \lambda J_{ff}^{-2} + \lambda^2 J_{ff}^{-3} + \dots \tag{2.90}$$

is used where λ must be small for the series to converge. Note that this assumption is not restrictive since we assume that the eigenvalue we are calculating is a small change from the eigenvalue λ_0 of J_{ss}. Then λ_0 can be used as a shift to the full system eigenvalue by replacing J_{ff} by $J_{ff} - \lambda_0 I$ and J_{ss} by $J_{ss} - \lambda_0 I$. This modifies the nonlinear eigenvalue problem in Equation 2.89 by redefining $S(\lambda) = (J_{ss} - \lambda_0 I) - J_{sf}(J_{ff} - \lambda_0 I - \lambda I)^{-1}J_{fs}$. The series approximation then becomes

$$(J_{ff} - \lambda_0 I - \lambda I)^{-1} = (J_{ff} - \lambda_0 I)^{-1} + \lambda(J_{ff} - \lambda_0 I)^{-2} + \lambda^2(J_{ff} - \lambda_0 I)^{-3} + \dots \tag{2.91}$$

When the shifted problem is solved for λ, the eigenvalue of the original system is then $\lambda_0 + \lambda$. The terms $(J_{ff} - \lambda_0 I)^{-1}J_{fs}$, $\lambda(J_{ff} - \lambda_0 I)^{-2}J_{fs}$ can be pre-computed to yield the series approximation which can then be evaluated for any λ at virtually no computational cost.

This method is referred to as the Schur method. The series approximation is used for approximating the Jacobian matrix of the residual from Equation 2.89. For the residual the evaluation of $S(\lambda)\mathbf{p}_s - \lambda\mathbf{p} - s$ can be made based on a series approximation at virtually no additional cost after the series matrices are formed. This formulation leads to a very efficient method of tracing the aeroelastic eigenvalues as functions of altitude, which in turn provides stability boundaries.

Chapter 3

Transformation Methods

3.1 Introduction

3.1.1 The Transformation Problem

Computational aeroelasticity (CAE) refers to the coupling of computational fluid dynamics (CFD) and computational structural dynamics (CSD) to perform aeroelastic calculations. To solve the coupled aeroelastic problem two approaches have emerged.

The first is called the monolithic approach that uses a tailored aero-structural solver. In this approach the governing equations are reformulated combining the fluid and structural equations, which are then solved and integrated in time simultaneously. While using a fully coupled procedure, one must deal with fluid equations in an Eulerian reference system, and structural equations in a Lagrangian system. A problem with this type of scheme is that the matrices to be solved are several orders of magnitude stiffer for the structural system compared to the fluid system, which makes them difficult to solve [57]. There are examples of this approach [58, 59], but they are limited to 2D problems.

The second approach is called the partitioned approach. In the partitioned approach separate aerodynamic and structural solvers are used, which are coupled through the wetted surface. This requires the aerodynamic loads to be transferred to the structure and the structural deflections to be transferred to the CFD grid. This is complicated by the CFD requiring an accurate description of the surface geometry, but the structural model is usually defined on a simplified geometry, such as a plate, wing-box or beam. Figure 3.1 shows a typical CFD surface grid and a structural model. Despite adequately describing the important structural dynamics, this structural simplification produces the problem that there is a mismatch between the fluid and structural discretisation of the interface between the two models. This means that projection and extrapolation are usually required in addition to interpolation to transfer data. To solve this problem one can either use a high resolution structural model, resulting in longer computation time, or use a transformation method. Collectively the reconstruction of the fluid surface grid node locations and velocities from the structural model, and the transfer of forces from the fluid surface grid to the structural grid, is referred to as transformation. There are several ways in which the shape of the wing can be altered in a non-physical manner (sectional and planform). Reviews of transformation methods can be found in references [10, 60, 61, 62]. Farhat *et al.* [38] simplified the transfer problem of the F-16 fighter by defining both the CFD and structure on the same surface using an unstructured Euler CFD solver and a detailed structural model. However detailed structural models are not always available and can be difficult to tune to ground vibration tests.

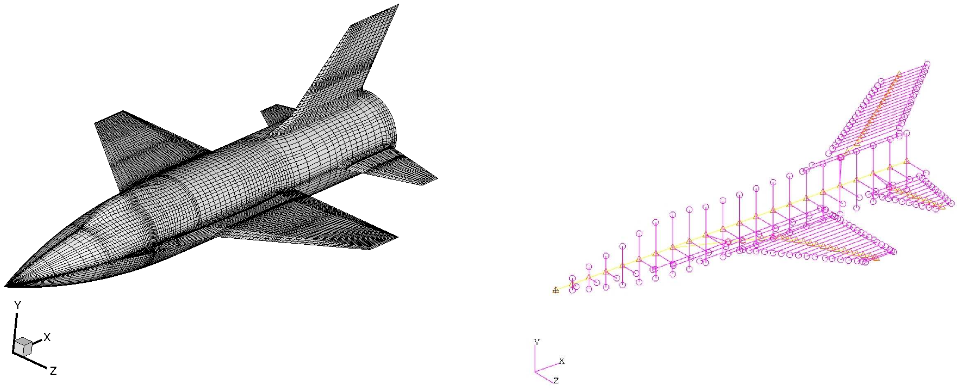

(a) CFD surface grid (b) CSD grid

Figure 3.1: Comparison of typical CFD/CSD grids

Transformation methods can be grouped into two groups, local and global methods. Each have their own advantages and disadvantages. Local methods often depend on connectivity between the aerodynamic surface and the structural model and do not always give a smooth surface. However as the name suggests, they only use local information and have low memory requirements. Global methods have higher memory requirements and can produce non-local effects, but always provide a smooth surface.

3.1.2 Notation

The following notation will be used throughout

- Structural model
    - Contains n_s grid points

  - $\mathbf{x}_s = (x_{s_1} \cdots x_{s_{n_s}})^T$ is the set of structural grid points (used for either x, y or z)
  - $\mathbf{dx}_s = (dx_{s_1} \cdots dx_{s_{n_s}})^T$ are the displacements calculated at the grid points by the structural solver (used for either dx, dy or dz)
  - $\mathbf{F}_s = (F_{s_1} \cdots F_{s_{n_s}})^T$ are the forces calculated during the transformation process (used for either F_x, F_y or F_z)

- CFD model
  - Contains n_a grid points
  - $\mathbf{x}_a = (x_{a_1} \cdots x_{a_{n_a}})^T$ is the set of aerodynamic grid points (used for either x, y or z)
  - $\mathbf{dx}_a = (dx_{a_1} \cdots dx_{a_{n_a}})^T$ are the displacements calculated during the transformation process (used for either dx, dy or dz)
  - $\mathbf{F}_a = (F_{a_1} \cdots F_{a_{n_a}})^T$ are the forces calculated at the grid points by the CFD solver (used for either F_x, F_y or F_z)

3.1.3 Requirements

There are a number of requirements for a transformation method to satisfy given in the literature [2, 10, 62].

1. Conservation of energy.
2. Conservation of total force and moment.
3. Exact recovery of translation and rotation.
4. Force and displacement association.
5. Smoothness.
6. Complex geometries.
7. Minimal memory requirements.
8. Minimal CPU requirements.

These are now elaborated upon.

Conservation of energy

Conservation of energy can be achieved through the use of the principle of virtual work. The virtual work W is defined by

$$W = \mathbf{dx}_s^T \mathbf{F}_s = \mathbf{dx}_a^T \mathbf{F}_a \tag{3.1}$$

where $\mathbf{dx}$ is displacement vector and $\mathbf{F}$ is force vector. The subscript a denotes aerodynamic nodes and s structural nodes. Defining a transformation matrix T that transforms the structural displacements to the aerodynamic displacements in a linear fashion as

$$\mathbf{dx}_a = T\mathbf{dx}_s \tag{3.2}$$

Then the requirement for energy conservation can be satisfied by substituting Equations 3.2 into Equation 3.1 so the relationship between the forces is

$$\mathbf{F}_s = T^T \mathbf{F}_a \tag{3.3}$$

Using this method the global conservation of energy is satisfied regardless of the method that is used to fill the transformation matrix [62].

Conservation of total force and moment

Conservation of the global forces can be written as

$$\sum_{i=1}^{n_s} F_{s_i} = \sum_{i=1}^{n_a} F_{a_i} \tag{3.4}$$

Exact recovery of translation and rotation

If the structural grid is subject to a rigid body motion, the displacement transfer should result in the same motion for the aerodynamic surface grid. Any transformation method should be able to accurately resolve rigid body motions without introducing any distortion.

Force and displacement association

If all the fluid and structural nodes coincide exactly then the forces and displacements must be associated exactly. In this case the transformation matrix produced by the transformation method should be an identity matrix. This will only hold if both the structural and aerodynamic surface meshes coincide. If any fluid and structural nodes coincide at the beginning of the simulation, then these points should remain attached throughout the simulation.

Smoothness

If the deformed structural grid is smooth then the aerodynamic surface grid once deformed should also be smooth. If the transformation method artificially generates surface distortions (i.e. ripples, ridges, spikes etc.) it could lead to unexpected results like premature separation or additional shockwaves. There is also the possibility of the CFD solver failing, especially if the grid folds inside the aircraft for example at the wing-fuselage junction. If the load distribution on the aerodynamic surface grid is smooth then the transformed load distribution on the structural grid should also be smooth. However if there are discontinuities in the flow solution (i.e. shock-waves) then these should be accurately transferred. Here smooth is defined in a general sense, but for the CFD solution the surfaces need to be C^2 continuous to avoid pressure blips. However the local transformation methods in general are only C^0 continuous, the effect of this lack of sufficient continuity will be explored in a later chapter.

Complex geometries

When applied to a complex geometry the scheme must not introduce any holes at component junctions. The scheme should also be able to cope with control surfaces and stores.

Memory requirements

The methods should use a minimal amount of memory, since high fidelity simulations can involve large CFD and structural grids. For example a full aircraft CFD surface grid can have in the region of $n_a = 2 \times 10^5$ and a high fidelity structural model can have in the region of $n_s = 1.8 \times 10^4$. Although the use of beam stick models for aeroelastics is common, which reduces the number of structural nodes to the region of $n_s = 200$. Using a beam stick model and a global transformation method can lead to a matrix of around $6 \times n_s \times n_a = 2.4 \times 10^8$ non-zero values. The larger the memory requirements for the transformation method the smaller the simulation size is that can be run.

CPU time

The CPU time that the transformation method requires should be small in comparison to the CFD calculation, to make the scheme feasible for use in a closely coupled system.

3.1.4 Review

Transformation started to gain interest in the late 1960's as panel methods and finite element structural models usage became widespread. The initial methods used were beam and surface splines such as those published by Done [63].

In 1972 infinite plate splines (IPS) were proposed by Harder and Desmarais [52] and use the solution of a multiply-supported infinite plate for the data transfer. This is still a popular method and is used in commercial finite element packages such as NASTRAN [64] and ASTROS [65]. This method was an attempt to step away from previous methods, which required a large amount of user input to choose the best structural and aerodynamic points to get an accurate solution. Also in the seventies a number of methods were proposed in the field of mathematics to solve the problem of scattered data interpolation, including Hardy's multiquadrics (MQ) [66] and inverse multiquadrics (IMQ) and Duchon's thin plate splines (TPS) [67]. However these new methods were not applied to the aeroelastic transformation problem until much later.

Franke published a paper in 1982 [68] that reviewed all the methods known at the time for scattered data interpolation. From this paper the MQ and TPS were noted to perform very well. Murti and Valliappan published a paper in 1986 on inverse isoparametric mapping (IIM) [69] for the application of remeshing for crack propagation and this would later be used as a transformation method. At the end of the eighties Appa published a paper on finite plate splines (FPS) [70], which was aimed at improving on the infinite plate splines of Harder and Desmarais. This paper also introduced the concept of virtual surfaces.

The nineties saw an explosion in publications on the transformation problem. In 1990 Kansa [71] published a series of papers on MQ for use in CFD. In 1992 Pidaparti [72] published the first application of IIM to an aeroelastic problem. A significant contribution to the field of transformation methods in the nineties was a paper by Smith *et al.* [60]. This paper reviewed the transformation methods IPS, FPS, MQ, TPS, IIM, and NUBS through the use of 260 test cases. The main conclusions were that TPS was the most accurate, robust and cost-efficient of all methods tested and IIM performed very well, but requires an extension to 3D and the elimination of its dependency on structured grids. It is also recommended that multiple methods should be available in any software package. In 1996 Samareh [73] presented a method for load transfer based upon NURBS. Cebral and Löhner [74] published a conservative, monotonic, adaptive Gaussian quadrature load transfer method. In 1998 Chen [47] presented a new boundary element method (BEM).

In the next decade the new methods that were introduced were radial basis functions (RBF) and constant volume tetrahedron (CVT). Radial basis functions have been used for transfer for a long time, since IPS, TPS and MQ can be written in this form. Beckert and Wendland [75] presented radial basis functions to aeroelastics in 2001 using a number of different basis functions using compact support. This methodology has been improved upon in a series of papers [2, 50, 76, 77, 78]. Constant volume tetrahedron was proposed by Goura [79] in 2001 and has subsequently been improved upon [7, 39, 62]. This is a local method where each aerodynamic node is attached to a structural triangle forming a tetrahedron. As the structural nodes move the out-of plane component is scaled to keep the volume of the tetrahedron constant.

3.2 Types of Structural Models

There are a number of different structural models that can be used in aeroelastic calculations. The simplest are the beam stick models (BSM), these models use a number of beam elements with lumped masses connected together using stiff springs. These models are assumed to be chordwise rigid. An example BSM is shown in Figure 3.2 (a) for the XML12 aircraft test case. The beam elements are shown in black, the rigid bars are shown in magenta and the lumped masses are shown as blue triangles. The rigid bars are used for visualisation and to define additional points to aid the transformation methods. These BSM are still widely used in industry due to the small number of degrees of freedom (DOF) and subsequently the ease of matching the model to ground vibration tests (GVT). These models are also used in the conceptual phase of design because the more complex models are not available until further along in the design process. These models are usually used for transport-type configurations with high aspect ratio wings. Plate models model the lifting surfaces as a plates. An example is shown in Figure 3.2 (b) for the Standard Dynamics Model (SDM) fighter test case. These models are usually used for fighter aircraft with low aspect ratio wings. Wing-box models represent a wing as a wing-box, which only consists of the spars, ribs and skins above and below the ribs and spars, the rest of the structure is treated as dead weight and modeled as lumped masses. These models are also assumed to be chordwise rigid. An example is shown in Figure 3.2 (c) for the Goland wing test case. These are typically used for transport-type aircraft whose wings are constructed in this way. Shell models represent the aircraft using shell elements and usually model the spars, ribs and the full skin. An example is shown in Figure 3.2 (d) for the ARW-2 wing test case. Full finite element models using bricks can be used, but are quite rare due to the large number of degrees of freedom that they contain. These models accurately capture the structure, but at a high computational cost and for aeroelastic calculations the other types of structural models can provide the required accuracy at a more reasonable cost. An example is shown in Figure 3.2 (e) for the High Reynolds Number Aero-Structural Dynamics (HIRENASD) wing test case.

This thesis concentrates on the beam stick and wing-box models. Most transfer methods cannot handle beam stick models directly, since beam elements provide displacements and rotations at the beam nodes. It is common to use rigid bars attached to the beam elements to provide additional points with displacements. Depending on the transfer method to be used these additional points can be triangulated or used directly.

3.3 Existing Transformation Methods

Common transformation methods are presented in their approximate historical order.

3.3.1 Multiquadric-Biharmonic

The multiquadric (MQ) was first derived by Hardy [66] for the approximation of geographical surfaces and was applied to CFD by Kansa [71]. Hardy assumed that any function $s(x)$ could be written as an expansion of n continuously differentiable basis functions ϕ,

$$s(\mathbf{x}) = \sum_{i=1}^{n} \alpha_i \phi(\|\mathbf{x} - \mathbf{x}_i\|) \tag{3.5}$$

where $\mathbf{x} = (x, y, z)^T$ in this case, $\phi(\|\mathbf{x}\|) = [\|\mathbf{x}\|^2 + r^2]^{1/2}$ and r^2 is a non-zero parameter. The coefficients α_i can be found by solving a set of linear equations in terms of the basis functions. This can be written in a matrix form and then be used to calculate a transformation matrix. The form of this equation is very similar to radial basis functions (see Section 3.3.8), but without a polynomial. To generate the transformation matrix a matrix C_{ss} requires inverting. The higher the condition number the more accurate the resulting transformation matrix will be, but the C_{ss} matrix is harder to invert. This means a compromise needs to be reached between having a condition number small enough to invert the matrix and big enough to achieve the desire accuracy. The parameter r^2 also has an effect on the condition number, as this parameter is increased the condition number increases and therefore accuracy until the matrix becomes singular [71].

Improvements

- **Vary Parameter** r^2
  Kansa [71] found that the key factor in obtaining an accurate result from

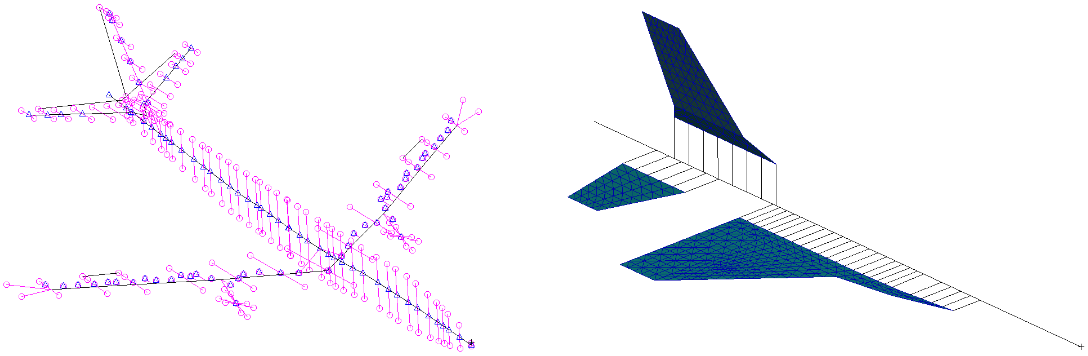

(a) Beam stick model (XML12)

(b) Plate model (SDM)

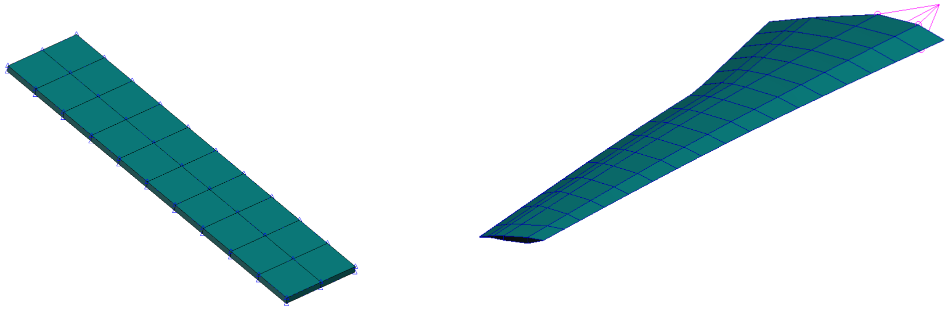

(c) Wing-box model (Goland wing)

(d) Shell model (ARW-2)

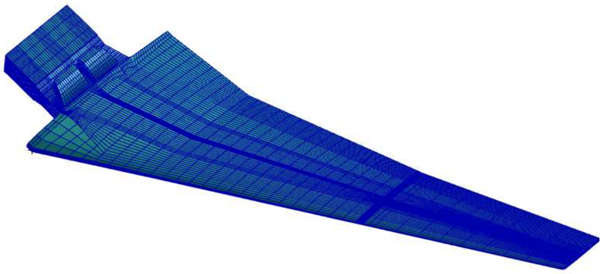

(e) Full finite element model (HIRENASD)

Figure 3.2: Structural models

MQ was the conditioning of the coefficient matrix. It was found that by varying the parameter r^2 monotonically the accuracy could be improved by reducing the matrix condition number. The value of r^2 for the j^{th} basis function is given by

$$r_j^2 = r_{min}^2 \left(\frac{r_{max}^2}{r_{min}^2}\right)^{\frac{j-1}{n-1}} \qquad j = 1, 2, ..., n \tag{3.6}$$

where r_{min}^2 and r_{max}^2 are input parameters. By carefully choosing the values of r_{min}^2 and r_{max}^2 the transformation can be made more accurate by changing the condition number of the C_{ss} matrix.

- **Unit Sub-domain**
  Kansa [71] also recommended that the data should be mapped onto a unit sub-domain to reduce the errors. One-dimensional problems are mapped on to a unit line, two-dimensional problems are mapped on to a unit square and three-dimensional problems are mapped on to a unit cube. Then if necessary additional rotation and shear transformations were introduced to make the distances more distinct.

- **Domain Decomposition**
  Kansa [71] also recommended using domain decomposition to split the large coefficient matrix into smaller quasi-local problems. This increases the accuracy and computational efficiency.

Observations

MQ performs better than inverse multiquadric (IMQ) where the basis function is $\phi(\|\mathbf{x}\|) = [\|\mathbf{x}\|^2 + r^2]^{-1/2}$ [68]. The main advantages of MQ are that it is infinitely differentiable function and it is accurate in regions where the surfaces are steep. However in regions where surfaces are relatively flat MQ produces a surfaces that is not as smooth as the original surface, this can be improved using a hybrid scheme. Smith *et al.* [60] found that MQ accuracy is case dependent and performs poorly interpolating highly oscillatory functions. It was also found that the parameter r should be kept within certain limits to insure a stable linear system of equations. Finally it was found that the need for scaling was case dependent and that MQ was sensitive to grid resolution.

3.3.2 Infinite Plate Spline

Infinite plate spline (IPS) was proposed by Harder and Desmarais [52] and is used by programs such as NASTRAN [64] and ASTROS [65]. IPS is a special 2D case of TPS [60]. It is based upon the superposition of the solutions for the partial differential equation of equilibrium of an infinite plate. The deflections normal to the plate surface due to n point forces F_i at given locations (x_i, y_i) on the plate can be written as

$$dz(x,y) = a_0 + a_1 x + a_2 y + \sum_{i=1}^{n} F_i r_i^2 \ln r_i^2 \tag{3.7}$$

where $r_i^2 = x_i^2 + y_i^2$. The unknowns, a_k and F_i are obtained from the equilibrium conditions

$$\sum_{i=1}^{n} F_i = \sum_{i=1}^{n} x_i F_i = \sum_{i=1}^{n} y_i F_i = 0 \tag{3.8}$$

and from the given deflections at the n nodes

$$dz_j = a_0 + a_1 x_j + a_2 y_j + \sum_{i=1}^{N} F_i r_{ij}^2 \ln r_{ij}^2 \tag{3.9}$$

where $r_{ij}^2 = (x_i - x_j)^2 + (y_i - y_j)^2$. The derivation of the transformation matrix is given in Appendix A. Then equations 3.2 and 3.3 can be used to calculate the displacements and forces respectively.

Improvements

- **Distributed Loads**
  It was suggested in the original paper by Harder and Desmarais [52] that the solution can be smoothed by using distributed loads. This is achieved by replacing Equation 3.9 with

  $$dz_j = a_0 + a_1 x_j + a_2 y_j + \sum_{i=1}^{N} F_i r_{ij}^2 \ln(r_{ij}^2 + \epsilon) \tag{3.10}$$

  where ϵ is an input parameter. A parameter value of $\epsilon = 0$ is the same as using point loads, Sadeghi *et al.* [62] showed that by using $\epsilon = 20$ the result obtained by IPS was improved.

Observations

IPS requires the aerodynamic points and the structural points to be in the same plane. If the aerodynamic and structural points do not lie on the same plane then they can be projected onto a neutral plane [10]. The deflections for the projected aerodynamic points are then calculated with the original offset being added to the projected points to generate the deflected aerodynamic points. The interpolation function can be differentiated everywhere, the nodes do not need to form a mesh and a minimum of three nodes are required [60]. It is a global method and as such generates a large transformation matrix. Extrapolations to the edges of the planform from the interior structural grid points do not always appear to be reliable. Figure 3.3 shows that IPS is unable to recover rigid rotations exactly. A circle is driven by a rigid bar and as the bar is rotated the circle is skewed. Smith *et al.* [60] found IPS to be sensitive to the grid resolution and that the accuracy was only adequate.

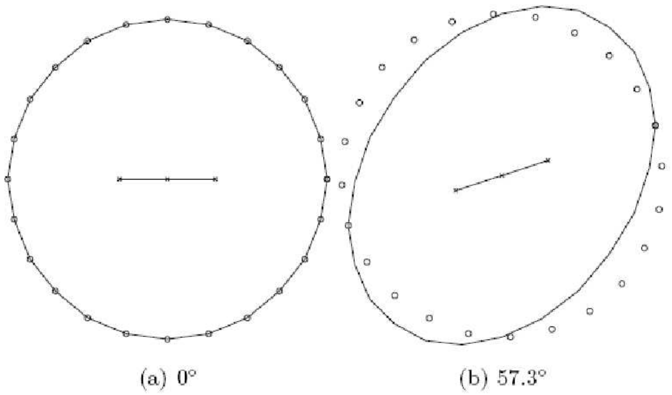
(a) 0°
(b) 57.3°

Figure 3.3: A circle of points rigidly rotated by a bar using IPS (from ref. [10])

3.3.3 Thin-Plate Splines

Thin-plate splines (TPS) of Duchon [67] provide a means to characterise an irregular surface by using functions that minimise an energy functional. This method is very similar to RBF and MQ, however uses a different basis function. IPS is a 2D special case of TPS. The basis function for TPS is

$$\phi(\|\mathbf{x}\|) = \|\mathbf{x}\|^2 \ln \|\mathbf{x}\| \tag{3.11}$$

where $\mathbf{x} = (x, y, z)^T$ in this case. This is solved in the same way as RBF with the linear polynomial (see Section 3.3.8).

Improvements

- **Sub-domaining**
  Smith *et al.* [60] stated that TPS outperformed IPS when the data be mapped onto a number of sub-domains. Then if necessary additional rotation and shear transformations were introduced to make the distances more distinct. This mapping on to a number of sub-domains also causes the transformation to be more localised.

Observations

Kamakoti et al [61] observed that since splines are invariant to translation and rotation, it is a useful tool for moving and flexible surfaces. Smith et al [60] commented that if TPS is used globally in 2D it has all the same limitations as IPS, but when used in 3D outperforms IPS.

3.3.4 Inverse Isoparametric Mapping

Inverse Isoparametric Mapping (IIM) was proposed by Murti and Valliappan [69] and was applied by Pitaparti [72]. The same shape functions N_i are used for both the aerodynamic grid points and the structural deformation. Each aerodynamic node is projected to a quadrilateral element. A pair of generalised coordinates (ξ, η) are defined on the quadrilateral using shape functions so that

$$x_a = \sum_{i=1}^{n} N_i(\xi, \eta) x^e_{s_i} \tag{3.12}$$

$$y_a = \sum_{i=1}^{n} N_i(\xi, \eta) y^e_{s_i} \tag{3.13}$$

where n is the number of nodes for the element. The element is assumed to lie in the $x - y$ plane and the superscript e indicates the structural node is a member of that element. The shape function for a quadrilateral element [80] is given by

$$\begin{gathered} N_1(\xi,\eta) = (1-\xi)(1-\eta)/4 \\ N_2(\xi,\eta) = (1+\xi)(1-\eta)/4 \\ N_3(\xi,\eta) = (1+\xi)(1+\eta)/4 \\ N_4(\xi,\eta) = (1-\xi)(1+\eta)/4 \\ \xi, \eta \in [-1, 1] \end{gathered} \tag{3.14}$$

Observations

IIM is the most accurate among all methods for interpolation [61] and can be derived for different types of elements such as 8-noded quadrilaterals. IIM is only valid for 2D interpolations and it is commented that no extrapolation is possible purely using IIM [81]. However Pidaparti [72] showed that it was possible to use this transformation method with common extrapolation techniques to extrapolate data to control surfaces. This method is only C^0 continuous in displacement between quadrilateral elements, but since the interpolation is bilinear it is an improvement over weighted triangles.

3.3.5 Finite Plate Spline

The Finite Plate Spline (FPS) proposed by Appa [70] uses a finite plate instead of the infinite plate of Harder and Desmarais [52]. This was applied to a fighter aircraft wing by Guruswamy and Byun [57]. This method introduced the concept of a virtual surface, which is a surface that passes through the aerodynamic and structural points with the same planform as the aerodynamic surface. The virtual surface is discretised into finite bending elements. A set of constraints are established such that when deformed, the virtual surface passes through the deformed structural points. Appa [70] suggested that C^1 shape functions should be used, since the C^0 did not give satisfactory results. As such the following transformation matrix can be derived [60, 70]

$$T = \Psi_a \left[\alpha^{-1} K + \Psi_s^T \Psi_s\right]^{-1} \Psi_s^T \tag{3.15}$$

where K is the stiffness matrix of the virtual surface, Ψ_s is the displacement mapping from the virtual surface to the structural grid, Ψ_a is the displacement mapping from the virtual surface to the aerodynamic grid and α is the penalty parameter. Then equations 3.2 and 3.3 can be used to calculate the displacements and forces respectively.

Observations

FPS can accommodate changes in models or meshes, however it is a 2D method and was shown to be CPU and memory intensive due to the virtual surface [60].

3.3.6 Non-Uniform Rational B-Splines

The method proposed by Samareh [82] uses NURBS to transfer the forces and displacements between the CFD and structural models. The concept behind this method is to have one main representation of the aircraft in the form of NURBS surfaces. This single representation can be discretised into a number of other domains (CFD,CSD, etc.). Each domain is solved and transfers data to and from the NURBS representation, shown in Figure 3.4. More details can be found in the papers by Samareh [11, 82].

Observations

This requires the structural model to be a full finite element model that shares the same surface as the CFD, which will add to the cost. This method requires access to a CAD package.

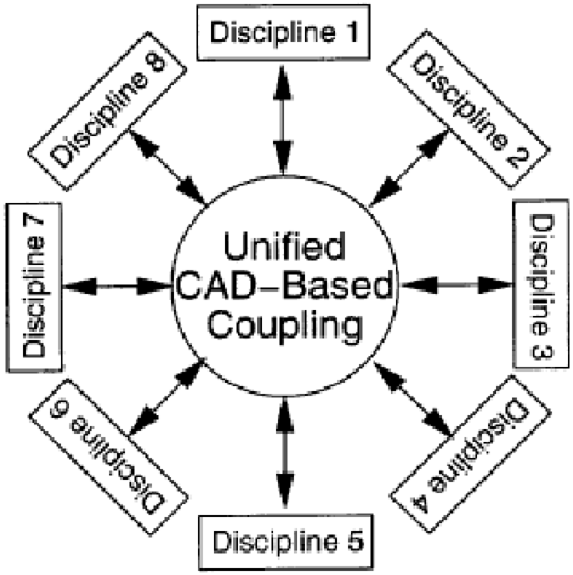

Figure 3.4: NURBS approach [11]

3.3.7 Boundary Element Method

The Boundary element method (BEM) was proposed by Chen and Jadic [47]. BEM is based upon the elastostatic boundary element method with a BEM solver being devised to generate a transformation matrix. In this approach the fluid surface mesh forms the external boundary of an elastic homogeneous body with the structural nodes as internal points as shown in Figure 3.5.

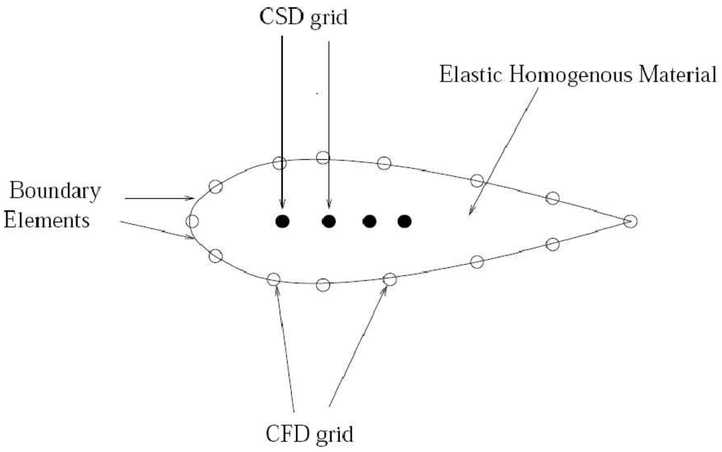

Figure 3.5: Boundary element method [10]

Observations

Sadeghi et al [62] observed that BEM recovers the exact transformation of rigid body motion and produces a smooth transformation, because all grid points are connected within continuous elastic bodies, and because of the conditions of minimum strain applied for the inverse BEM. The linear approach allows for the formulation of a global transformation matrix, which is used for conservative displacement and force transformations. BEM can also be used for CFD volume grid deformation. Rampurawala [10] states that BEM requires more memory than IPS and as such is memory intensive.

3.3.8 Radial Basis Functions

The radial basis function interpolant [75] has the form

$$s(\mathbf{x}) = \sum_{i=1}^{N} \alpha_i \phi(\|\mathbf{x} - \mathbf{x}_i\|) + p(\mathbf{x}) \tag{3.16}$$

where $s(\mathbf{x})$ is the function to be evaluated at $\mathbf{x}$, $\phi(\|\mathbf{x}\|)$ is the basis function, the index i identifies the centres for the RBF and $\mathbf{x}_i$ is the location of that centre (centres are usually the structural points). The linear polynomial $p(\mathbf{x})$ is used to ensure that translations and rotations are recovered. The coefficients α_i are found by requiring the exact recovery of the structural node positions. The polynomial in the x-direction is given by

$$p_x(\mathbf{x}) = \gamma_{x0} + \gamma_{xx}x + \gamma_{xy}y + \gamma_{xz}z \tag{3.17}$$

When the polynomials are included in the system, the additional requirement is

$$\sum_{i=1}^{N} \alpha_i q(\mathbf{x}) = 0 \tag{3.18}$$

for all polynomials $q(\mathbf{x})$ with degree less than or equal to $p(\mathbf{x})$. Equation 3.16 can be recast into a transformation matrix, as shown in Appendix C. Then equations 3.2 and 3.3 can be used to calculate the displacements and forces respectively.

Basis Functions

There is an infinite choice of basis functions that can be used. A selection of basis functions from the literature are given in Table 3.1, where $(.)_+ = max(0, .)$ and in the Euclid's Hat basis function $r = 2\rho$ [76].

Table 3.1: Basis Functions $\phi(\|\mathbf{x}\|)$ (taken from [2])

Basis Function	Definition
Gaussian (G)	$\exp^{-\alpha\|\mathbf{x}\|^2}$
Thin Plate Spline (TPS)	$\|\mathbf{x}\|^2 \ln \|\mathbf{x}\|$
Multiquadric (MQ)	$(c^2 + \|\mathbf{x}\|^2)^{1/2}$
Inverse Multiquadric (IMQ)	$(c^2 + \|\mathbf{x}\|^2)^{-1/2}$
Wendland's C0 (C0)	$(1 - \|\mathbf{x}\|)_+^2$
Wendland's C2 (C2)	$(1 - \|\mathbf{x}\|)_+^4 (4\|\mathbf{x}\| + 1)$
Wendland's C4 (C4)	$(1 - \|\mathbf{x}\|)_+^6 (35\|\mathbf{x}\|^2 + 18\|\mathbf{x}\| + 3)$
Wendland's C6 (C6)	$(1 - \|\mathbf{x}\|)_+^8 (32\|\mathbf{x}\|^3 + 25\|\mathbf{x}\|^2 + 8\|\mathbf{x}\| + 1)$
Euclid's Hat (EH)	$\pi \left(\left(\frac{1}{12}\|\mathbf{x}\|^3\right) - r^2\|\mathbf{x}\| + \left(\frac{4}{3}r^3\right)\right)$

Improvements

- **Norm Biasing**

  The definition of the norm has a significant impact upon the interpolation, which is the input for the basis function. Typically, the Euclidean norm is used, shown below

  $$\|\mathbf{x} - \mathbf{x}_i\| = \sqrt{(x - x_i)^2 + (y - y_i)^2 + (z - z_i)^2} \tag{3.19}$$

  The modification to the norm proposed by Rendall and Allen [2] is

  $$\|\mathbf{x} - \mathbf{x}_i\| = \sqrt{k_x(x - x_i)^2 + k_y(y - y_i)^2 + k_z(z - z_i)^2} \tag{3.20}$$

  where the coefficients k_x, k_y and k_z have the effect of deforming the sphere of influence of each centre. It was shown in [2] that by choosing values for k_x, k_y, k_z that do not equal one improved the trailing edge interpolation.

- **Support Radius**

  The support radius is defined as $\phi(\|\mathbf{x}\|/\rho)$ where ρ is the support radius and ϕ is any basis function. This allows the control of the area of influence of each centre. A very large support radius smooths the deformation over a large area, whereas a small support radius makes it much more localised. The larger the support radius the higher the condition number of the C_{ss} matrix, which leads to higher accuracy when there the polynominals are not used. However when the polynomials are used the matrix sparsity pattern is more complex and the accuracy is increased as the support radius is decreased. From numerical tests the wing used effects the whether the condition number increases or decreases as the support radius decreases, even though the error decreases for both wings tested. The reason behind this need further work.

- **Data Storage**
  Rendall and Allen [2] suggest using a threshold value above which an element of the matrix is stored. This reduces the storage cost associated with this method.

- **Pointwise Partition of Unity**
  Rendall and Allen [78] proposed the pointwise partition of unity, which is an improvement of the partition of unity of Wendland [83] and Ahrem et al [76]. The global solution is generated from a weighted combination of local solutions. The local solutions are for each aerodynamic point deformed by a small number of the closest structural points. This results in a much faster solution with lower storage requirements and a more physical force distribution.

- **Data Reduction**
  Rendall and Allen [50] developed a method that uses a greedy algorithm to minimise the number of points used as centres whilst minimising the error. This works by starting with a small number of centres and then applying a unit translation in the x, y and z directions. This gives a measure of the error introduced by using a subset of the centres. If the error is above a threashold amount then an additional centre is added at the loction of the maximum error, this is repeated until the error is below the target error.

Observations

The great strength of RBF is the fact that the same code can be used to perform the coupling and/or the mesh movement on structured and unstructured meshes. RBF is an interpolation scheme for use on scattered data sets and as such is not based upon the structural dynamics or connectivity. Unfortunately this method is computationally and memory intensive, since the matrix C_{ss} is n_s^2 in size and if mesh motion is also required the memory required is $n_s \times n_v$. Another disadvantage is the large number of options that can be changed, such as basis functions, norm biasing and support radius. There is a problem reported by Rendall and Allen [2] and Ahrem et al [76] where camber is induced at the trailing edge of a wing especially near the tip, this is probably due to extrapolation. The improvements given above address most of the issues at the cost of a more complex implementation.

3.3.9 Constant Volume Tetrahedron

Constant Volume Tetrahedron (CVT) was proposed by Goura [79]. In this method each aerodynamic node is assigned to a structural element defined by three structural grid points, shown in Figure 3.6. The position of the aerodynamic node $\mathbf{x}_{a,l}$ is given by

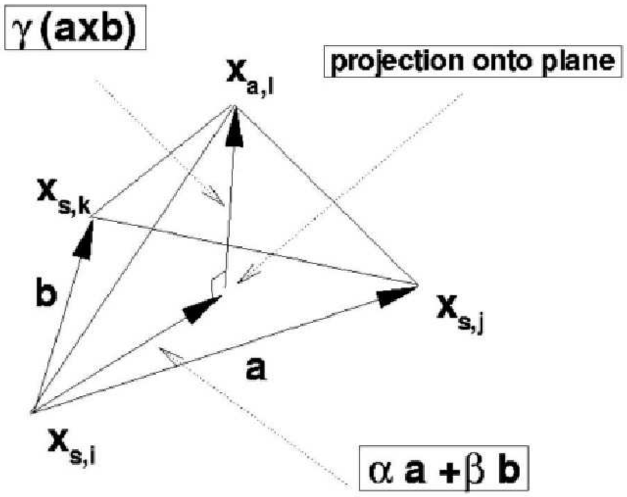

Figure 3.6: Constant volume tetrahedron [10]

$$\mathbf{x}_{a,l} - \mathbf{x}_{s,i} = \alpha\mathbf{a} + \beta\mathbf{b} + \gamma\mathbf{d} \tag{3.21}$$

where $\mathbf{a} = \mathbf{x}_{s,j} - \mathbf{x}_{s,i}$, $\mathbf{b} = \mathbf{x}_{s,k} - \mathbf{x}_{s,i}$ and $\mathbf{d} = \mathbf{a} \times \mathbf{b}$. The constants are calculated using

$$\alpha = \frac{(\mathbf{b}.\mathbf{b})(\mathbf{a}.\mathbf{c}) - (\mathbf{a}.\mathbf{b})(\mathbf{b}.\mathbf{c})}{(\mathbf{a}.\mathbf{a})(\mathbf{b}.\mathbf{b}) - (\mathbf{a}.\mathbf{b})(\mathbf{a}.\mathbf{b})} \tag{3.22}$$

$$\beta = \frac{(\mathbf{a}.\mathbf{a})(\mathbf{b}.\mathbf{c}) - (\mathbf{a}.\mathbf{b})(\mathbf{a}.\mathbf{c})}{(\mathbf{a}.\mathbf{a})(\mathbf{b}.\mathbf{b}) - (\mathbf{a}.\mathbf{b})(\mathbf{a}.\mathbf{b})} \tag{3.23}$$

$$\gamma = \frac{(\mathbf{c}.\mathbf{d})}{(\mathbf{d}.\mathbf{d})} \tag{3.24}$$

The volume of the tetrahedron is held constant during the calculation by recalculating γ. The method can be linearised in the structural displacements [79], giving

$$\mathbf{dx}_{al} = A\mathbf{dx}_{s,i} + B\mathbf{dx}_{s,j} + C\mathbf{dx}_{s,k} \tag{3.25}$$

where

$$\begin{aligned} A &= I - B - C \\ B &= \alpha I - \gamma UV(\mathbf{b}) \\ C &= \beta I - \gamma UV(\mathbf{a}) \\ U &= I - \tfrac{2}{d^2} D(\mathbf{d}) S(\mathbf{d}) \end{aligned} \tag{3.26}$$

d is the magnitude of $\mathbf{d}$.

$$V(\mathbf{z}) = \begin{pmatrix} 0 & -z_3 & z_2 \\ z_3 & 0 & -z_1 \\ -z_2 & z_1 & 0 \end{pmatrix} \tag{3.27}$$

$$D(\mathbf{z}) = \begin{pmatrix} z_1 & 0 & 0 \\ 0 & z_2 & 0 \\ 0 & 0 & z_3 \end{pmatrix} \tag{3.28}$$

$$S(\mathbf{z}) = \begin{pmatrix} z_1 & z_2 & z_3 \\ z_1 & z_2 & z_3 \\ z_1 & z_2 & z_3 \end{pmatrix} \tag{3.29}$$

Equation 3.25 can be written as a transformation matrix, which can be recalculated each time step to reduce error. Then equations 3.2 and 3.3 can be used to calculate the displacements and forces respectively.

Improvements

- **Selection of the Structural Elements**

  For this method the selection of the correct structural element to map the aerodynamic node to is critical. This mapping is done as a preprocessing step and is provided as an input to the solver. The original method of selecting the structural element was to minimise the distance between the projected fluid point and the structural element centroid. This could result in the fluid point being above a structural triangle that it was not mapped to, since that neighbouring centroid was closer [7].

  To minimise the amount of extrapolation required the following modification was made. Each structural element was split into three subtriangles. The area of the *jth* structural element ABC (Δ_{ABC}) along with the subtriangles APB (Δ_{APB}), BPC (Δ_{BPC}), APC (Δ_{APC}) are calculated where P is the projected aerodynamic node and the following function is minimised

  $$S_{\Delta_j} = |\Delta_{ABC} - \Delta_{APB} - \Delta_{BPC} - \Delta_{APC}| \tag{3.30}$$

  If $S_{\Delta_j} = 0$, the point is above the assigned element, interpolation will be used. So by minimising S_{Δ_j} it also results in the minimisation of the number of displacements calculated using extrapolation.

- **Integral CVT**

  Sadeghi et al [62] used a different method to linearise the CVT equations using an integral approach, which is presented as a more efficient approach.

Observations

CVT is fully 3D and accounts for the out-of-plane component. It is easy to implement and has low memory and CPU requirements. However smoothness is not guaranteed because the structural triangles used are only C^0 continuous. CVT is sensitive to the resolution of the structural grid (the structural grid is required to have a similar resolution to the aerodynamic grid [62]). It is also highly dependent on the quality of the mapping routine used.

3.4 Rigid Section Method

A different approach is taken for beam models. Since one of the assumptions is that the chordwise section is rigid perpendicular to the beam, a direction is defined along which the wing section is assumed to be rigid. These directions would be defined by the ribs in the wing structure. The beam is defined by the points $\mathbf{x}_i$ and along with the rigid direction, the corresponding leading $\mathbf{x}_{LE_i}$ and trailing $\mathbf{x}_{TE_i}$ edge points can be calculated. Then, the motion of this section is defined by the translation $\mathbf{dx}_i$ and rotation $d\alpha_i$ of the beam point. The displacement of any point $\mathbf{y}$ on the section can then be derived as

$$\mathbf{dy} = \mathbf{dx}_i + R\left(\mathbf{y} - \mathbf{x}_i\right) \tag{3.31}$$

where the rotation matrix R is given by

$$R = \begin{pmatrix} a^2K + \cos d\alpha_i & abK - c\sin d\alpha_i & acK + b\sin d\alpha_i \\ abK + c\sin d\alpha_i & b^2K + \cos d\alpha_i & bcK - a\sin d\alpha_i \\ acK - b\sin d\alpha_i & bcK + a\sin d\alpha_i & c^2K + \cos d\alpha_i \end{pmatrix}$$

where $K = 1 - \cos d\alpha_i$, the axis of rotation is $\mathbf{v} = ai + bj + ck$ and $|\mathbf{v}| = 1$. The fluid grid is defined at $\mathbf{y}_j$, and the transformation problem is to define the displacements $\mathbf{dy}_j$ based on the definition of the displacements and rotation on the structural grid. To do this each fluid point is projected on the beam elements parallel to the rigid direction, the displacements and rotation are then interpolated and Equation 3.31 is applied to the fluid point.

Chapter 4

Evaluation of Transformation Methods

4.1 Introduction

There are some questions of interest that this chapter aims to answer. First, what influence does C^0 continuity (CVT and IIM) have on the section shapes? Secondly what is the contribution of the out-of-plane component on the section shapes? Finally, what is the influence of any shape distortion on the flutter predictions? Two test cases are used to shed light on these questions and are described below.

4.2 Test Cases

4.2.1 Goland Wing

The Goland wing, shown Figure 4.1, is a rectangular wing that has a chord of 6 feet and a span of 20 feet. The aerofoil section is a 4% thick parabolic section. The CFD grid used was a coarse version with 35 thousand points and is block-structured using an O-O topology. This allows points to be focused in the tip region, which is the most critical region for the aerodynamic contribution to the aeroelastic response. This was solved using the Euler equations. The Euler equations can be used because the Goland wing is a slender wing and therefore has a thin boundary layer and along with a high Reynolds number the viscous effects can be safely neglected. Throughout the flow regime being investigated the flow is expected to be attached also allowing the use of the Euler equations. At the time of the calculations the Schur solver was only capable of using the Euler equations to calculate the flutter boundaries, which was still a significant improvement over linear methods due to the ability to capture shockwaves. For LCO the paper by Beran *et al.* [84] found that the effect of viscosity has a minimal effect on the onset of LCO, but did limit the amplitude of oscillation due to shock-boundary-layer interaction. This supports the use of the Euler equations for flutter boundary calculations of the Goland wing.

In this study three structural models were used. The original structural model is a wing-box that follows the description in reference [84] and includes a lumped mass tip store. A plate model is calculated from the wing-box by averaging upper and lower surface values onto a mid-plane using RBE3 elements. This model is referred to as the original plate.

The second model is an extension of the first. Points are added along the leading and trailing edges and also at the tip. These points are tied to the first plate model using RBAR elements. The element properties of the plate model have no rotational degrees of freedom, which are required by the RBAR elements for extrapolating the mode shapes. In order to recreate the mode shapes, the points on the leading and trailing edges as well as the tip have their displacements extrapolated linearly using a Matlab script after being extracted from the NASTRAN output. Due to the positioning of the structural model inside the wing, the only areas of extrapolation are at the trailing edge and a small area at the tip. This model is referred to as the extended plate.

The final model was derived from the first model and is a beam stick model. The mid-plane points for the centre spar were chosen to be the beam nodes. The rotations at the beam nodes were calculated from the first and third spars using a Matlab script. The displacements of the leading and trailing edges were calculated in Matlab using Equation 3.31 and a simple rotation matrix about the z-axis. This model is referred to as the beam stick model (BSM).

In addition to the three structural models refined versions of the original and extended plates were generated. Each element was split into four elements and the displacements were linearly interpolated using a Matlab script. All the structural models generated are shown in Figure 4.2.

The sections used in the shape comparisons are at 98% of the span and the position as well as the original section at this position is shown in Figure 4.1. This section is translated and rotated to the original orientation to allow for easier evaluation of the shape change introduced by the transformation methods.

4.2.2 MDO Wing

The second test case is the multi-disciplinary optimisation (MDO) wing [85], shown in Figure 4.3, this is a commercial transport wing with a span of 36m. The wing was optimised to fly at a certain altitude and Mach number and has a thick supercritical section. The CFD grid used was a coarse grid with 81 thousand points and was solved using the Euler equations. The use of the Euler

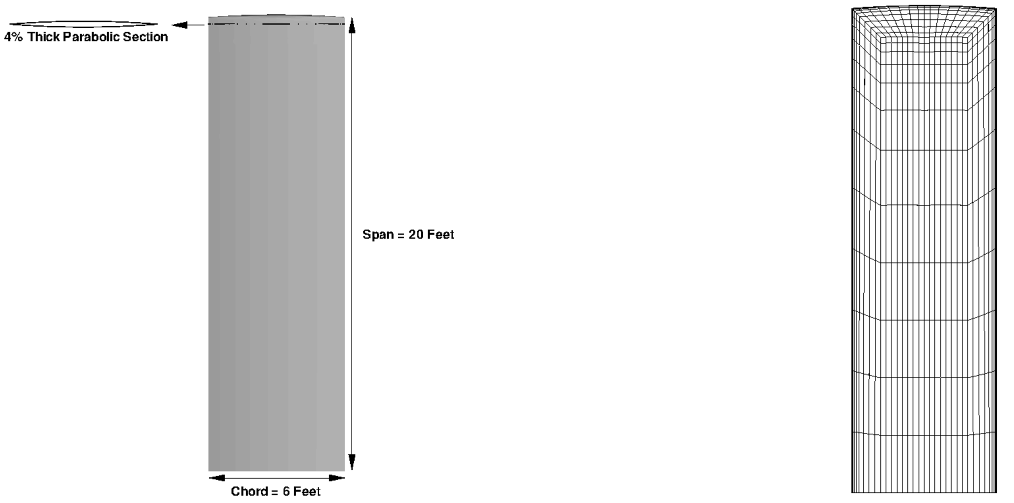

(a) Geometry (b) CFD surface grid

Figure 4.1: Goland wing geometry and CFD grid

equations is harder to justify than for the Goland wing, because of the thick aerofoil section. However the Reynolds number is high, which implies that the viscous effects are low. The paper on the MDO [85], shows that the shock position is different when including viscosity, but there is a significant degree of spread in the results between solvers. The Schur solver was only capable of calculating the flutter boundary using the Euler equations, but one should be mindful that when calculated with viscous effect that the flutter boundaries may change slightly. For this work the in-plane mode is neglected.

In this study two structural models were constructed. The original structural model is a wing-box model and this was converted into two beam stick models. The MDO wingbox model has a set of points that resemble a beam that acts as the connection points for the lumped masses. The points are attached to the wing-box ribs though RBE3 elements, with one point with a mass for each rib. These points were chosen to be the beam nodes in the new beam model. The displacements and rotations were extracted directly from NASTRAN at these nodes.

This serves as the basis for the two models used. For the first model the points on the leading and trailing edges are chosen so that the rigid ribs are approximately perpendicular to the beam, matching the ribs on the wing-box model. The second model has the points on the leading and trailing edges so that the rigid ribs are parallel to the x-axis (i.e. fuselage). These models are referred to as the perpendicular and parallel rib models respectively, and are shown in Figure 4.4.

The section used in the shape comparisons is taken at 98% of the span per-

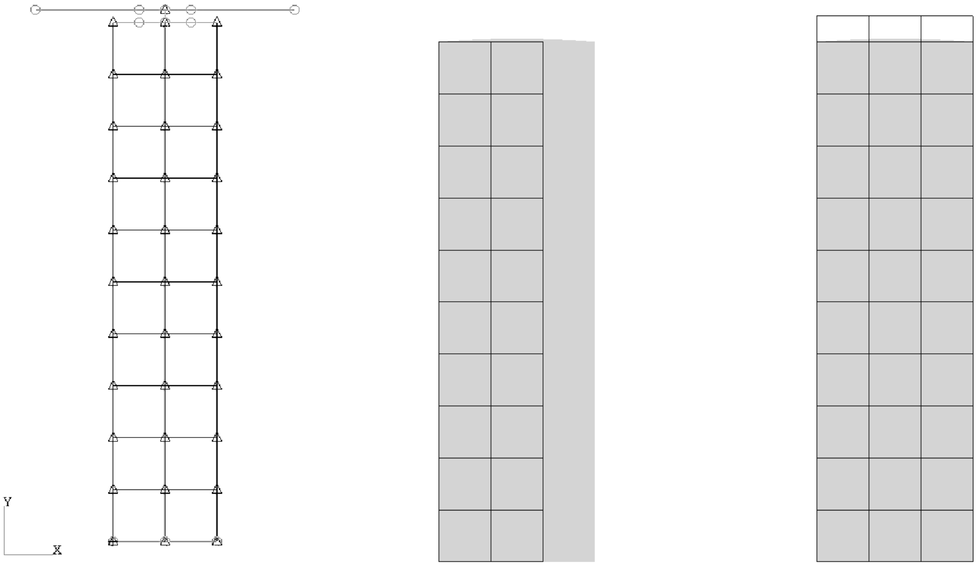

(a) Original NASTRAN model (b) Original plate (c) Extended plate

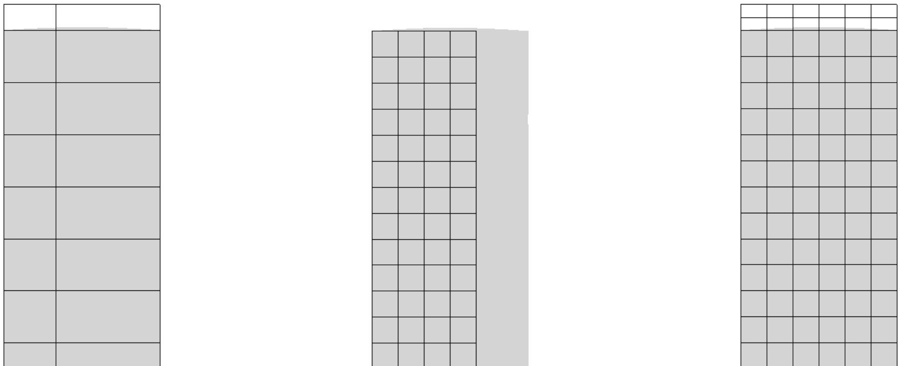

(d) Beam stick model (e) Refined original plate (f) Refined extended plate

Figure 4.2: Goland wing structural models (wing planform in grey)

pendicular to the beam and the position as well as the original section is shown in Figure 4.3.

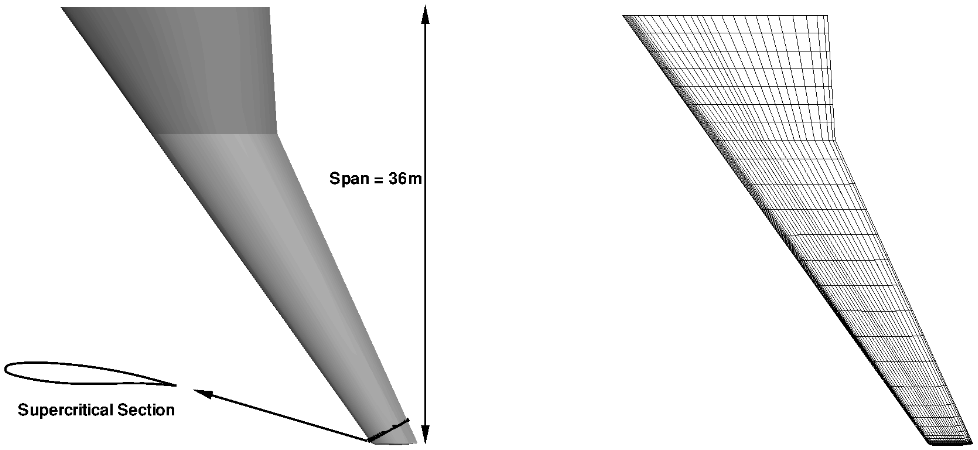

(a) Geometry (b) CFD surface grid

Figure 4.3: MDO wing geometry and CFD grid

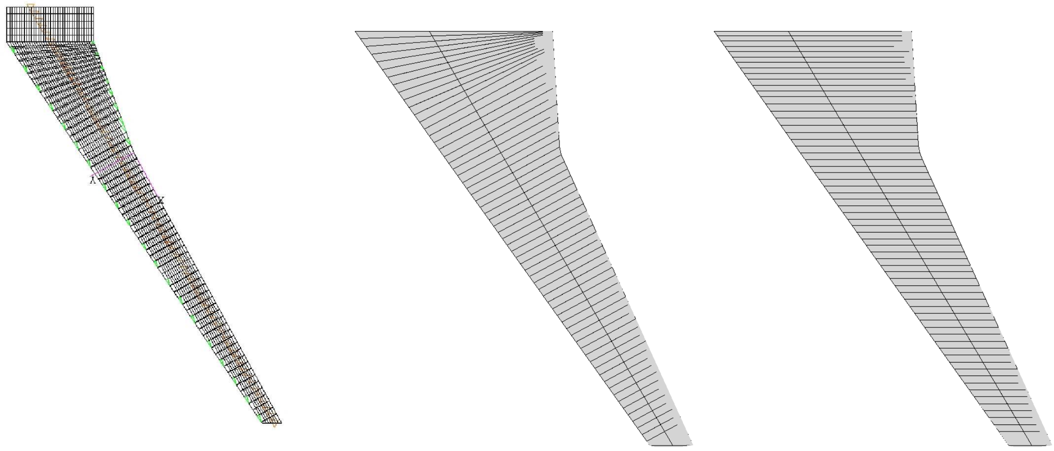

(a) Original NASTRAN model (b) Perpendicular ribs (c) Parallel ribs

Figure 4.4: MDO wing structural models

4.3 Evaluation of Transfer - Shape

The transfer methods were implemented and are tested in this section in terms of the mapped mode shapes. To test the transformation methods shape comparisons are shown for several cases in increasing complexity. The test section in each case is translated and rotated back to the original orientation to allow evaluation of the shape distortion introduced by the transformation.

4.3.1 Case 1 - In-plane

For this case the fluid grid is defined on a plane which is on the same surface as the structural grid and with the same planform as the Goland wing. The fluid grid is chosen to be finer than the structural grid and this case tests the in-plane treatment of the transformation methods only. Both the original plate and extended plate are compared in this case. Figure 4.5 shows the slice at 98% of the span for the third mode shape, which is the second torsion mode.

The CVT section exhibits a saw-tooth shape for both structural models, but passes through all of the NASTRAN points. This can be attributed to the lack of derivative continuity between structural elements. For the original plate, once the trailing edge of the structure has been reached, CVT extrapolates linearly. The IIM section passes through all of the NASTRAN points and provides linear extrapolation parallel to the element edges. The fact that IIM is only C^0 continuous does not show in the sections. IPS has trouble in the region of extrapolation for the original plate model where it flicks up to an unrealistically large deflection. Also throughout both structural models IPS oscillates between the structural model points. There is a well known problem with IPS[10, 60, 62] that it cannot recreate rigid rotations. IPS performs much better when there is no extrapolation, but still has minor oscillations. The RBF support radius was chosen to be 1.0 in order for the first mode shape to pass through the NASTRAN points, and no norm-biasing was applied. The RBF result shows the same problem with extrapolation as IPS, however it is much more severe. The observed additional camber has been seen in other papers [76] (incorrectly attributed to fuselage interference) and Rendall *et al.* [2] (where it was reduced by using norm-biasing).

This case highlights the differences between the local (CVT and IIM) and global (IPS and RBF) methods. The local methods exhibit a problem with slope discontinuity that the global methods do not suffer from, although IIM did not suffer from this visibly. IIM uses bilinear elements, so although they are only C^0 continuous this higher order interpolation appears to avoid the slope discontinuities experienced by CVT. The global methods however fail to extrapolate realistically and have oscillations that are reduced when there are no extrapolation regions. All the transformation methods performed better on the extended plate than the original plate due to the lack of extrapolation.

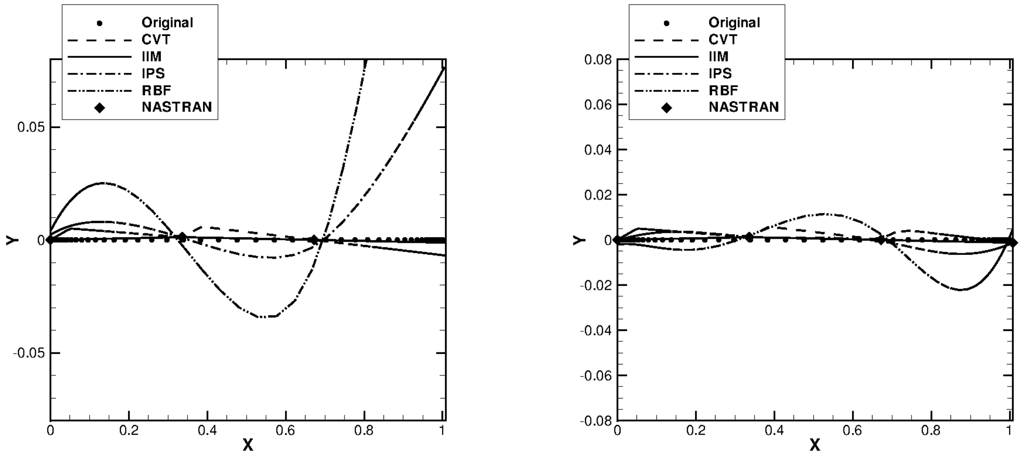

(a) Original plate

(b) Extended plate

Figure 4.5: Case 1: Section at 98% span for the third mode shape, rigidly translated and rotated back to the original orientation.

4.3.2 Case 2 - Goland Wing In-plane

For this case the fluid grid is now defined on the correct wing profile, but the fluid points are projected onto the structural plane. The transformation methods are used to define the displacements at the projected points and then these displacements are applied without modification to the wing points. This tests the discrepancy introduced by failing to calculate the out-of-plane component. Again only the original and extended plate models are used.

Figure 4.6 shows a slice through the two plate models at 98% of the span for the third mode shape. All of the methods show the same behaviour as seen for case 1, but now on the wing section. CVT shows the C^0 continuity effect which leaves the aerofoil nonsmooth. Interestingly IIM shows no sign of this problem and produces an excellent section shape. RBF and IPS both display the same behaviour as case 1 with the trailing edge failing to be extrapolated correctly, as well as section oscillations.

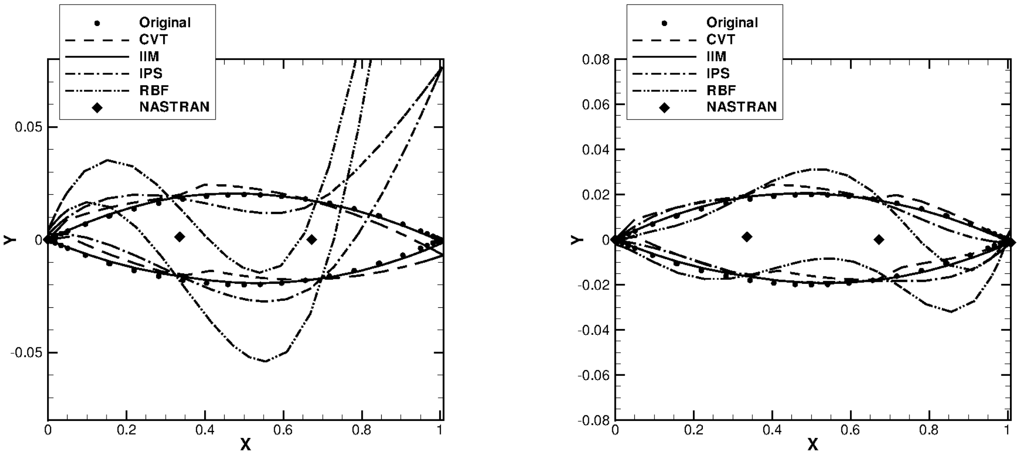

(a) Original plate (b) Extended plate

Figure 4.6: Case 2: Section at 98% span for the third mode shape, rigidly translated and rotated back to the original orientation.

4.3.3 Case 3 - Goland Wing Out-of-plane

Next, the CVT out-of-plane component is added to the in-plane components calculated from each method. Figure 4.7 shows the transformed slice. There is no significant change to the mode shapes between cases 2 and 3. It does seem to have the effect of thickening the section slightly. This is confirmed when the IIM result for case 2 is cross plotted with the IIM result for case 3, shown in Figure 4.8. Since the out-of-plane components come from CVT there is a slight discontinuity introduced in the slope. It can be seen that the effect of the out-of-plane component is small.

To complete the picture of the performance of the transformation methods on a plate a refinement of the structural grid was undertaken, and is shown in Figure 4.9 for the extended plate model. For all cases except IIM a significant improvement can be observed. For IIM there was no improvement shown, which implies that the IIM solution is already grid independent. For CVT the slope discontinuity problem persists, but the severity is less for both of the refined models. IPS is improved in the regions of grid refinement, it is expected that another level of grid refinement would converge the solution. RBF also benefits in the region of refinement and the extrapolation is also effected by the refinement. However although the improvement is significant for the RBF the sections are still the worst of the methods used.

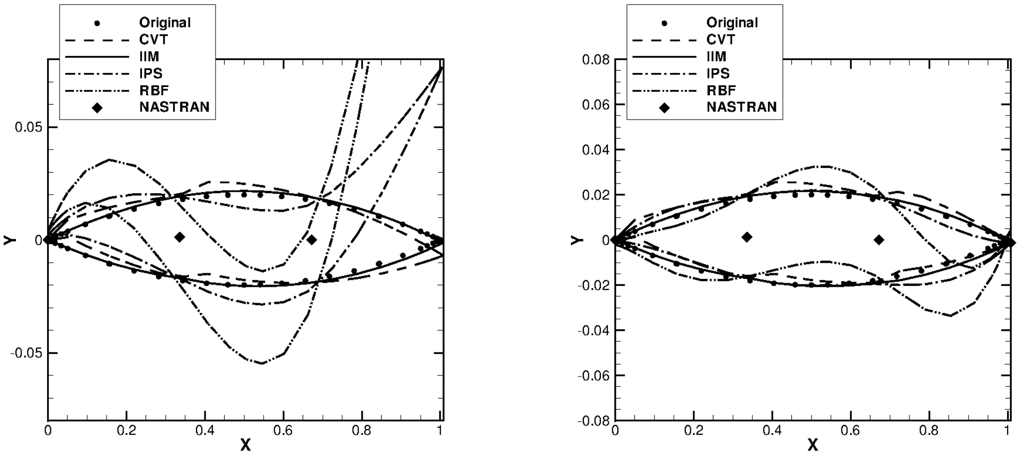

(a) Original plate

(b) Extended plate

Figure 4.7: Case 3: Section at 98% span for the third mode shape, rigidly translated and rotated back to the original orientation.

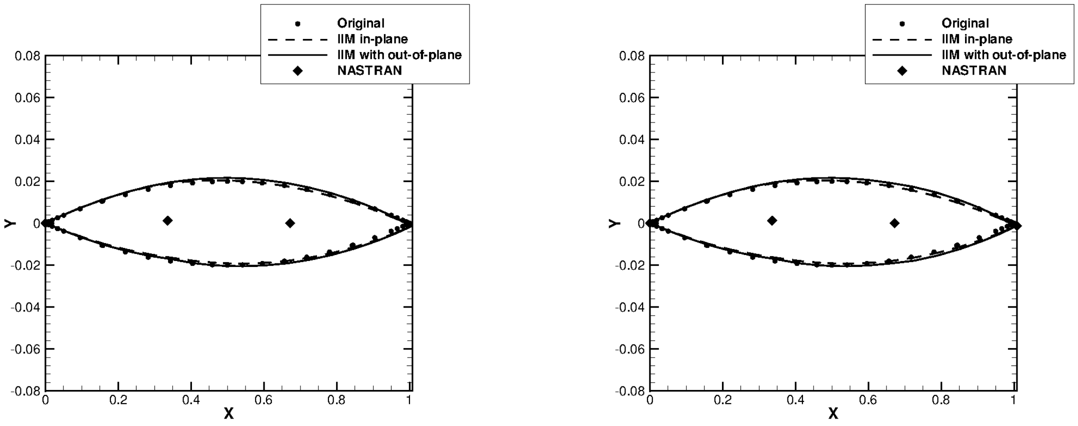

(a) Original plate (b) Extended plate

Figure 4.8: Case 3: Sections at 98% of the span through the mode 3 mode shape for IIM comparison for cases 2 and 3, rigidly translated and rotated back to the original orientation.

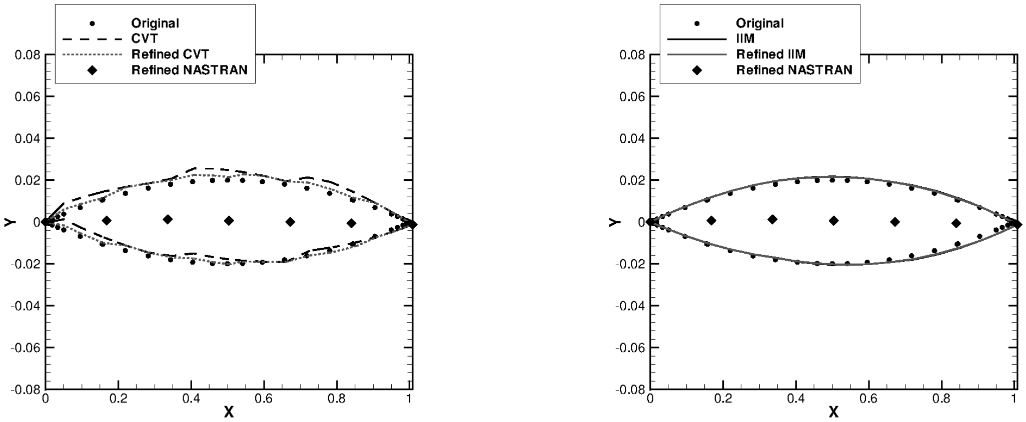

(a) CVT (b) IIM

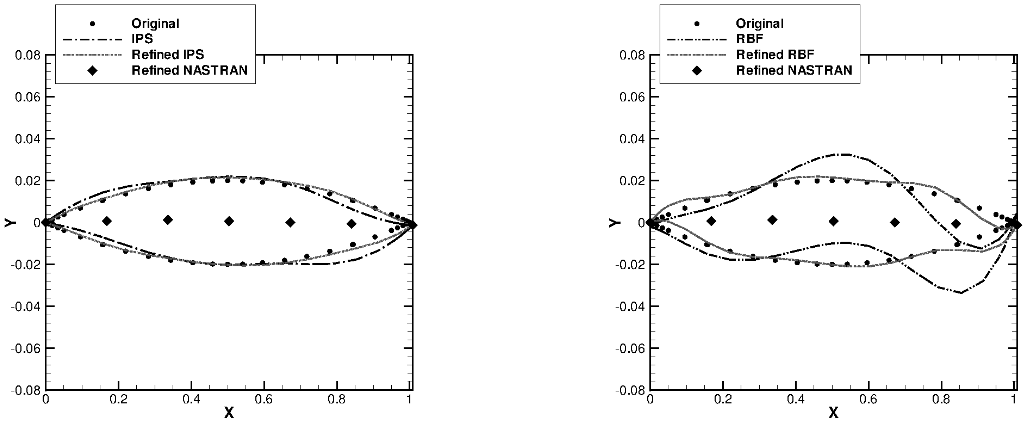

(c) IPS (d) RBF

Figure 4.9: Case 3: Sections at 98% of the span for the refined extended plate model, rigidly translated and rotated back to the original orientation.

4.3.4 Case 4 - Goland Wing Beam Stick Model

Finally the beam stick model is used and all transfer methods have the out-of-plane contributions from the CVT method applied to them. Figure 4.10 shows a slice at 98% for the third mode shape. All the methods are effectively using a coarsened extended plate model, since the BSM has one less row of structural points in the chord-wise direction that corresponds to the trailing edge of the wing box in the other structural models. The sections are significantly worse as the trailing edge is approached for all methods except IIM. CVT has a higher amplitude saw-tooth in the trailing edge region, but the saw-tooth in the leading-edge region is unchanged from case 3. This underlines the local character of this method. IIM appears to only be affected by the poor CVT out-of-plane contributions. IPS has the largest deviation from the section shape in the coarse region of the grid at the trailing edge, but also see an increase in the amplitude over case 3 in the leading edge region. RBF has the same trend as IPS, but to a worse degree.

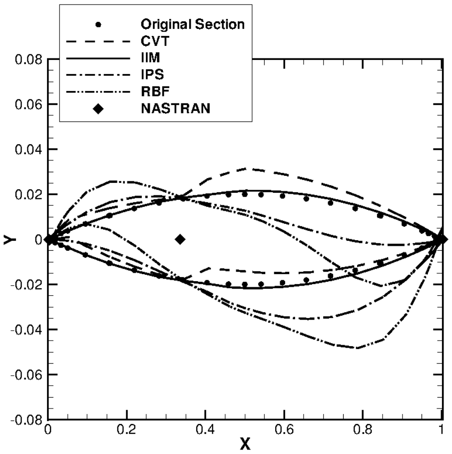

Figure 4.10: Case 4: Sections at 98% span through the mode 3 mode shape rotated and translated back to the original orientation.

4.3.5 Case 5 - MDO Wing

Next, results are shown for the two structural models of the MDO wing. The transformation methods are compared in terms of the vertical displacement calculated in Figure 4.11. The rigid rib results are considered exact in this comparison since all methods only have access to the beam structural model, and the rigid rib method exploits this information exactly by design. The displacements obtained by the different methods for the perpendicular ribs are similar except for those from IPS, which suffers due to the coarse structural grid used. RBF is not shown because the deflections are very different compared to the other methods. There is much more variety in the results for the parallel ribs, in this case IIM and the rigid ribs approach match well. CVT has a slight saw-tooth pattern and IPS deviates slightly due to the coarse mesh. RBF prediction is rather poor for the MDO wing. The reason that the discrepancies are small compared to the Goland wing is due to the scaling. A significant difference is seen between the displacements obtained from the different rib orientations, with larger displacements seen for this mode from the parallel ribs shown in Figure 4.11(c). For other modes this is the opposite way around. The reason for this difference is that the values for the rotation of the section are obtained from different points on the structural beam.

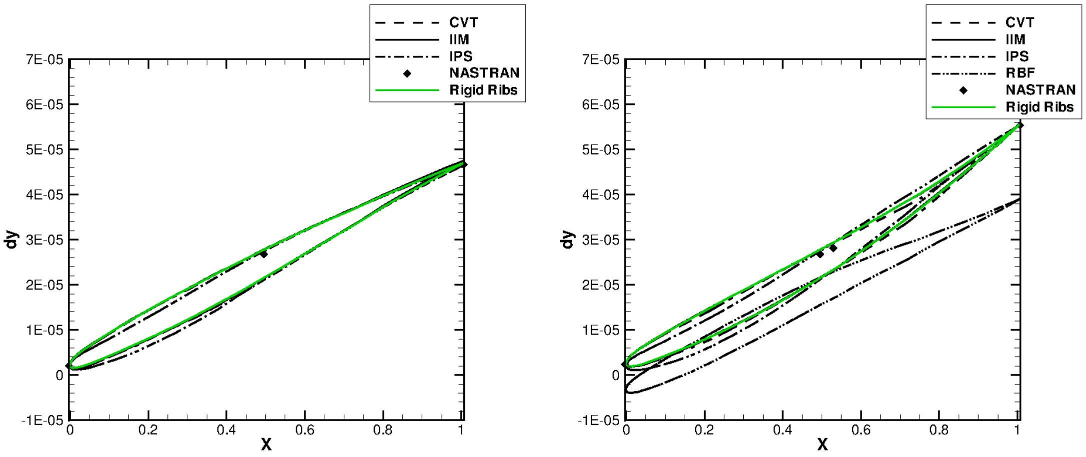

(a) Perpendicular rib model

(b) Parallel rib model

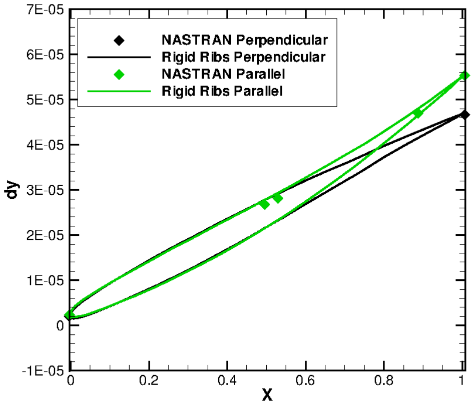

(c) Rigid rib comparison of parallel and perpendicular ribs

Figure 4.11: Case 5: Vertical displacement of sections at 98% span for the mode 5 mode shape.

4.3.6 Summary

From these test cases it has been shown that allowing the transfer methods to extrapolate is inadvisable. The in-plane component dominates the final displacements calculated, other factors have a larger effect on the final displacement than accounting for the out-of-plane affects. Of the methods tested only IIM was unaffected by changing grid density. All the other methods benefited from the structural grid being refined. The local method CVT suffered from a saw-tooth pattern of discontinuities in the slope, which could be reduced by refining the structural grid. The other local method IIM did not suffer from this discontinuity in slope, probably due to the higher order interpolation inside the bilinear elements used. The RBF result could be improved using the techniques and advanced algorithms covered in the previous chapter. Also Ahrem *et al.* [77] published a paper on using RBF with BSM, however the proposed algorithm was found to be six times more expensive than the standard algorithm. The proposed rigid ribs method was shown to perform well producing smooth section shapes similar to IIM. As expected the orientation of the ribs has an effect on the section shapes, which as the orientation becomes further from the ideal perpendicular section the section shapes get worse.

4.4 Flutter Evaluation

Having evaluated the influence of the transformation methods on the sectional shape, the impact of these distortions is now evaluated for the aeroelastic stability predictions. The Schur eigenvalue method is used to trace the aeroelastic eigenvalues as a function of altitude (see the Schur solver in Section 2.8).

4.4.1 Goland Wing

The Goland wing mode tracking at a Mach number of 0.80 and zero degrees incidence for all modes using CVT and the original plate model is shown in Figure 4.12. It can be seen that modes one and two interact, with mode one becoming undamped at 13,216 feet as the real part of the eigenvalue becomes positive. The evaluation of the influence of the transformation methods is presented below for the real part of mode one.

The effect of using different structural models is shown for the Goland wing in Figure 4.13 and Table 4.1. Consistent with the section shape results presented above, IIM shows the least spread of results as the structural model is changed. CVT and IPS show comparable spread in their results, particularly where the interaction is strong as the mode becomes undamped. RBF shows a large spread and has no real correlation between the different structural model results. The original plate model did not flutter for mode one, when all the other transfer methods and structural model combinations did. The extended and BSM models did flutter in mode one, but their flutter points are almost 9,000 feet different. Next the results from different methods are compared for each structural model in turn and this is shown in Figure 4.14. The predictions from the local IIM and CVT methods are similar for all the structural models. There is considerable spread in the results for the global methods (IPS and RBF). For the extended plate where the section shapes were the most reasonable, all the flutter points are clustered including RBF. The original plate shows the CVT and IIM methods closely clustered with the IPS flutter point close, RBF however did not flutter for this mode. The BSM model is effectively a coarsened extended plate and since the global methods suffered the most in the section shapes their results are spread out compared to the local methods. If the IIM flutter results are assumed to be correct due to the excellent performance in the section shapes, then the other methods results can be compared with them. It would appear that the discontinuity in slope has a smaller effect on the flutter results than induced oscillations in the mode shapes.

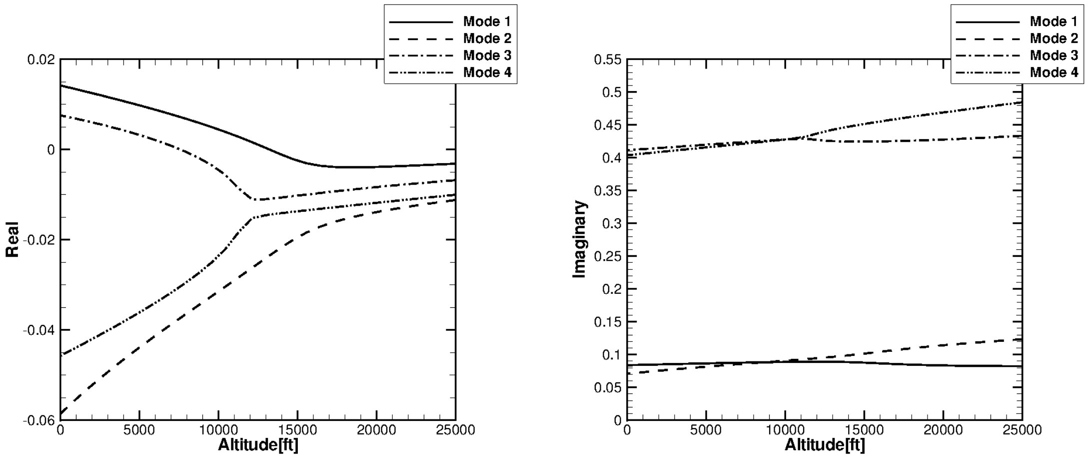

(a) Real part

(b) Imaginary part

Figure 4.12: Goland wing mode tracking for all modes using CVT

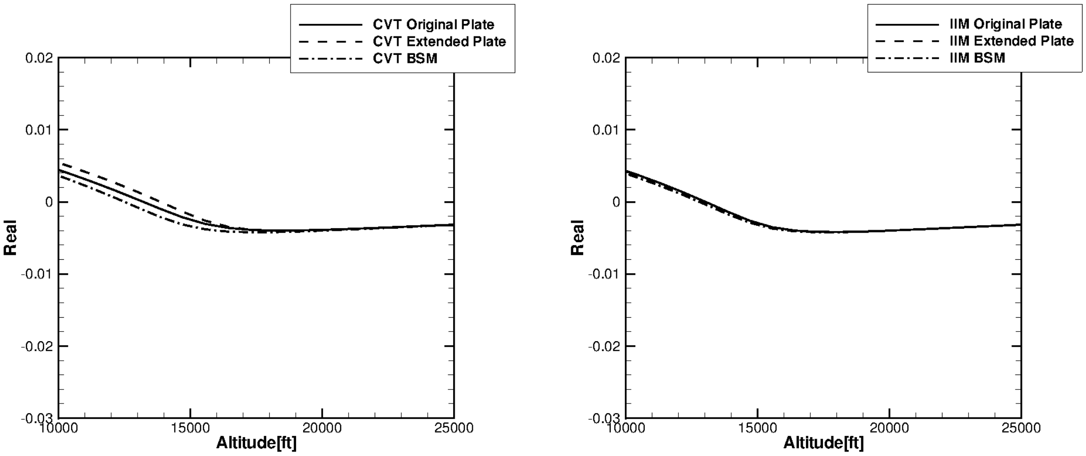

(a) CVT (b) IIM

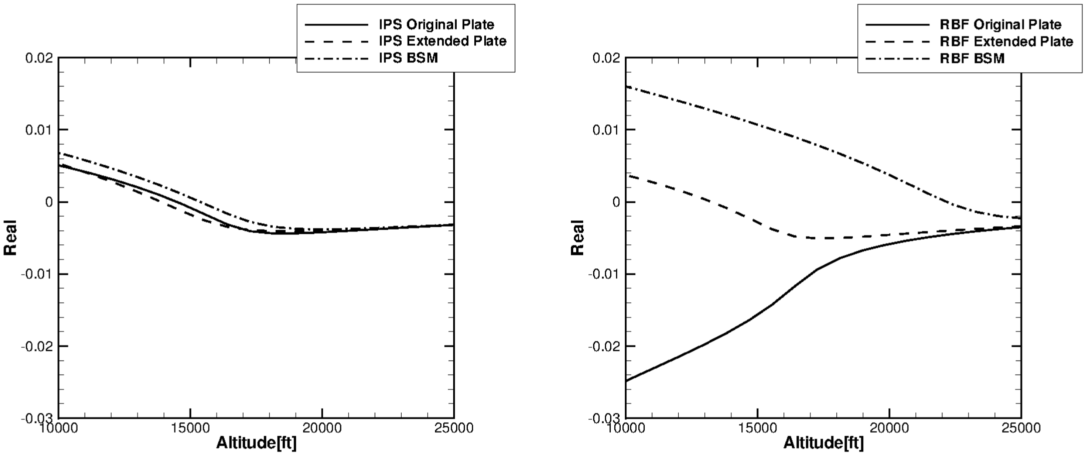

(c) IPS (d) RBF

Figure 4.13: Goland wing mode tracking for mode 1 for the different structural models (real part)

Table 4.1: Flutter altitude for Goland wing (all values in feet)

	Original plate	Extended plate	BSM	Spread
CVT	13216	13865	12502	1363
IIM	13025	13002	12790	235
IPS	14480	13890	15373	1483
RBF	N/A	13243	22175	8932
Spread	1455	888	9673	

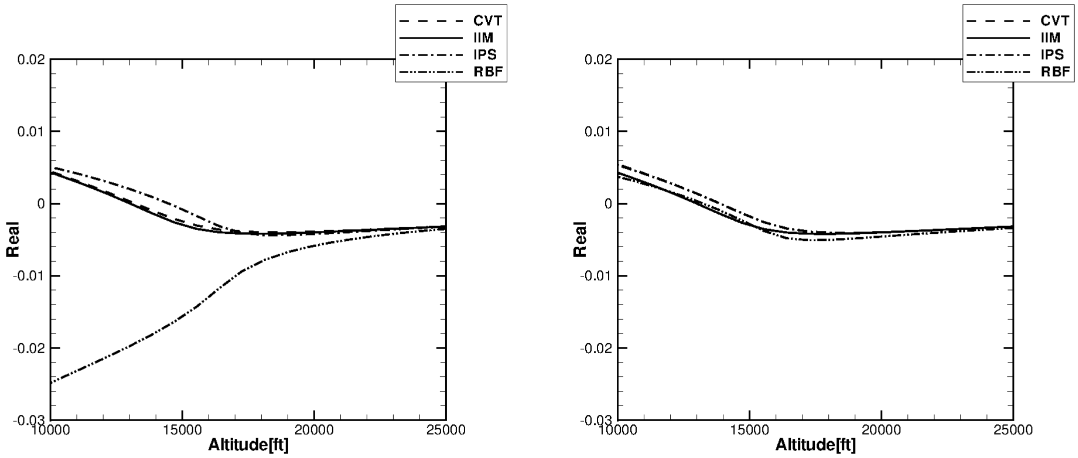

(a) Original Plate (b) Extended Plate

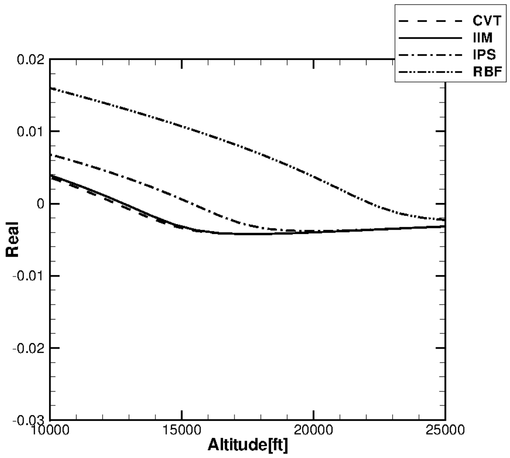

(c) BSM

Figure 4.14: Goland wing mode tracking for mode 1 for the different structural models (real part)

4.4.2 MDO Wing

The mode tracking for the MDO wing at a Mach number of 0.85 and an incidence of one degree based on the beam model with perpendicular ribs using CVT, is shown in Figure 4.15. Modes one, two and four participate in the instability, with mode one going undamped first at -2358m.

The effect of the rib orientation for the MDO wing is shown in Figure 4.16. It can be seen that there are significant differences in damping between the two rib orientations, even if the crossing at a similar altitude. The comparison of the predictions from the different transformation methods is shown in Figure 4.17 and Table 4.2. The perpendicular ribs has a tight clustering of the flutter points for all the methods except RBF which fails to flutter for this mode. This is not a suprise since it's section shape was so different to the other methods it was omitted. The parallel ribs shows more variation between the methods with the local methods clustered tightly. The rigid ribs predicts flutter at a slightly higher altitude compared to the local methods, but the global methods predict the flutter point at even higher altitudes. It is not obvious from the sections why the rigid ribs and IIM are not more similar in this case, although it could be due to the other modes that interacts with mode one having a different section shapes leading to a different flutter points.

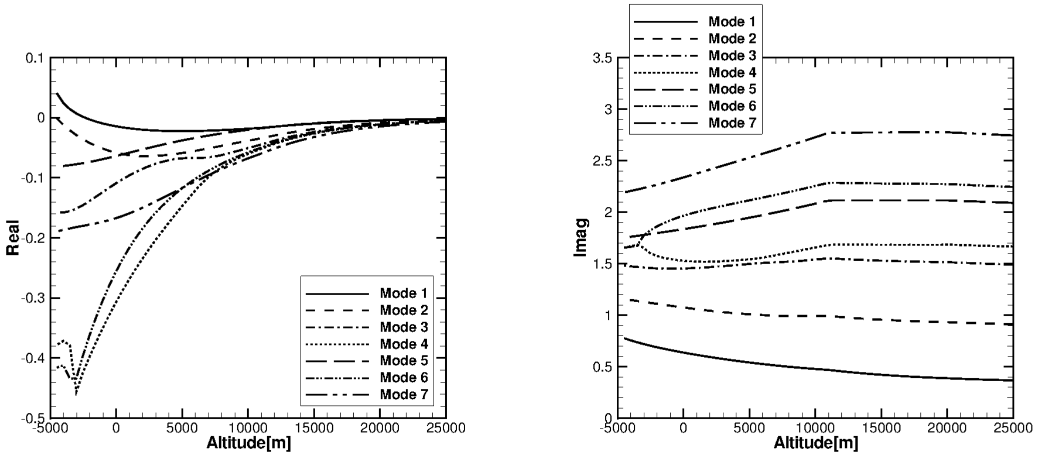

(a) Real part

(b) Imaginary part

Figure 4.15: MDO wing mode tracking for all modes using CVT

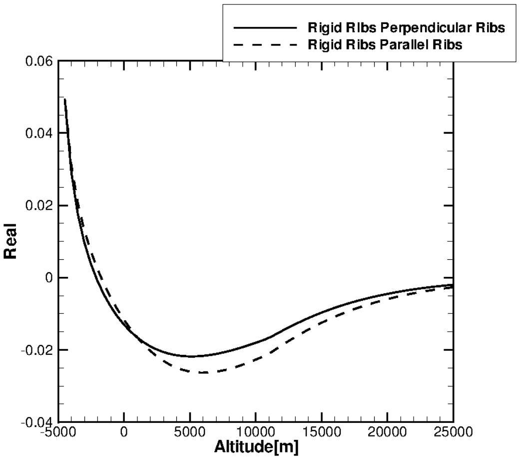

Figure 4.16: MDO wing mode tracking for mode 1 for the different structural models (real part)

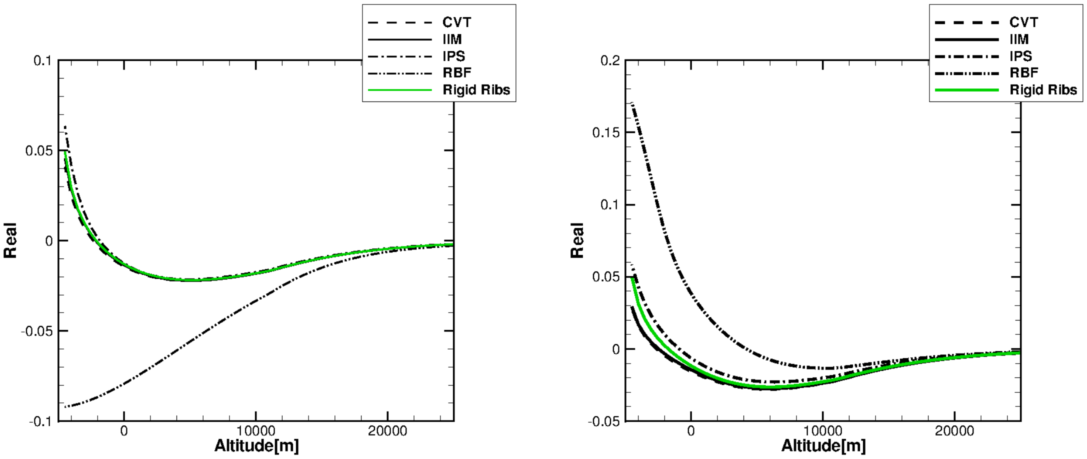

(a) Rigid ribs perpendicular to the beam

(b) Rigid ribs parallel to the x-axis

Figure 4.17: MDO wing mode tracking for mode 1 for the different structural models (real part)

Table 4.2: Flutter altitude for MDO wing (all values in meters)

	Perpendicular	Parallel
CVT	-2358	-2612
IIM	-2175	-2481
IPS	-1848	-915
RBF	N/A	4198
Rigid ribs	-2125	-1743
Spread	510	6810

4.5 Summary

The performance of transformation methods was evaluated. Several common methods were compared for two test cases in terms of their influence on the aeroelastic damping. It is one thing to have a predictive method for calculating flutter, however confidence needs to be built up in its ability and robustness. Through using different transformation methods it has been shown that when there is no extrapolation there is minimal spread in the resulting flutter point. When the methods are required to extrapolate there is a large degree of spread in the flutter point. This clearly shows that to minimise the error associated with using the transformation methods no extrapolation should be used.

It was also shown that the orientation of the ribs is important in BSM because most transfer methods do not use rotation data and therefore require additional displacements to be provided (usually at the leading and trailing edges). Although it is much simpler and quicker to use the parallel ribs approach, it is more reliable to use the perpendicular ribs approach that also matches with the assumptions of BSM. By using the perpendicular ribs the scatter in the results was also reduced.

Whilst it is unlikely to be the norm to have multiple structural models of different types to test on, it should be possible to have multiple transfer methods available. Since it has been shown that the choice of transfer method can have a significant affect on the predicted flutter point then it is strongly advisable to use more than one transformation method during the verification process.

Chapter 5

Aerofoil Buffet

5.1 Introduction

Transonic buffet is associated with shock/boundary-layer interaction, although buffet is a more general term used for any flow unsteadiness inducing structural vibrations. Consequences of this phenomena can range from reduced fatigue life to structural damage [4]. Transonic buffeting is interesting because it has more severe buffet loads than the low-subsonic or supersonic conditions. Transonic buffet occurs when a shock is strong enough to induce boundary-layer separation at its foot. Under certain conditions a large amplitude periodic shock motion can occur. The prediction of this behaviour is challenging for CFD. The success of the prediction depends on the turbulence model used. This chapter reviews previous work on the prediction of flow over the Bauer-Garabedian-Korn (BGK) No. 1 aerofoil. Then the unsteady flow over the BGK No. 1 aerofoil is predicted.

5.2 Test Case

Previous investigations at the National Aeronautical Establishment (NAE) in Canada have shown that supercritical aerofoils have more favourable buffet characteristics compared to conventional aerofoils. In the 1980s and 1990s the Bauer-Garabedian-Korn (BGK) No. 1 supercritical aerofoil was investigated experimentally at NAE. The BGK was designed for a Mach number of 0.75 to have a lift coefficient of 0.63 with a thickness-to-chord ratio of 11.8%. From the results of these experiments a number of papers were published [86]-[89]. Later this aerofoil was selected as an AGARD test case and the experimental results were published in detail by Huang [90]. Finally CFD predictions were published by Xiao *et al.* [3, 91].

It was found that the buffet excitation frequency was 70-80Hz for Mach numbers 0.688 to 0.796. The buffet boundary for this aerofoil, along with the experimental data points is shown in Figure 5.1. The shock oscillation region was obtained by fixing the Mach number and varying the angle of attack. At each angle a power spectra for the normal force was computed and the presence of shock oscillation was deduced from whether a peak at 70-80Hz was present. The buffet boundary was calculated from a plot of rms values of the normal-force fluctuations, C'_N vs. C_L and was determined as the point that has a slope of $dC'_N/dC_L = 0.1$ [87]. This was an arbitrarily chosen value that matched the buffet boundary calculated by the trailing-edge pressure divergence criterion.

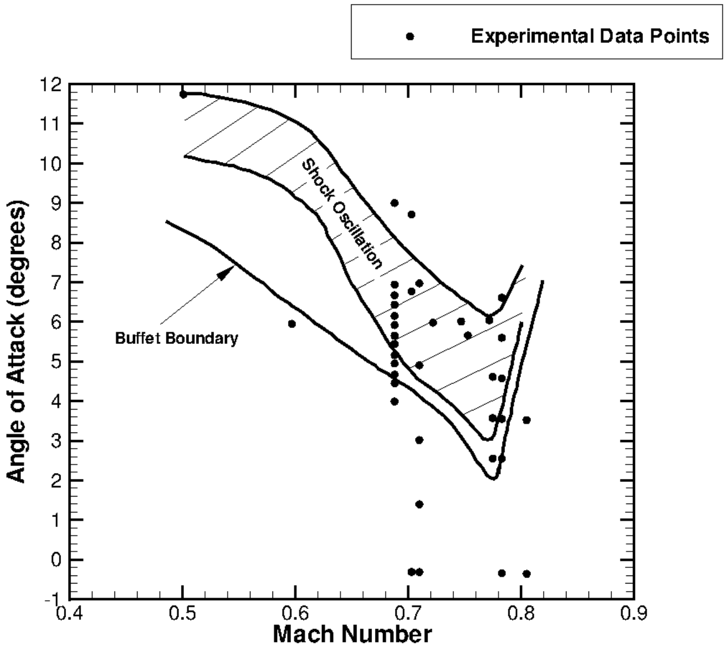

Figure 5.1: BGK No. 1 buffet boundary with the experiment locations (circles)

The experiments covered the Mach number range of 0.501 to 0.805, angle of attack range of -0.36° to 11.74° and Reynolds numbers between 15 million and 21 million. The wind tunnel had a floor and ceiling porosity of 19.3% or 20.5% depending on the reference. The aerofoil used in the experiments had a chord of 10in. and a span of 15in., and had 50 pressure orifices on the upper surface and 20 on the lower surface. It also had 16 miniature fast transducers on the upper surface for unsteady measurements. The locations of these pressure orifices and fast transducers are given in ref. [90] and are shown in Figure 5.2. For experiments at Mach number 0.688 skin friction was also measured. It was estimated that transition occurred at 10% of the chord. The results published focused on three test cases; case 1: Mach number 0.688 with varying angle of attack; case 2: Mach number 0.710 with varying angle of attack; case 3: angle of attack 6° with varying Mach number.

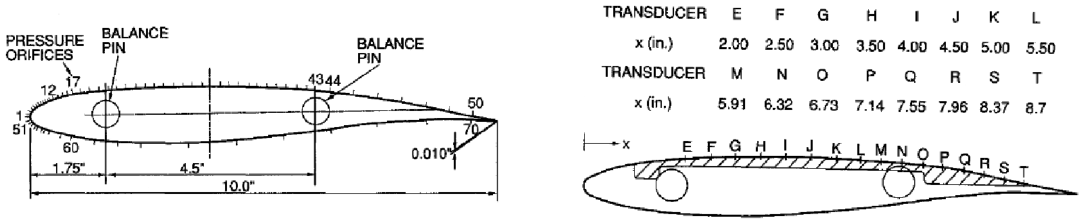

(a) Pressure orifice locations (from ref. [88]) (b) Fast transducer locations (from ref. [88])

Figure 5.2: BGK No. 1 supercritical aerofoil

Case 1 also had skin friction measurements taken. The shock boundary-layer interaction was classified into three types and the various angle of attack values were characterised. The first class of shock boundary-layer interaction is characterised by a weak shock that results in a low level shock excitation. The experiment at a Mach number of 0.668 and an angle of attack 3.99° was an example and showed a large peak in pressure fluctuations at the shock and the remainder of the aerofoil had very low levels. The second class is characterised by a strong shock that causes local separation and reattachment, for example in the experiment at Mach 0.668 and angle of attack 4.95°. The skin friction showed that there was a region of separation behind the shock followed by reattachment. The pressure fluctuations showed a large peak at the shock and second small peak in the separation bubble with the remainder of the aerofoil having very low levels. The third class is characterised by a strong shock followed by fully separated flow, but with some of the characteristics of the separation bubble and trailing-edge separation i.e. there is a peak in the pressure fluctuations that corresponds to the separation bubble even though this no longer exists. The experiment at Mach number of 0.688 and an angle of attack 6.94° showed this behaviour. The pressure fluctuations again showed a large peak at the shock and a second moderate peak for the separation bubble followed by a moderate level for the remainder of the aerofoil. When the angle of attack was increased to 9° the flow became very unsteady with very large shock motions. It was also found that as the angle of attack increased the trailing edge separation expanded faster than the separation bubble behind the shock. The switch from class two to class three shock boundary-layer interaction happened with a small increase in angle of attack. It was found that below angle of attack 4.67° that the flow was attached, at angle of attack 4.67° a separation bubble is detected. At angle of attack 6.13° trailing edge separation had reached x/c =0.89 and above angle of attack 6.94° the aerofoil became fully separated. The maximum fluctuation in normal force C_N' was found to be at an angle of attack 8°.

Case 2 was at Mach 0.710 with an angle of attack range of -0.316° to 6.97°.

The results were very similar to those of case 1. The flow at angle of attack -0.316° was sub-critical with fully attached flow and at angle of attack 1.396° there was a weak shock formed with no separation. For angle of attack 3.017° there was a stronger shock with small oscillations which had decayed by the next transducer 5% of the chord downstream. A separation bubble was formed behind the strong shock at angle of attack 4.905° and then at angle of attack 6.970° the flow has become fully separated.

For case 3 the experiments used an angle of attack of approximately 6° whilst varying the Mach number from 0.597 to 0.772. It was found that at M=0.597 the flow was attached due to the absence of pressure fluctuations. As the Mach number was increased to 0.688 the flow gained a stronger shock that leads to a separation bubble. Above Mach 0.722 the flow is fully separated from the shock to the trailing edge and there is no evidence of the separation bubble. The maximum C_N' was found to be at Mach 0.733. The frequency of oscillation was found to be a linear function of Mach number.

For the BGK No. 1 aerofoil experiments, boundary-layer suction was used and the ceiling and floor had 19.3% or 20.5% porosity depending on the reference. Also the span of the aerofoil was only 1.5 chords potentially effecting the accuracy of the CFD predictions due to the uncertainty caused by the wind tunnel walls. It is likely that the two-dimensional character of these experiments is not beyond question.

There has been a CFD study using the BGK No. 1 aerofoil by Xiao *et al.* [3]. This CFD study focused on case two, the flow conditions used are shown in Table 5.1. The grid used had a C-topology and was 640 × 64 with 512 points on the aerofoil and 128 in the wake. The initial wall spacing used was 1×10^{-6} of the chord. A grid refinement study was carried out and it was found that this grid was adequate for their study. The grid refinement study also found that the dominant frequency was insensitive to the grid refinement.

Table 5.1: Xiao *et al.* [3]: Flow conditions

Reynolds Number	20×10^6
Mach Number	0.710
Angles of Attack	1.396°, 6.970°, 9.000°
Non-dimensional Time Step	0.05
Non-dimensional Duration	150-200

The first case was at angle of attack 1.396°, where a weak shock is expected with no separation. The CFD predicted the shock too far downstream, however when the angle of attack was changed to account for wind tunnel corrections the shock was predicted closer to the experiment. The second case was at an angle of attack of 6.970°, the experimental result was a strong oscillating shock causing full separation. The mean lift coefficient from the CFD was 1.030 and the experimental mean lift coefficient was 1.016. For the dominant reduced frequency the CFD prediction was 36% lower than the experimental result. For this case no wind tunnel correction was used. The CFD failed to capture the magnitude of the unsteady pressure, however there was better agreement for the phase. The final case at angle of attack 9.000° showed a steady shock at the leading edge that caused separation to the trailing edge.

An attempt has been made to understand the mechanism behind self-sustained shock oscillations and shock-induced buffet [12, 92, 93]. This was also studied computationally by Xiao *et al.* [3]. The mechanism proposed by Lee [12] is shown in Figure 5.3. The mechanism is for self-sustained shock oscillations with fully separated flow after the shock wave. Due to the shock motion pressure waves are formed that propagate downstream in the separated flow region at velocity u_d. When these waves reach the trailing edge they generate new waves either from the wake fluctuation or from the trailing edge boundary layer, which travel upstream outside the region of separated flow at velocity u_u. These new waves interact with the shock and impart energy to it to maintain the oscillation. This loop then repeats, the period of the shock oscillation T_p should agree with the time it takes for the waves to propagate to the trailing edge and the time it takes the new wave to propagate upstream to the shock. This can be given by the following equation

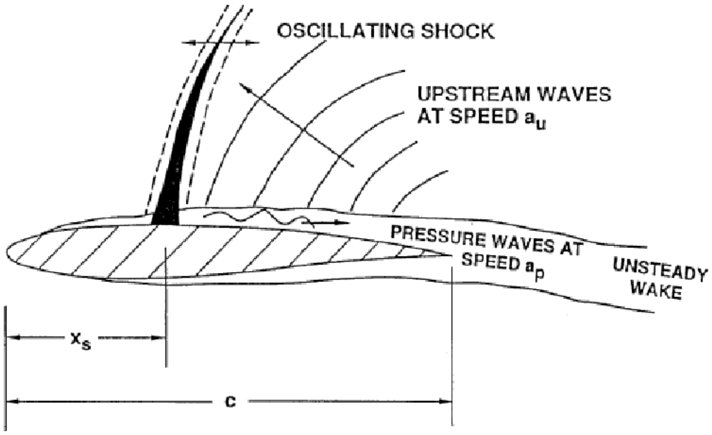

Figure 5.3: Model of self-sustained shock oscillation for the BGK No. 1 aerofoil (from ref. [12])

$$T_p = \int_{x_s}^{c} \frac{1}{u_d} dx - \int_{c}^{x_s} \frac{1}{u_u} dx \tag{5.1}$$

where u_d is the speed of downstream pressure wave propagation, u_u is the speed of upstream pressure wave propagation and x_s is the time-mean shock position. It has also been shown experimentally that during buffeting the wake oscillates and the periodic shock motion is coupled with the disturbances generated at the trailing edge. It was also shown experimentally that the unsteady pressures in the wake are random until a periodic shock oscillation occurs. Then the wake shows a distinct frequency peak which is the same as the shock frequency. Lee *et al.* [92] used the non-linear transonic small disturbance equation to investigate the propagation of the Kutta waves over a series of aerofoils with shock waves. The empirical formulation that had previously been used to compute u_d and u_u was shown to compare favourably with the numerical computations. Xiao *et al.* [3] used cross-covariance of signals in various locations in the CFD flowfield to show that a pressure wave was propagating downstream in the separated region and that there was a pressure wave propagating upstream outside this region. This agrees well with Lee's model. They also shows that by using the cross-covariance they could calculate u_d and u_u and by using Equation 5.1 calculate the time period of the shock oscillation. This can be converted into a reduced frequency of 0.175 which compared favourably with the Fast Fourier Transform (FFT) of the lift coefficient of 0.16.

5.2.1 Other Aerofoil Buffet Cases

In the 1970s experiments were undertaken on an 18% thick circular-arc aerofoil at NASA for computer code validation. It was tested in a wind tunnel with contoured upper and lower walls for a nominal Mach number of 0.775. It has been studied both experimentally and numerically [13]-[99].

The experiments covered the Mach number range of 0.71 to 0.78 and Reynolds numbers between 1 million to 17 million. The angle of attack was kept constant at zero degrees. The aerofoil used in the experiments had a chord of 20.3cm and a span of 25cm. McDevitt *et al.* [13] showed experimentally that the experimental setup and conditions were two-dimensional in nature.

This aerofoil has three distinct flow regimes, the first occurs when below the critical Mach number of 0.76 . It is characterised by a steady weak shock and trailing edge separation. The second flow regime occurs between Mach number 0.76 and 0.78. In this regime there is a strong shock on the upper and lower surfaces that oscillate out of phase along with shock induced boundary-layer separation. Finally the third flow regime is as the Mach number is increased beyond 0.78 and the shocks become stronger. The shock becomes steady and induces boundary-layer separation that extends to the trailing edge. When the Reynolds number is greater than 5 million the flow exhibits a flow hysteresis. The flow hysteresis is shown in Figure 5.4.

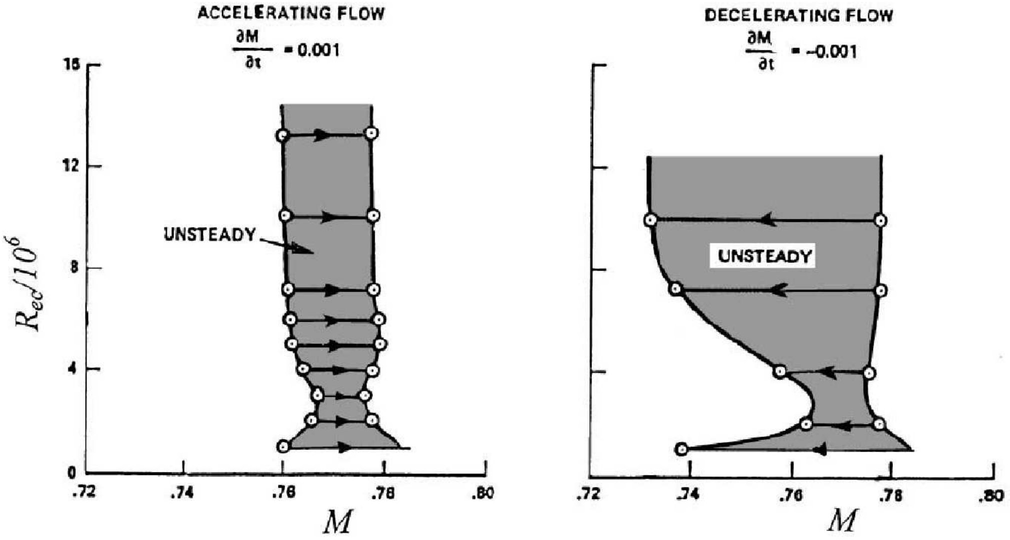

Figure 5.4: 18% thick circular-arc aerofoil shock oscillation domains (from ref. [13])

The mechanism for the flow over this aerofoil at zero degrees was described by McDevitt *et al.* [13]. It was explained as the shock induced boundary-layer separation on the upper surface causes a thickening of the boundary-layer on the upper surface. This effectively creates a negative camber which has the effect of slowing the flow on the upper surface. This tends to suppress the shock-induced phenomenon, but at the same time induce higher velocities over the lower surface, causing shock induced boundary-layer separation there and the flow field flips. This mechanism was verified by McDevitt [95] by using a splitter plate at the leading and trailing edges.

An alternate mechanism was proposed by Chen *et al.* [99] similar to that of Lee for the BGK No. 1 aerofoil. The model proposed by Lee assumed the shock oscillates above the aerofoil, the model proposed by Chen *et al.* assumes the shock propagates upstream and leaves the aerofoil. The flow mechanism is described as a series of compression waves develop in the region near the trailing edge and move upstream. As they move upstream they coalesce to form a strong shockwave, this shockwave continues to move upstream whilst strengthening and induces boundary-layer separation. Once it has reached the mid-chord the shock weakens to a weak shock and then compression waves that propagate upstream leaving the aerofoil.

At ONERA in France wind tunnel tests were done on the OAT15A aerofoil which is a supercritical profile. The experiments were done by Jacquin *et al.* [100] and CFD calculations have also been performed by Deck [101].

The experiments covered the Mach number range of 0.7 to 0.75, angle of attack range 2.5° to 3.91° at a Reynolds number of 3 million. The aerofoil is 12.3% thick with a trailing edge thickness of 0.5% and in the experiment the chord was 230mm with a span of 780mm. The experiment had 68 static pressure orifices and 36 unsteady Kulite pressure transducers. Transition was forced at 7% of the chord and buffet onset was found to be at 3.1° for Mach 0.73. When the angle of attack was increased to 3.5° the shock oscillations traversed 20% of the chord with a frequency of 70Hz. This frequency was insensitive to angle of attack, but was sensitive to Mach number.

The transonic buffet on the aerofoil is similar in character to the BGK No. 1 aerofoil. The boundary-layer remains attached as the shock moves downstream, when it reaches its most downstream location the shock causes the boundary-layer to separate. The region of separation increases in size until it reaches the trailing edge as the shock reaches the most upstream position. At this point the boundary-layer becomes attached and the loop repeats. The unsteady pressure transducers detected a pressure wave travelling downstream over the upper surface at $0.072U_\infty$ and a pressure wave travelling upstream at $0.27U_\infty$ over the lower surface. This results appears to be similar to the mechanism proposed by Lee [12] for the BGK No. 1 aerofoil.

Garnier and Deck [102] also studied the OAT15A aerofoil, but using a zonal URANS/LES solver with the flowfield calculated using LES except on the pressure side of the aerofoil, which uses 2D URANS. This study showed pressure waves travelling downstream over the upper surface and upstream over the lower surface. The mechanism of Lee [12] was evaluated and gave a higher frequency using Equation 5.1 in comparison to the power spectral density of the signals. This was contributed to the lower surface contributing to the mechanism, not just the upper surface pressure waves, however further research was needed.

Raghunathan *et al.* [103] presented results on the NACA 0012 aerofoil that was pitched from 5° to 6°. The flow at 5° was steady and the flow at 6° had shock-oscillations with boundary-layer interaction. The paper studied the mechanism of the onset of buffet and proposed a mechanism behind the origin of shock oscillation. The shock was strong enough to generate a separation bubble that caused the shock to move upstream, strengthening and increasing the length of the separation bubble. When the separation bubble reached the trailing edge, the upper surface became fully separated. The separated flow extended into the wake leading to a deflection of the wake, effectively changing the camber of the aerofoil pushing the shock further upstream. When the shock reached far enough upstream it weakened and the boundary-layer reattached. As the separation bubble reattached the effective camber decreased causing the shock to move downstream once more. As the shock moves downstream it strengthened until it causes separation and the process repeats.

Iovnovich and Raveh [104] published a study on the shock-induced boundary-layer separation of the flow past three aerofoils, the subsonic NACA 0012, the supercritical RA16SC1, and the thin transonic/supersonic NACA 64A204. The type of buffet studied is associated with upper-surface shock oscillations at an angle of attack. It was found that buffet onset could be well predicted using URANS, along with a fair prediction of the buffet frequency. However the buffet amplitude and offset conditions could not be accurately predicted. For buffet onset it was found that the shock location was the most important factor in the onset mechanism, with the shock location slightly aft of the location of maximum camber for all the aerofoils, where the local camber is near zero. Buffet onset is not driven by the bursting of the separation bubble behind the shock. Buffet offset for all the aerofoils had the flow fully separated aft of the shock with the shock located near the leading edge and the aerofoils were stalled. The mechanism proposed is generally in agreement with Raghunthan *et al.* [103]. The mechanism proposed for shock-buffet is dependant on a combination of factors, which are

- *“Wedge effect”* in which the separation region acts as a geometrical wedge increasing shock strength and changing the shock from normal to oblique
- *“Dynamic effect”* in which, as the shock moves upstream, the Mach number in front of the shock increases relative to the shock, resulting in a stronger shock
- *“Aerofoil curvature effect”* that weakens the shock as it moves upstream and the aerofoil becomes more curved

Starting at the most downstream location the separation bubble pushes the shock upstream strengthening it, with the wedge and dynamic effects dominating over the curvature effect. When the shock reaches the upstream position the aerofoil curvature effect now dominates over the wedge and dynamic effects. As the shock weakens the boundary-layer reattaches followed by the rest of the flow field after a lag. As the flow field reattaches the shock travels downstream strengthening and when it reaches the downstream position it causes separation initiating a new cycle.

5.3 BGK No. 1 Aerofoil Results

5.3.1 Grids

Three grids were generated and their sizes are given in Table 5.2. The blocking is of the C-H type of a similar setup to Xiao *et al.*[3] with 256 points on the aerofoil upper and lower surfaces, 128 in the wake and 64 in the normal direction. The medium grid is shown in Figure 5.5. The coarse and fine grids are a coarsening or a refinement of the medium grid by a factor of two in each direction. To calculate the initial cell spacing the following equations where used. They are based on the turbulent flow over a flat plate to give a single point in the laminar sub-layer of the boundary-layer. The inputs for the equations are the Reynolds number, characteristic length and desired y^+. First the temperature was calculated using

Table 5.2: Grid Sizes

Grid	Number of nodes
coarse	24,576
medium	98,304
fine	221,184

$$T = \frac{288.15}{1 + \frac{\gamma - 1}{2}} \tag{5.2}$$

followed by the pressure

$$p = \frac{101325}{\left(1 + \frac{\gamma-1}{2}\right)^{\frac{\gamma}{\gamma-1}}} \tag{5.3}$$

Then using Sutherland's law the viscosity can be calculated

$$\mu = 1.7894 \times 10^{-5} \left(\frac{T}{288.15}\right)^{\frac{3}{2}} \frac{288.15 + 110}{T + 110} \tag{5.4}$$

The density is calculated using the equation for a perfect gas

$$\rho = \frac{p}{RT} \tag{5.5}$$

from the equation for the Reynolds number the freestream velocity can be calculated

$$U_\infty = \frac{Re\mu}{\rho l} \tag{5.6}$$

The Schlichting skin-friction correlation for a turbulent boundary-layer is

$$c_f = (2\log_{10}(Re) - 0.65)^{-2.3} \tag{5.7}$$

then wall shear stress is calculated using

$$\tau_w = \frac{c_f \rho U_\infty^2}{2} \tag{5.8}$$

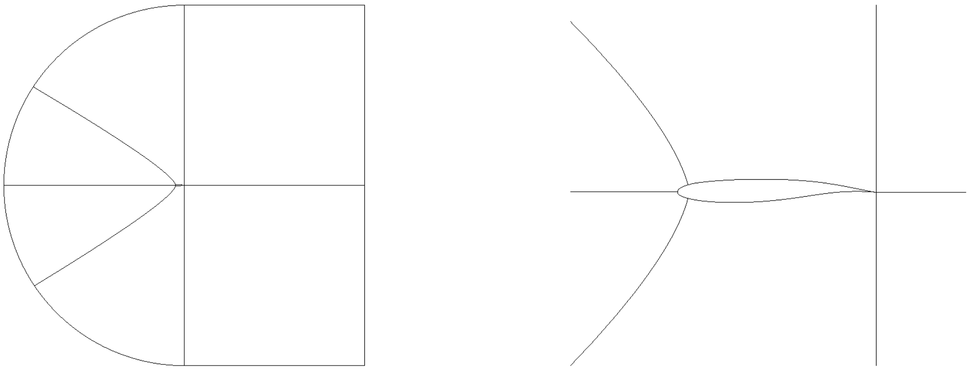

(a) Blocking

(b) Near aerofoil blocking

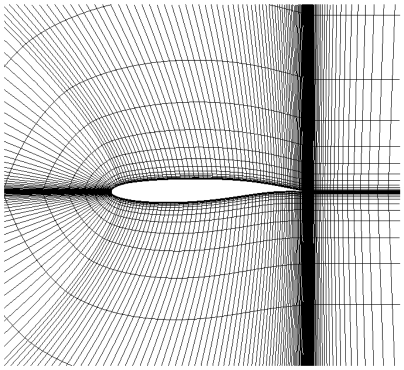

(c) Near aerofoil grid (every other line)

Figure 5.5: BGK No. 1 grid details

and the friction velocity

$$u^* = \sqrt{\frac{\tau_w}{\rho}} \tag{5.9}$$

Finally the first cell spacing can be calculate using

$$y = \frac{y^+ \mu}{\rho u^*} \tag{5.10}$$

Using a Reynolds number 20×10^6, a characteristic length of 1 and a target y^+ of 1 gave a initial cell spacing of 1.46×10^{-6}. To ensure that the $y^+ < 1$ the first cell space was chosen to be 1×10^{-6} which gives a $y^+ \approx 0.71$. Figure 5.6 shows the y^+ distribution for a calculation at Mach 0.71, Reynold number 20×10^6 and 6.97° angle of attack.

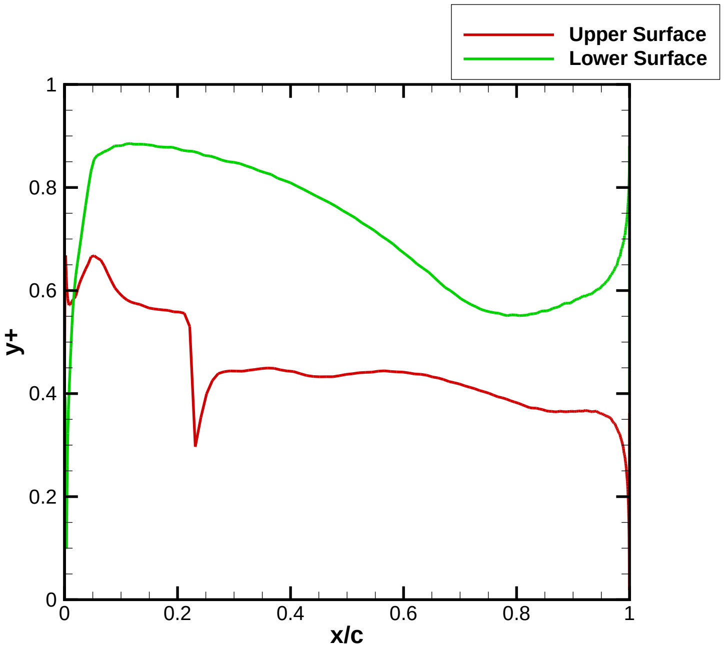

Figure 5.6: y^+ distribution around the BGK No. 1 aerofoil at $\alpha = 6.97°$, M=0.71 and Re=20×10^6

5.3.2 Probe Locations

Table 5.3 gives the location of the pressure taps and the probe locations used in the analysis of the calculations.

5.3.3 Reduced Frequency Calculation

Reduced frequency k is defined [3] as

$$k = \frac{\pi f c}{U_\infty} \tag{5.11}$$

Table 5.3: Pressure taps and probe locations

Probe	x/c	y/c
E	0.200000	0.058386542
F	0.250000	0.061595008
G	0.300000	0.063864008
H	0.350000	0.065301239
I	0.400000	0.066004328
J	0.450000	0.065981880
K	0.500000	0.065223873
L	0.550000	0.063659132
M	0.591000	0.061656490
N	0.632000	0.058887668
O	0.673000	0.055237915
P	0.714000	0.050626419
Q	0.755000	0.045050010
R	0.796000	0.038576253
S	0.837000	0.031455696
T	0.870000	0.024903920
A	1.000000	0.000000000
B1	0.795000	0.087300000
B2	0.795000	0.112000000
B3	0.795000	0.126000000
C1	0.591000	0.118000000
C2	0.591000	0.136000000
C3	0.591000	0.157000000
D1	0.500000	0.125000000
D2	0.500000	0.138000000
D3	0.500000	0.157000000

where f is the frequency, c is the chord and U_∞ is the free-stream velocity.

5.3.4 Convergence Studies

A number of convergence studies where completed to find the effect of various solver parameters. The parameters studied where the number of pseudo steps, the time step size and the grid density. For all of these studies the test conditions used were Mach 0.710, angle of attack 6.97° and Reynolds number 20×10^6 using the medium grid. The number of explicit steps used to start the calculation was set to 500 with a CFL of 0.4 followed by 10,000 implicit steps using a CFL of 2.0. The steady convergence was set to 1.0×10^{-5} using the SST turbulence model.

5.3.5 Pseudo Steps Study

Pseudo steps are used to iterate to the real time solution. The number of these steps can be changed to allow different levels of convergence. The unsteady parameters used were 6,000 time steps using a time step of 0.05 non-dimensional time with an unsteady tolerance of 0.001. The number of pseudo steps allowed for each unsteady time step was varied in this study, the values used were 100, 500, 1,000 and 1,500. Table 5.4 gives the mean lift coefficient, the reduced frequency of oscillation and the percentage of time steps that failed to converge to the desired unsteady tolerance. By increasing the number of pseudo steps the percentage of unconverged time steps reduced and the mean lift coefficient and reduced frequency converged, as shown in Figure 5.7. Figure 5.7(a) shows the lift history and that the 100 pseudo steps caused the lift oscillations to decay to a steady solution, whereas increasing the number of pseudo steps gives almost identical unsteady oscillating lift histories. The time-averaged pressure distribution shown in Figure 5.7(c) is a reasonable match to the experimental results for all numbers of pseudo steps except for 100 pseudo steps. The skin-friction shown in Figure 5.7(d) for all numbers of pseudo steps the flow separates after the shock and on average fails to reattach. Figure 5.7(e) shows the unsteady pressure distribution

Table 5.4: Results for the pseudo steps study

Pseudo steps	Mean Cl	Reduced Frequency	Percentage of Unconverged steps
100	0.967	0.161	100%
500	0.994	0.230	28%
1,000	0.994	0.230	12%
1,500	0.993	0.230	7%
Experiment	1.016	0.25	
Xiao *et al.* [3]	1.03	0.16	

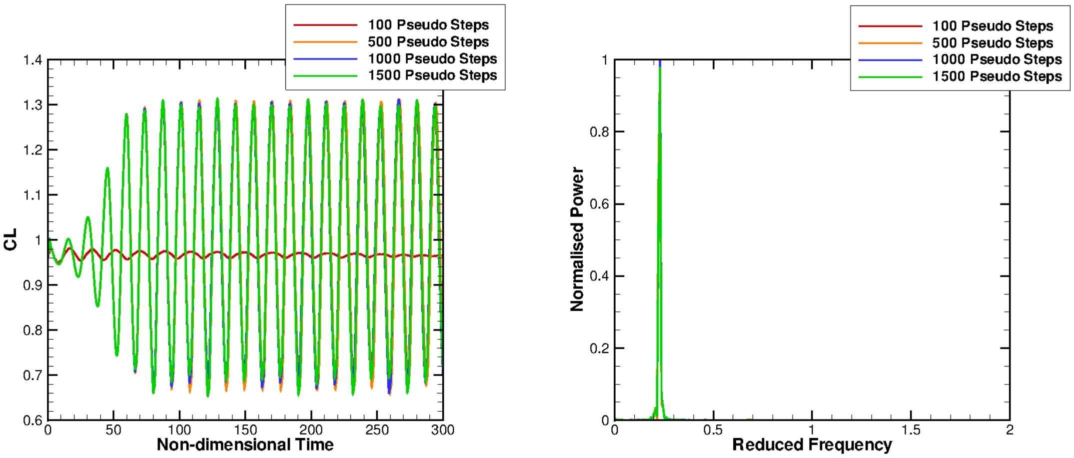

(a) Time history (b) Lift power spectral density

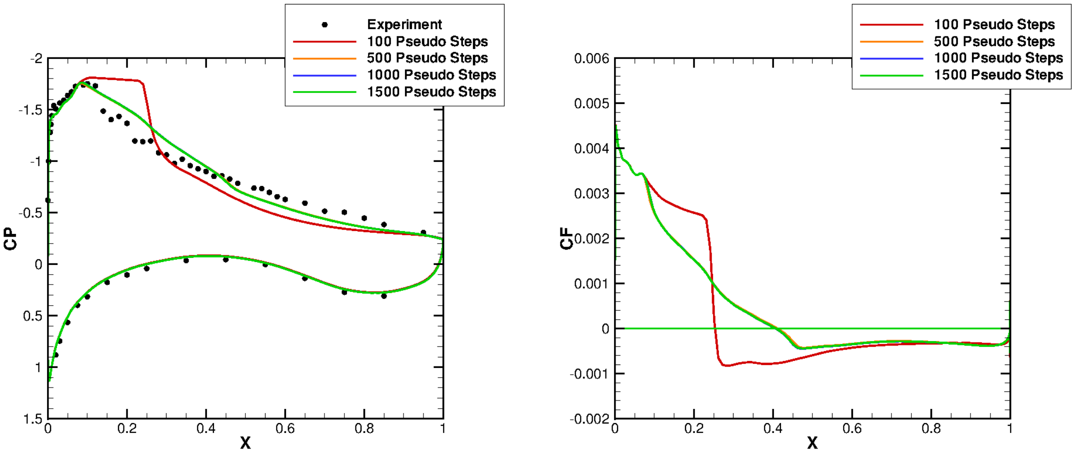

(c) Time-averaged pressure distribution (d) Time-averaged skin-friction distribution

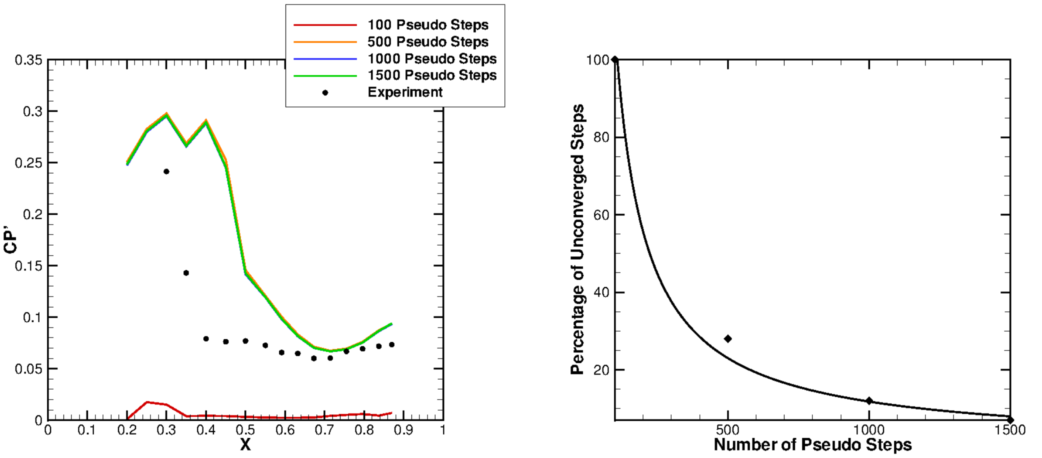

(e) Unsteady pressure distribution (f) Pseudo steps study convergence

Figure 5.7: BGK No. 1 pseudo steps study results

at the experimental pressure taps, this again shows that 100 pseudo steps results in a steady solution. The CFD results show a higher unsteadiness than the experiment and point towards the shock oscillating further back on the aerofoil. However this is in-line with the other CFD study by Xiao *et al.* [3]. For all the calculations presented from now on 1,000 pseudo steps will be used, since this is a good compromise between the potential benefit of a greater number of converged time steps and the cost of the calculation. Figure 5.7(f) shows this compromise graphically.

5.3.6 Time Step Study

The non-dimensional time steps used were 0.05 (6,000 steps), 0.025 (12,000 steps), 0.0125 (24,000 steps) and 0.00625 (48,000 steps). All the calculations were ran to 300 non-dimensional time. The unsteady parameters used were an unsteady tolerance of 0.001 and 1000 pseudo steps.

A time step study was not performed by Xiao *et al.* [3], but previous studies on the 18% thick circular-arc aerofoil by Rumsey *et al.* [96] showed that the reducing the time step converges the reduced frequency. This trend can also be seen in the results presented in Table 5.5, with both the reduced frequency and the mean coefficient of lift converging.

Table 5.5: Results for the time step study

Time Step	Mean Cl	Reduced Frequency
0.05	0.994	0.230
0.025	0.998	0.230
0.0125	1.002	0.238
0.00625	1.001	0.238
Experiment	1.016	0.250
Xiao *et al.* [3]	1.03	0.16

The results of the present study are given Figure 5.8. The time-averaged pressure distribution shows all the tested time-steps are in good agreement with the experimental data. The skin-friction shows that all the time steps are on average fully separated after the shock with no reattachment. The unsteady pressure distribution shows that as the time step increases the unsteadiness also increases with reducing time step. Since the cost of the calculation approximately doubles when the time step is halved a time step of 0.0125 was chosen for the remaining calculations as a compromise between cost and accuracy.

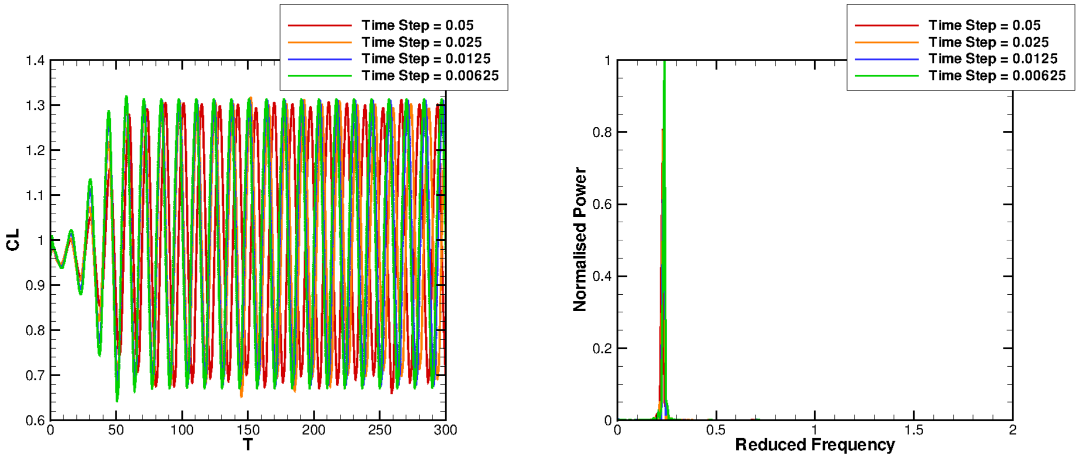

(a) Time history (b) Lift power spectral density

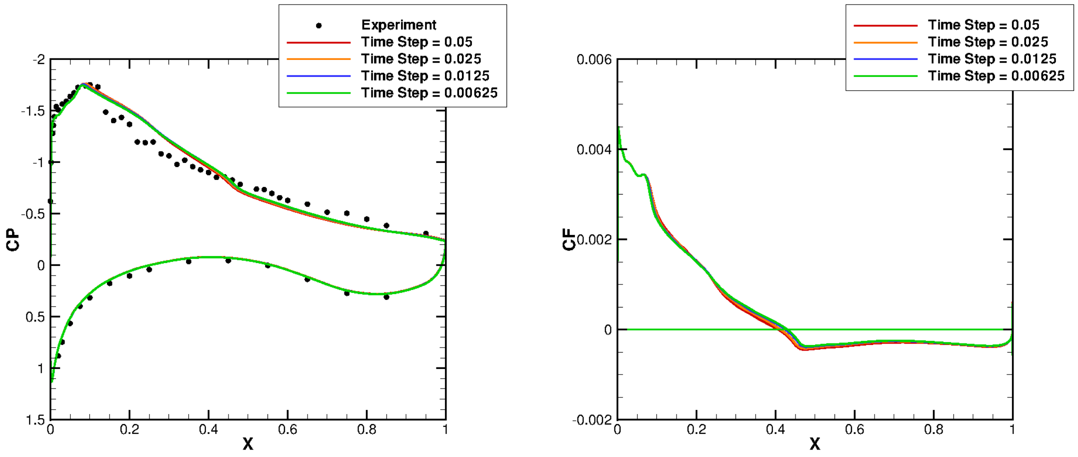

(c) Time-averaged pressure distribution (d) Time-averaged skin-friction distribution

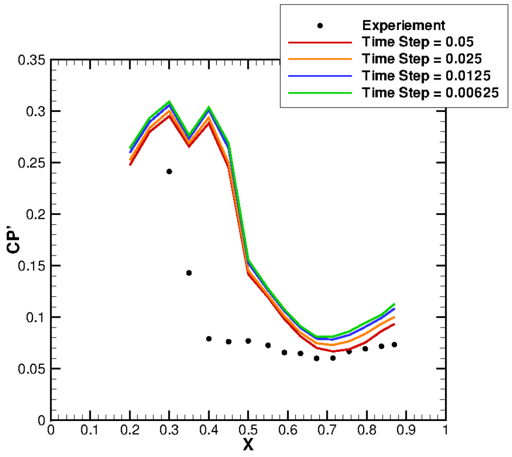

(e) Unsteady pressure distribution

Figure 5.8: BGK No. 1 time step study results

5.3.7 Grid Refinement Study

For the grid refinement study the three grids given in Table 5.2 where used. From the previous studies the unsteady parameters used were 12,000 time steps using a time step of 0.0125 non-dimensional time leading to a total run length of 150 non-dimensional time with an unsteady tolerance of 0.001 and 1000 pseudo steps.

Xiao *et al.*[3] found the dominant frequency to be independent of the grid used. Other CFD studies on the 18% thick circular-arc aerofoil found that the whilst the reduced frequency was relatively insensitive to grid density it still varied by 2-5%. Changing the grid in the study by Xiao *et al.* changed the pressure distribution and the lift coefficient. Table 5.6 shows the results from the grid study. The mean lift is reasonably well converged, but the reduced frequency is still converging towards the experimental result.

Table 5.6: Results for grid refinement study

Grid	Mean Cl	Reduced frequency
Coarse	1.042	-
Medium	1.002	0.238
Fine	0.997	0.245
Experiment	1.016	0.250
Xiao *et al.* [3]	1.03	0.16

More results are given in Figure 5.9, it can be seen that the coarse grid was unable to capture the unsteady flow. The medium and fine grids both produced the expected unsteady flow with the amplitude of the lift oscillations being very similar. The difference in the mean pressure and skin-friction distributions are minimal between the medium and fine grids, whereas the coarse grid shows a strong steady shock. The unsteady pressure distributions are similar for the medium and fine grids and have a higher intensity than the experimental results. The coarse grid has very little unsteadiness as expected from the lift history. All the remaining calculations use the medium grid.

5.3.8 Buffet Boundary Estimate

To calculate the buffet boundary using unsteady CFD calculations takes significant computational time with at least three calculations required for each point along the buffet boundary. In order to increase the speed of the buffet boundary prediction using steady computations would be advantageous. If the lift is plotted against iteration number useful patterns emerge. Even though these results are not time accurate and represent no real time history, if the lift coefficient stabilises after an initial oscillation the flow is steady. If these oscillations per-

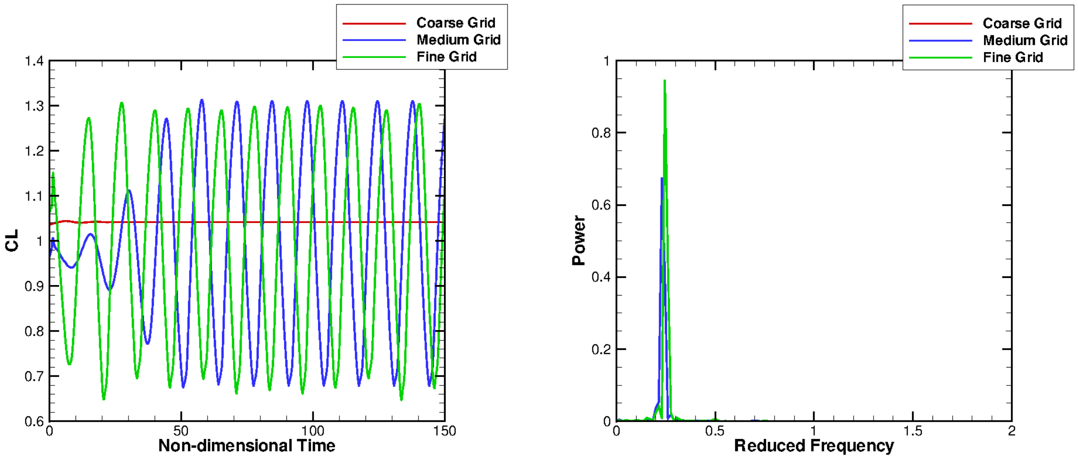

(a) Time history (b) Lift power spectral density

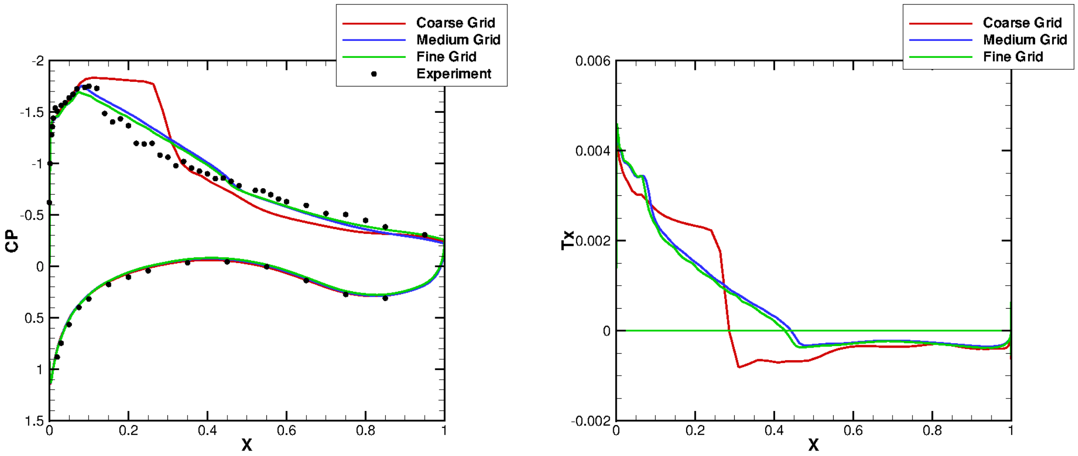

(c) Time-averaged pressure distribution (d) Time-averaged skin-friction distribution

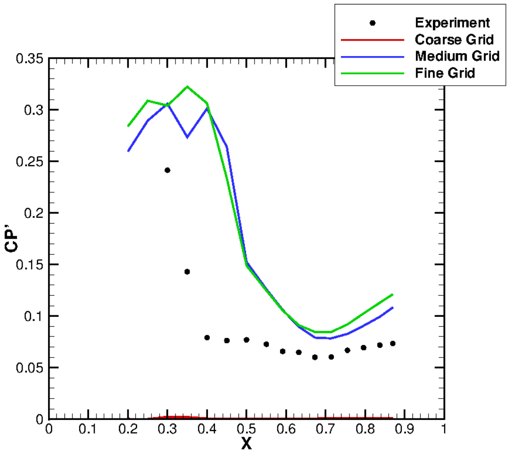

(e) Unsteady pressure distribution

Figure 5.9: BGK No. 1 grid refinement study results

sist then the flow is possibly unsteady. This was shown by Singh [105] using a NACA0012 aerofoil.

A large number of steady state calculations were ran using the medium grid to estimate the buffet boundary. The cases were ran to 40,000 implicit iterations using a CFL of 2.0 and with the lift coefficient output at each iteration. The lift coefficient history and the residual of the steady calculation can be used to estimate whether the the flow is steady or unsteady and therefore estimate the buffet boundary. The test region is shown graphically in Figure 5.10 for both using the lift coefficient and residual as the estimator. In the figure the regions of experimental shock oscillation and the experimental buffet boundary are highlighted. Using the lift coefficient as the estimator the region of shock oscillation is well captured, but the experimental buffet boundary is not. This is not surprising as the most likely feature to cause the lift coefficient to oscillate in this flow is an oscillating shock wave. Using the residual as the estimator results in significantly more unsteady results. These cover the entire buffet region, but also extend outside the experimentally estimated region.

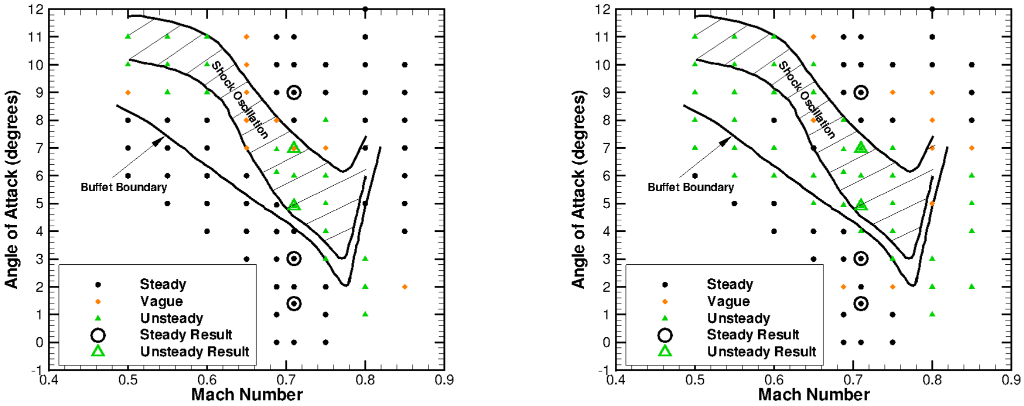

(a) Based upon the Cl history

(b) Based upon the residual

Figure 5.10: Buffet boundary estimate

Figure 5.11 shows a comparison of a number of different angles of attack for Mach number 0.71. From the lift coefficient history it can be seen that the angles 1.396°, 3.017° and 9.0° are steady. The angle of attack 6.97° is oscillating, but converging to a steady state and as such was defined as a vague result. The angle of attack of 4.905° was clearly unsteady. The residual plot contains the data for the Navier-Stokes residual (dot-dash line) and the turbulence model residual (solid line). For all angles of attack the Navier-Stokes residual converged to the desired convergence. However after achieving this level of convergence the angles of attack 1.396° and 3.017° both rapidly converged and the angle

4.905° oscillated. The remaining two angles of attack oscillated, but gradually damped towards further convergence. The turbulence model residual however gave a slightly different story. The lowest two angles of attack gave a steady convergence, 9.0° oscillated before damping to a steady convergence. The angle of attack of 4.905° failed to converge and its turbulence model residual oscillated. At angle of attack of 6.97° the turbulence model residual oscillated as it converged, but never settled down to a steady convergence. To give an indiction that the reason that the calculations are do not converge is not a numerical issue, this angle of attack sweep was calculated using CFL number of 5.0 and is also shown in Figure 5.11. The results at the higher CFL number confirm that the angles of attack of 1.396° and 3.017° are both steady. The results also confirm that angle of attack of 4.905° fails to converge and therefore is likely to be unsteady. The higher angles of attack of 6.97° and 9.0° are less clear, as both converge to the desired level. The 6.97° angle of attack the turbulence model residual oscillated as it converged and both angles of attack had oscillations as the Navier-Stokes residual converged. Since their convergence was quite different from the steady cases these would also be worth looking into. This method has some promise for a fast initial estimate of whether a calculation is likely to be unsteady, but as the results look different for each CFL number care must be taken to only compare iteration histories of calculations with the same CFL number. This leaves some calculations with convergence histories that are different from the rapid smooth convergence of steady calculations giving an indication of which calculations are worth running unsteady.

Figure 5.12 shows the lift curve for the steady calculations. It can be observed that the CFD lift coefficient values are higher for all angles of attack tested below 6.97°. Stall is at the same point as the experiment at about 5°.

5.3.9 Mach 0.71 Angle of Attack Sweep

An angle of attack sweep for the Mach number 0.71 ran as unsteady calculations will be presented here and will cover the region before shock-induced oscillation, shock-induced oscillation and the region after the shock-induced oscillation. For the unsteady runs only data from 50 to 150 non-dimensional time will be used for statistical analysis to remove transient effects at the start of the calculations. Following the convergence studies each angle of attack will be ran for 150 non-dimensional time using a time step of 0.0125 and 1000 pseudo steps on the medium grid.

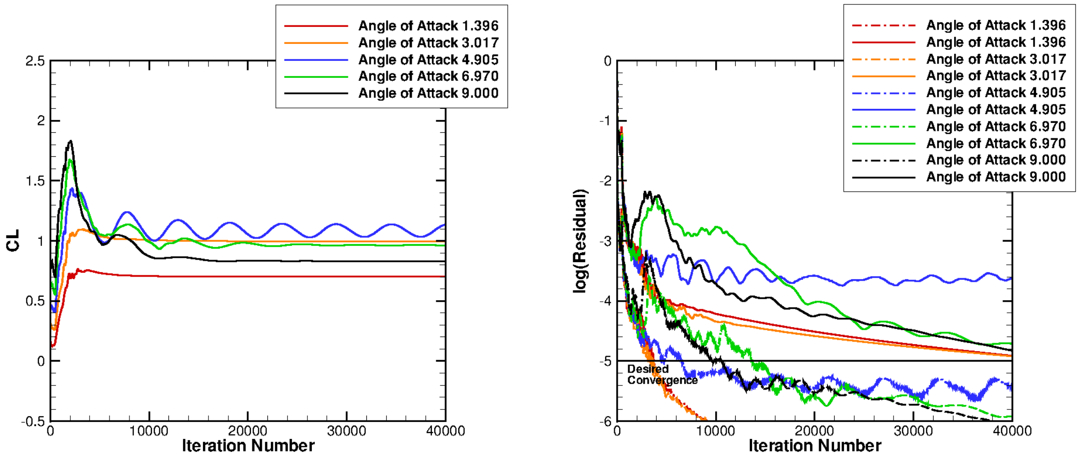

(a) Lift history at CFL of 2.0 (b) Residual history of CFL of 2.0

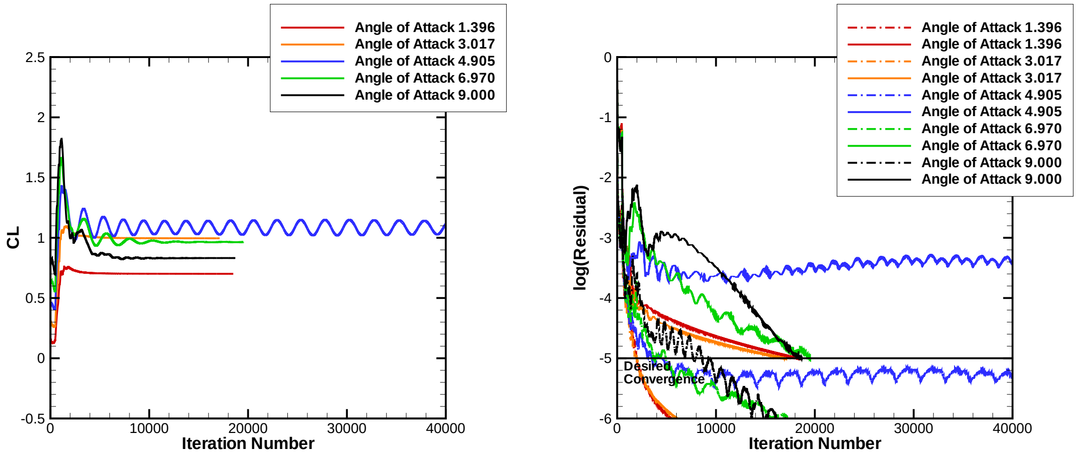

(c) Lift history at CFL of 5.0 (d) Residual history at CFL of 5.0

Figure 5.11: Comparison of Mach 0.71 angle of attack sweep for steady calculations

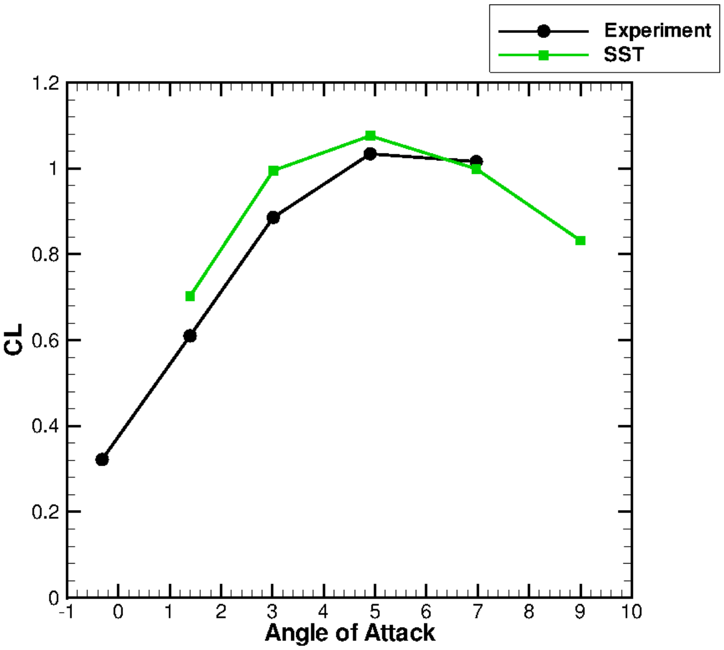

Figure 5.12: Lift curve for the Mach 0.71 angle of attack sweep

1.396° **Angle of Attack**

This case is the lowest angle of attack ran and converged to a steady solution. This agrees with the estimate in Figure 5.10 using both the lift coefficient and residual, this also agrees with the experimental estimate. The CFD study by Xiao *et al.* used an angle of attack of 1.3° to account for wind tunnel correction. The comparison of the pressure distributions is shown in Figure 5.13 and the lift coefficient is shown in Table 5.7. The pressure distributions for both the original and the corrected angles of attack fail to match the experimental results. The lower angle of attack does shift the shock towards the experimental location, but does not predict its location correctly. This is in-line with the results by Xiao *et al.* who used the lagged k-ω turbulence model and also failed to predict the experimental shock location. There is no separation in this case from the skin friction distribution as expected.

Table 5.7: Coefficient of lift comparisons for angle of attack 1.396°

Angle of Attack	CFD Cl	Experimental Cl
1.396	0.701	0.610
1.300	0.683	-

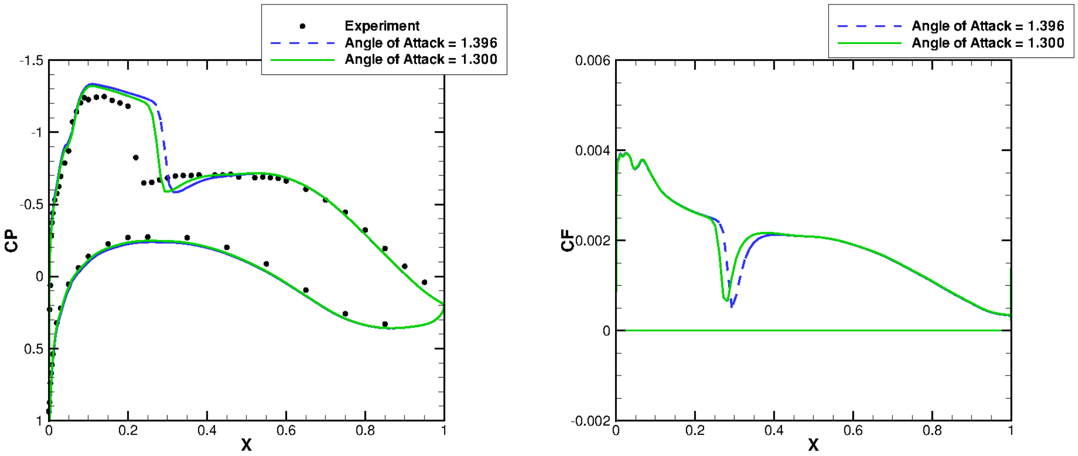

(a) Pressure distribution

(b) Skin-friction distribution

Figure 5.13: BGK No. 1 angle of attack 1.396° results

3.017° **Angle of Attack**

This angle of attack also converged to a steady solution. This matches both the experimental and the steady calculation estimates in Figure 5.10. Figure 5.14 presents the pressure and skin-friction distributions. The pressure distribution does not match the experiment so well, as the shock is predicted too far downstream. There is also a small region of separation directly after the shock which reattaches, the pressure distribution implies that predicted the region of separation is smaller than in the experiment, due to the late shock.

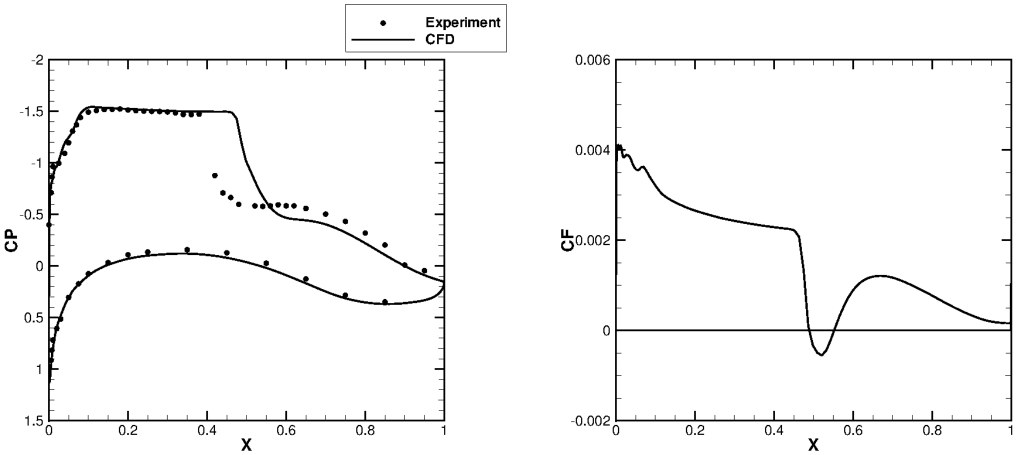

(a) Pressure distribution

(b) Skin-friction distribution

Figure 5.14: BGK No. 1 angle of attack 3.017° results

4.905° **Angle of Attack**

This angle of attack is unsteady as shown in Figure 5.10 as shown by both the experimental and the steady calculation estimates. The time history shown in Figure 5.15(a) is unsteady, due to shock-induced oscillation. The pressure distribution matches the experimental results reasonably well. The time-averaged skin-friction plot shows a region of separation after the shock and another at the trailing edge. The unsteady pressure distribution shows a region $0.45 < x/c < 0.7$ where the CFD predicts a much larger amount of unsteadiness. This region corresponds to the time-average region of separation in the skin friction plot. It may be that in the experiment this region of separation was much smaller than that predicted by the CFD. The magnitude and phase angle (obtained from an FFT of each probe at the shock oscillation frequency) of the unsteady pressure at the pressure taps are shown in Figure 5.16. As expected the magnitude has a very similar profile to the unsteady pressure in Figure 5.15(e). The phase angle has three regions, for $x/c < 0.35$ the phase angle is constant. For $0.4 < x/c < 0.6$ the phase angle is constant at a different phase angle to the first region. This region corresponds to the time-average separation bubble. The final region $0.6 < x/c$ is linear with an increasing phase angle and corresponds to the trailing edge separation. This could indicate a pressure wave travelling with a constant speed.

Figure 5.17 shows the pressure distribution at different time instants during one period, (a) is for the downstream shock movement and (b) is for the upstream shock movement. The time instant $\tau = 0.0$ corresponds to the time at which the lift is at a maximum and time instant $\tau = 1.0$ represents a complete cycle. Shock motion is clearly visible and covers the range $0.34 < x/c < 0.46$. The Mach number contours and streamline plots are shown in Figures 5.18 and 5.19. At $\tau = 0.0$ the shock is at $x/c = 0.46$ with a separation bubble directly behind the shock and trailing edge separation. Between $\tau = 0.1$ and $\tau = 0.4$ the shock moves upstream and between $\tau = 0.6$ and $\tau = 0.9$ the shock moves downstream. As the shock moves upstream the two regions of separation merge into one fully separated region and moves upstream with the shock movement. When the shock has reached furthest upstream point ($x/c = 0.34$ at $\tau = 0.5$) the two regions of separation split to become distinct again. As the shock moves downstream the two regions of separation become smaller and by $\tau = 0.8$ the trailing edge separation has disappeared with only a small separation bubble directly behind the shock left. At $\tau = 1.0$ the shock is at its most downstream position, the shock-induced separation region has grown and a region of trailing edge separation has also reappeared. The cycle of separated flow and shock movement then repeats. This pattern of separation can also be seen in the skin-friction plots in Figure 5.17 (c) and (d).

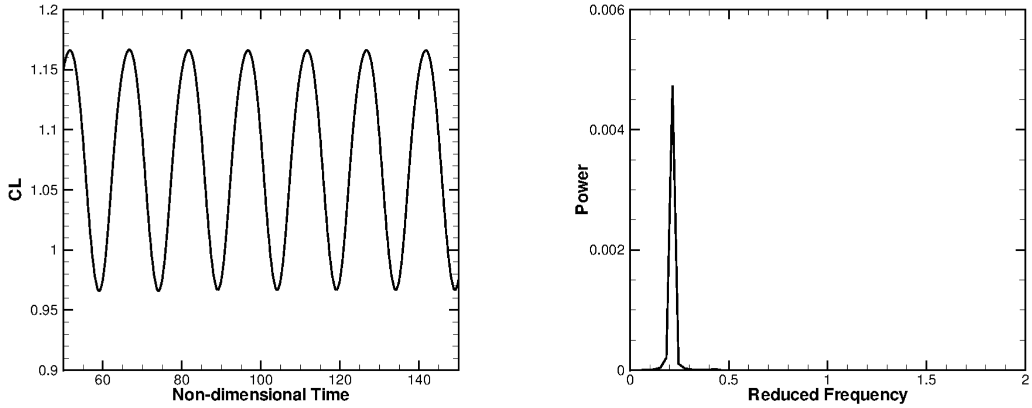

(a) Time history

(b) Lift power spectral density

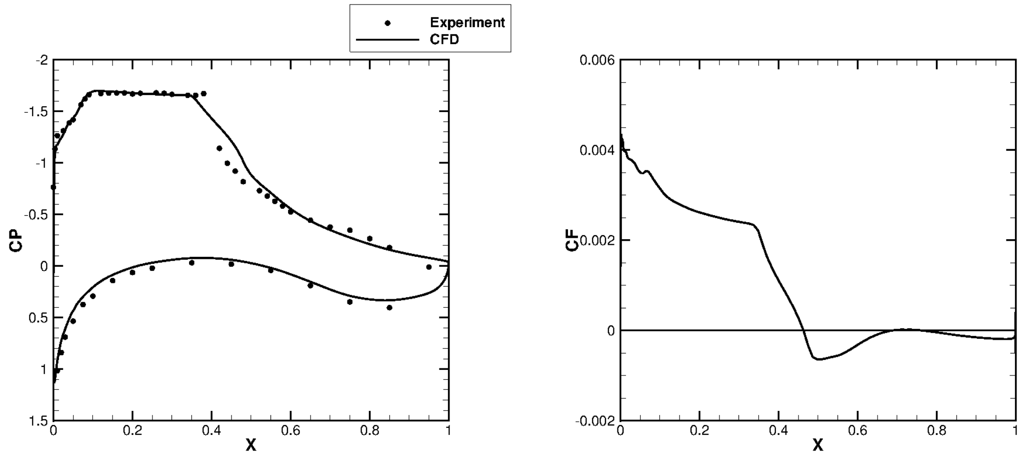

(c) Time-averaged pressure distribution

(d) Time-averaged skin-friction distribution

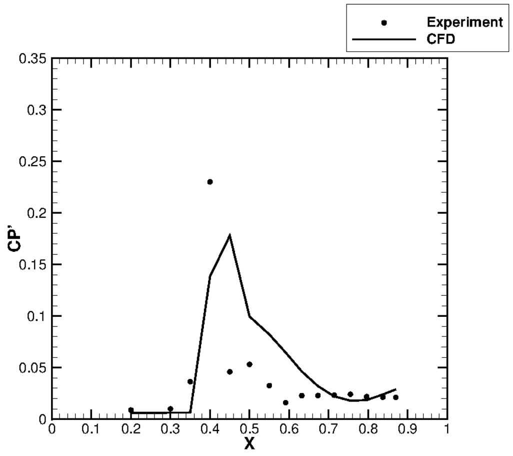

(e) Unsteady pressure distribution

Figure 5.15: BGK No. 1 angle of attack 4.905° results

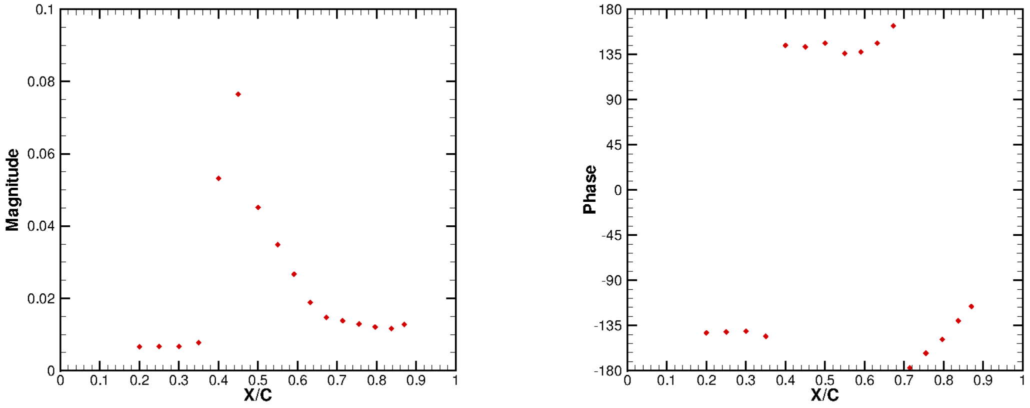

(a) Magnitude (b) Phase angle

Figure 5.16: Pressure wave propagation for angle of attack 4.905°

A similar analysis of the calculation was performed to that of Xiao *et al.* [3]. As explained in the introduction the mechanism for a self-sustained shock oscillation expects a pressure wave to travel downstream from the shock in the region of separation to the trailing edge. Upon arrival another pressure wave travels upstream outside the separated region. This is shown in Figure 5.3. The period of the shock oscillation is given by Equation 5.1. By using two-point cross-covariance the direction and speed of the pressure waves can be calculated avoiding any empirical formula. This was achieved using the MATLAB command xcov(x, y). Figure 5.20 presents the cross-covariance of the surface pressure taps as well as a number of probes that create three paths outside the separated region. The location of the probes and the pressure taps are given in Table 5.3. A positive time delay in Figure 5.20(a) indicates that a pressure wave within the separated region behind the shockwave travels downstream towards the trailing edge. Since the distance and time delays between the pressure taps are known, then the wave speed can be calculated. The Figures 5.20 (b), (c) and (d) are for three different wave paths outside the separated region and all show a negative time lag indicating that a pressure wave is moving upstream. Again the speeds can be calculated in the same manner. The wave speeds are given in the final plot in this figure. The upstream speeds are all almost identical and linear. The downstream speed is near constant downstream of the mean shock location, but upstream of the mean shock location anomalous results are obtained. These velocities can be used in Equation 5.1 to calculate the period of shock oscillation and therefore the reduced frequency. The reduced frequency for the shock oscillation calculated from the lift history using a FFT and from Equation 5.1 using the three different paths are given in Table 5.8. The different reduced frequencies are of a similar

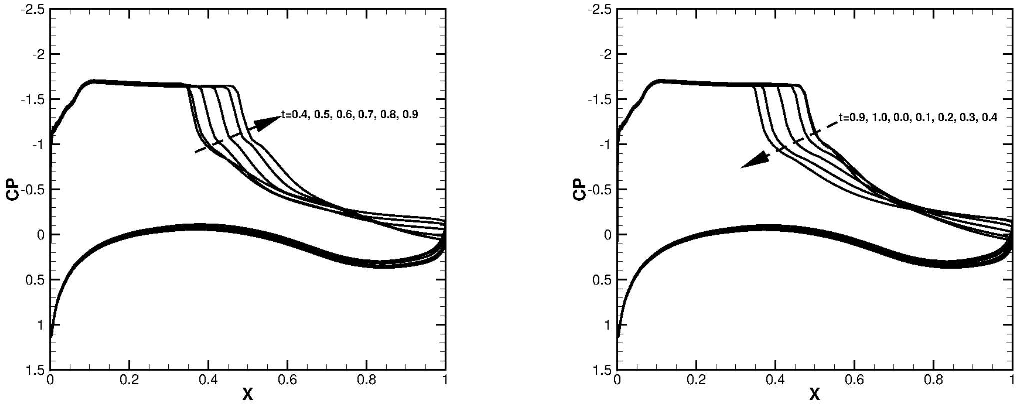

(a) Shock movement downstream: Pressure distribution

(b) Shock movement upstream: Pressure distribution

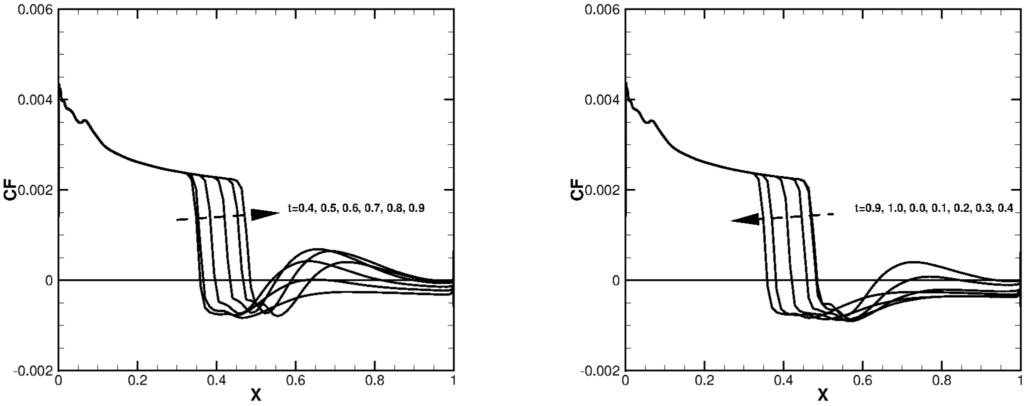

(c) Shock movement downstream: Skin-friction

(d) Shock movement upstream: Skin-friction

Figure 5.17: Unsteady shock movement during one period for angle of attack 4.905°

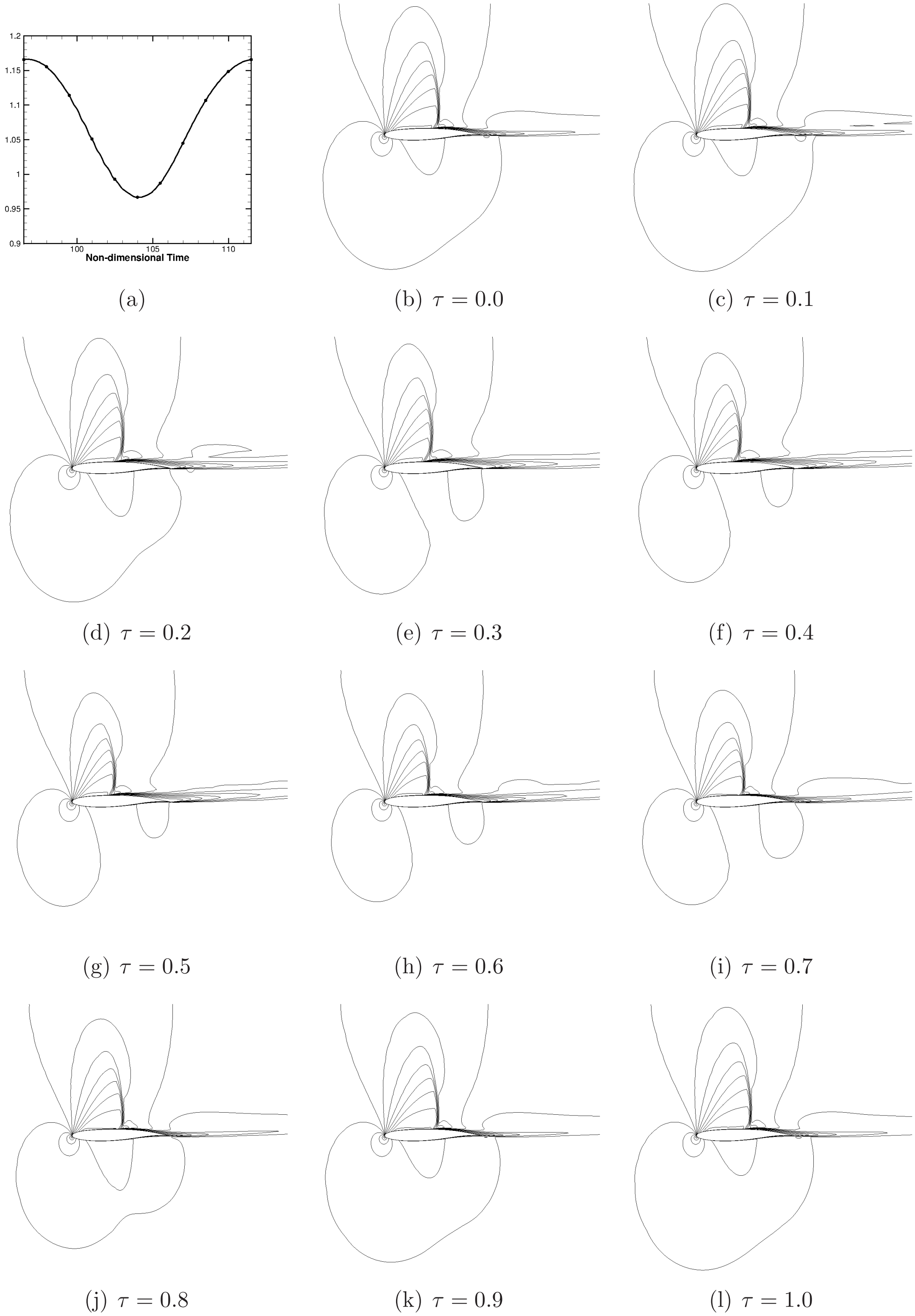

(a)

(b) $\tau = 0.0$

(c) $\tau = 0.1$

(d) $\tau = 0.2$

(e) $\tau = 0.3$

(f) $\tau = 0.4$

(g) $\tau = 0.5$

(h) $\tau = 0.6$

(i) $\tau = 0.7$

(j) $\tau = 0.8$

(k) $\tau = 0.9$

(l) $\tau = 1.0$

Figure 5.18: Mach number contours at different instants in time for one period of oscillation for angle of attack 4.905°, $\Delta M = 0.095$

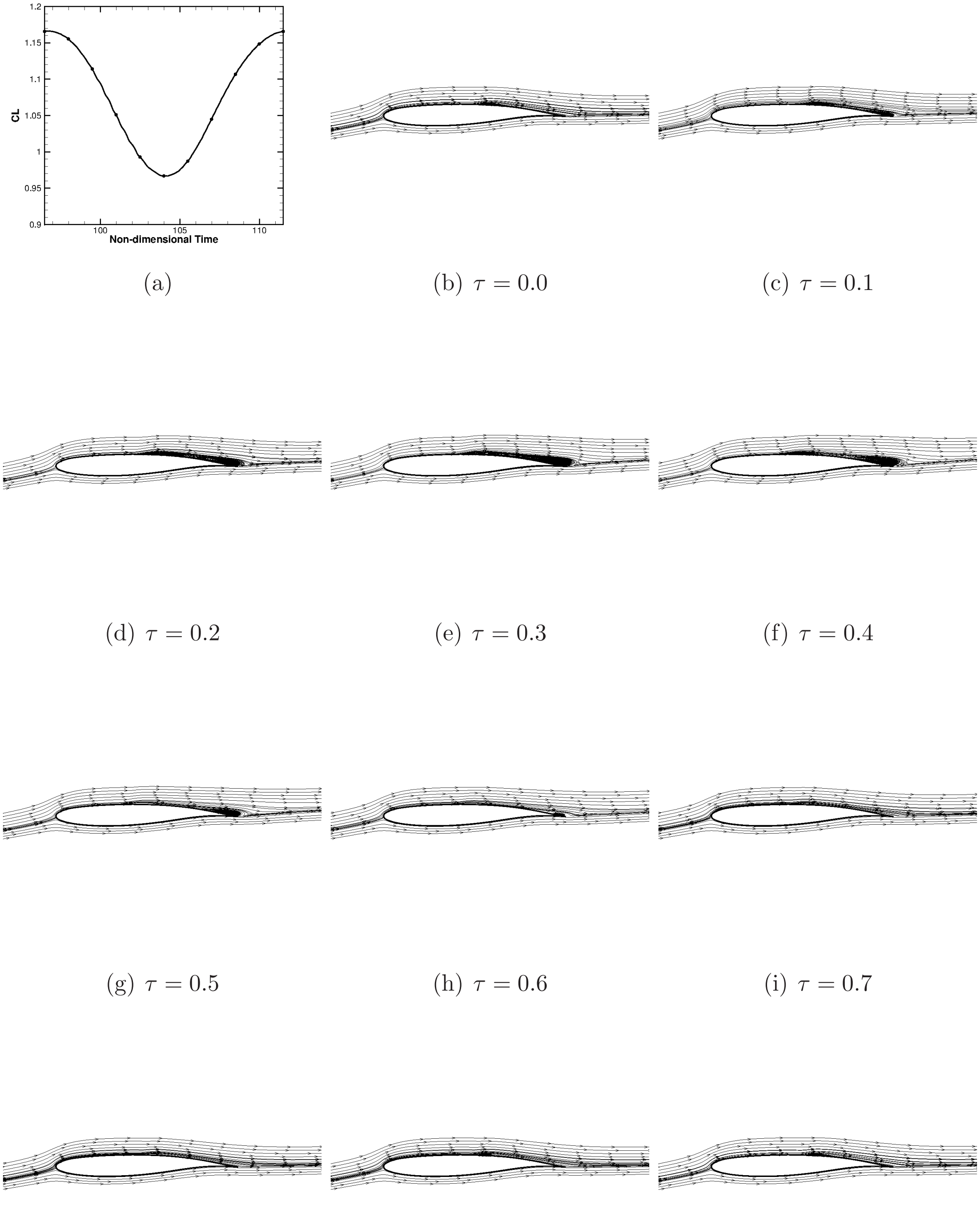

(a)

(b) $\tau = 0.0$

(c) $\tau = 0.1$

(d) $\tau = 0.2$

(e) $\tau = 0.3$

(f) $\tau = 0.4$

(g) $\tau = 0.5$

(h) $\tau = 0.6$

(i) $\tau = 0.7$

(j) $\tau = 0.8$

(k) $\tau = 0.9$

(l) $\tau = 1.0$

Figure 5.19: Streamlines at different instants in time for one period of oscillation for angle of attack 4.905°

magnitude, but are not as conclusive as the results presented by Xiao *et al.* [3].

Table 5.8: Reduced frequency results

Lift history	Path 1	Path 2	Path 3
0.215	0.273	0.250	0.239

6.97° **Angle of Attack**

This angle of attack is estimated to be unsteady in Figure 5.10, both experimentally and from the steady calculations. This is confirmed by the time history in Figure 5.21(a). The pressure distribution shown in Figure 5.21(c) has good agreement with the experimental results and the skin-friction indicates that the flow is on average separated. The unsteady pressure distribution points towards the shock oscillating further back than the experiment due to higher unsteadiness between $x/c = 0.4$ and $x/c = 0.5$. The magnitude and phase angle of the unsteady pressure taps is given in Figure 5.22. The magnitude has the same profile as the unsteady pressure distribution, but has a different magnitude to the experiment and CFD results published by Xiao *et al.* [3]. The phase angle has a similar profile to the experiment, but is offset by an average of $-92°$. This implies that there are different starting points in the shock oscillation cycle for the respective results.

Figure 5.23 shows the pressure and skin-friction distributions at different time instants throughout one cycle. The shock can be seen to oscillate between $x/c = 0.1$ and $x/c = 0.45$. The Mach number contours and streamlines throughout a single cycle are presented in Figures 5.24 and 5.25. At time instant $\tau = 0.0$ the shock is at $x/c = 0.4$ and this shock induces full separation to the trailing edge. The shock travels upstream for $0.1 < \tau < 0.4$ and travels downstream during $0.5 < \tau < 0.9$. As the shock travels downstream there is a separation bubble behind the shock and a small region of separation at the trailing edge. As the shock travels upstream the flow fully separates behind the shock and does not split into distinct regions of separation until the shock starts moving downstream again. This behaviour can be more easily seen in the skin-friction plots. This cycle of shock motion and separation then repeats.

The cross-covariance of the probes are given in Figure 5.26. A positive time delay in Figure 5.26(a) indicates a pressure wave travelling downstream in the separated region and the negative time delays in the Figures 5.26(b)-(d) indicate that a pressure wave is travelling upstream outside the separated region. As with the previous angle of attack the wave speeds can be calculated and are shown in Figure 5.26(e). The upstream wave speeds are all very similar and are

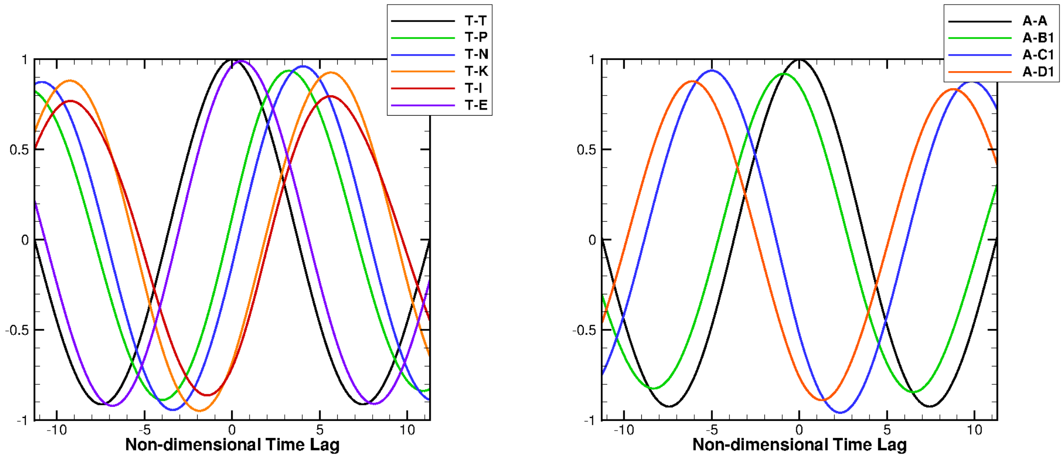

(a) Cross-covariance pressure taps (b) Cross-covariance upstream path 1

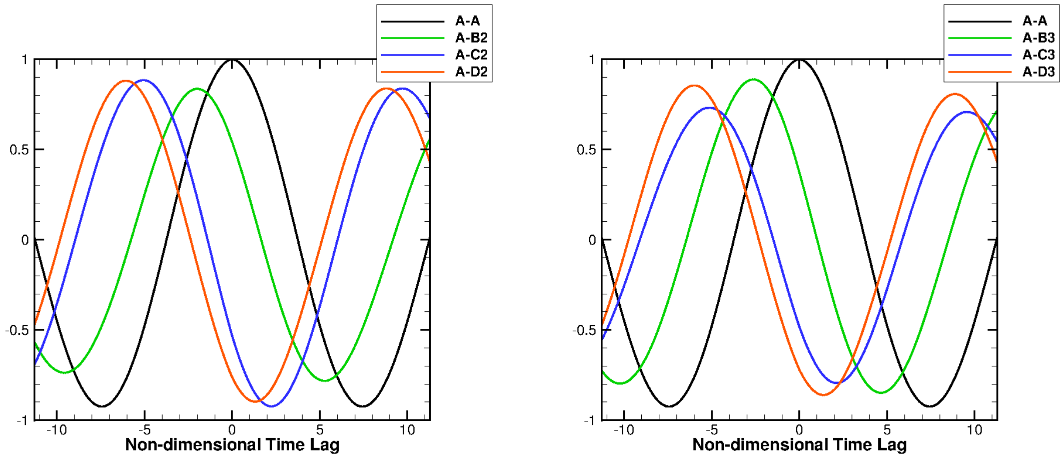

(c) Cross-covariance upstream path 2 (d) Cross-covariance upstream path 3

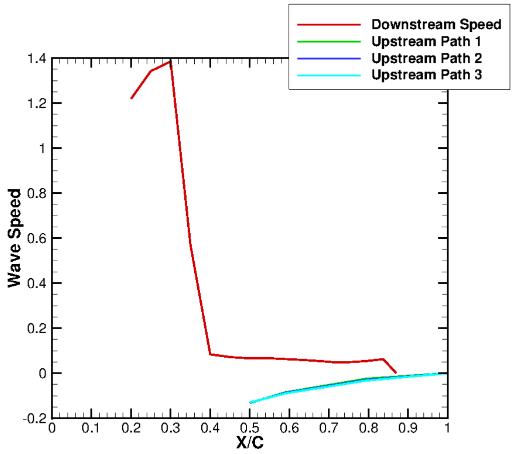

(e) Wave speeds

Figure 5.20: Cross-covariance and wave speed for angle of attack 4.905°

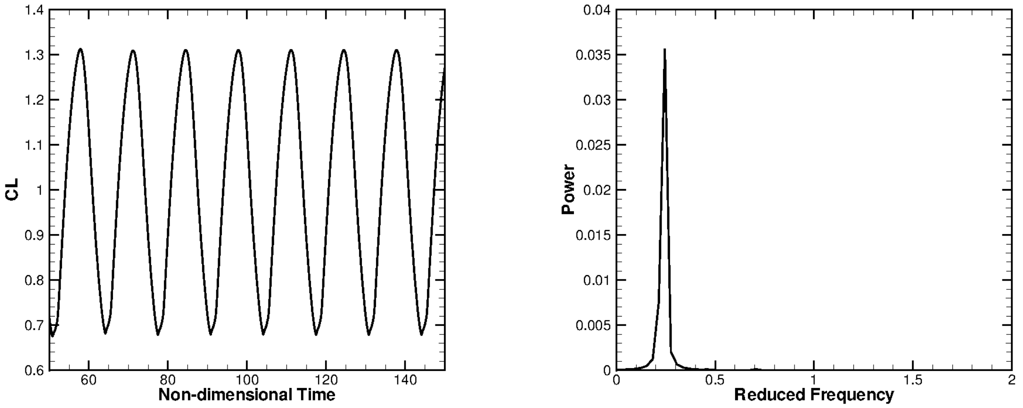

(a) Time history (b) Lift power spectral density

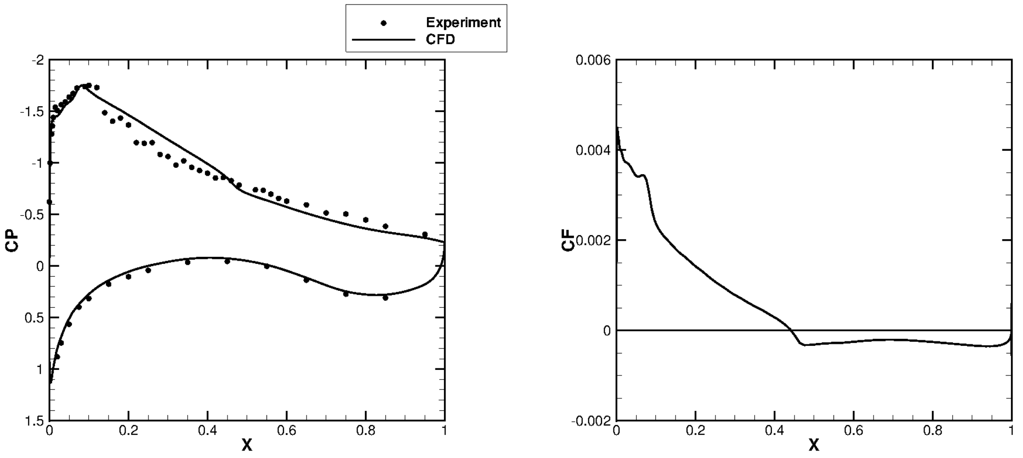

(c) Time-averaged pressure distribution (d) Time-averaged skin-friction distribution

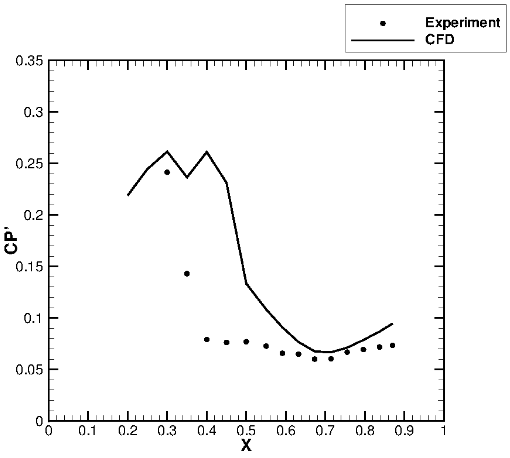

(e) Unsteady pressure distribution

Figure 5.21: BGK No. 1 angle of attack 6.97° results

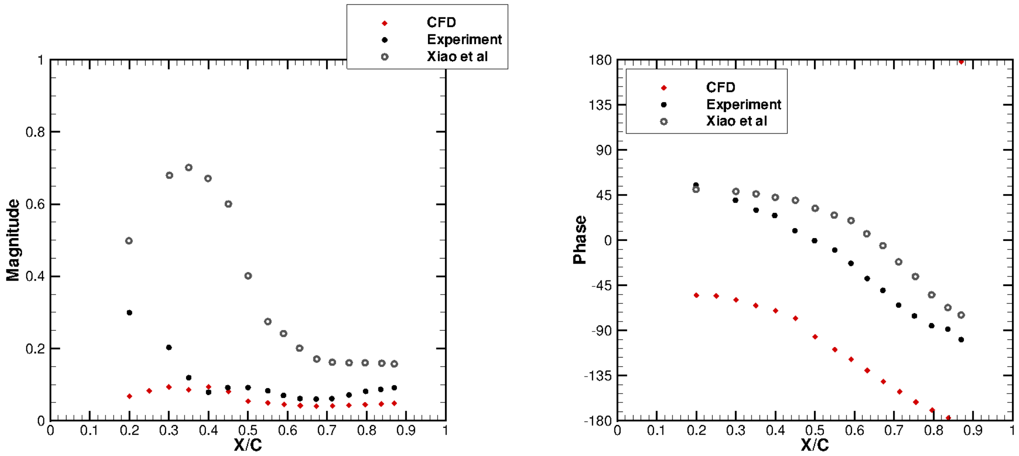

(a) Magnitude (b) Phase angle

Figure 5.22: Pressure wave propagation

near linear. The downstream wave speeds are linear until $x/c \approx 0.65$ at which point the wave speed rapidly increases. Using Equation 5.1 these speeds can be integrated to calculate the time period of shock oscillation and therefore the reduced frequencies, which are given in Table 5.9. Using this method the reduced frequencies obtained are much higher than the one obtained by a FFT of the lift history that is close to the experimental value of 0.250.

Table 5.9: Reduced frequency results

Lift History	Path 1	Path 2	Path 3
0.245	0.360	0.375	0.378

9.0° **Angle of Attack**

This angle of attack converged to a steady solution. This matches the steady calculation estimates in Figure 5.10. Figure 5.27 presents the pressure and skin-friction distributions, but there are no experimental results with which to compare. However the results are in-line with experimental observations that the flow becomes steady due to massive separation downstream of the shock with no reattachment. This can be clearly seen in the skin-friction plot.

5.4 Summary

It was shown that steady calculations can be used to estimate if a calculation is likely to be unsteady. This was confirmed by unsteady calculations at a number of different angles of attack that represent pre-, post- and shock oscillation regimes.

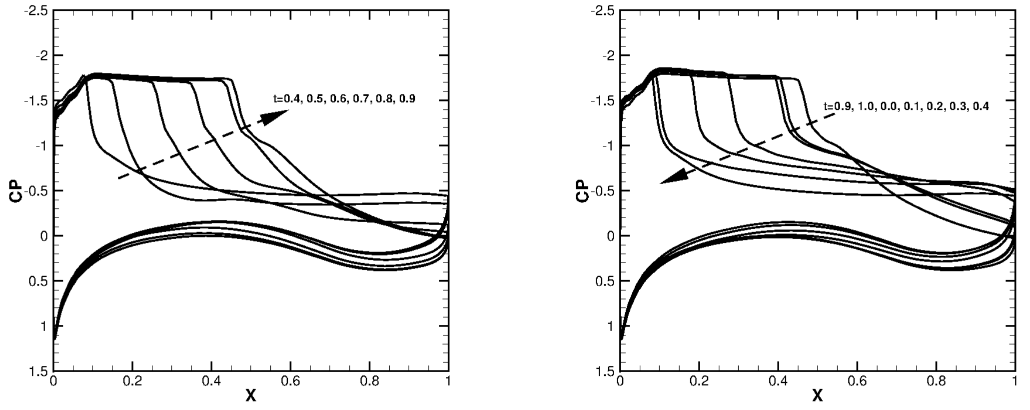

(a) Shock movement downstream: Pressure distribution

(b) Shock movement upstream: Pressure distribution

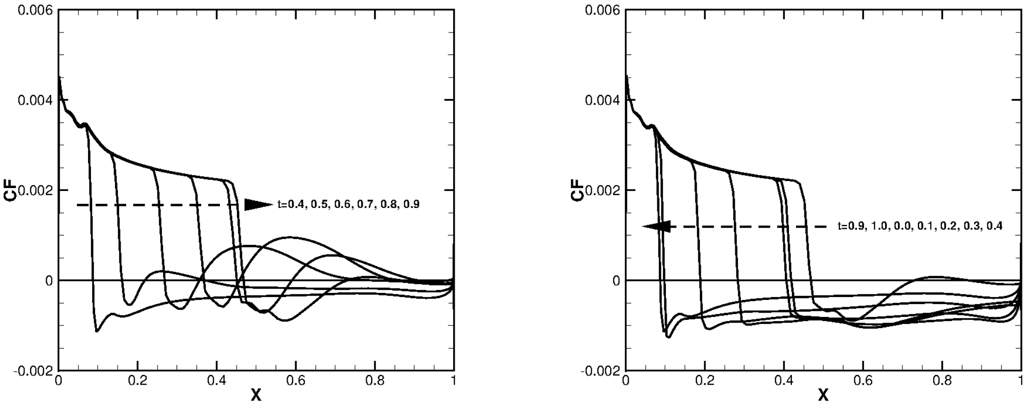

(c) Shock movement downstream: Skin-friction

(d) Shock movement upstream: Skin-friction

Figure 5.23: Unsteady shock movement during one period for angle of attack 6.97°

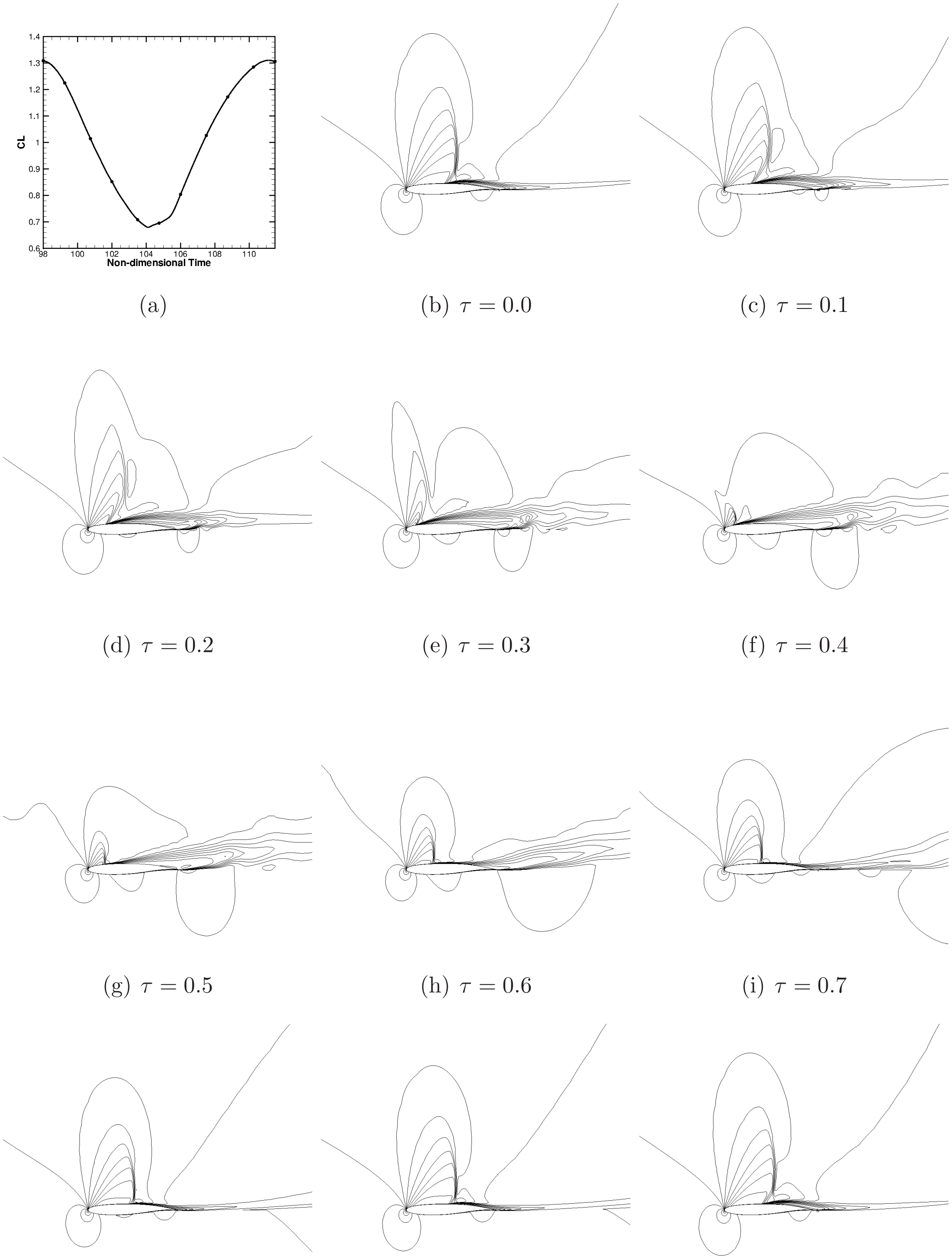

(a)

(b) $\tau = 0.0$

(c) $\tau = 0.1$

(d) $\tau = 0.2$

(e) $\tau = 0.3$

(f) $\tau = 0.4$

(g) $\tau = 0.5$

(h) $\tau = 0.6$

(i) $\tau = 0.7$

(j) $\tau = 0.8$

(k) $\tau = 0.9$

(l) $\tau = 1.0$

Figure 5.24: Mach number contours at different instants in time for one period of oscillation for angle of attack 6.97°, $\Delta M = 0.095$

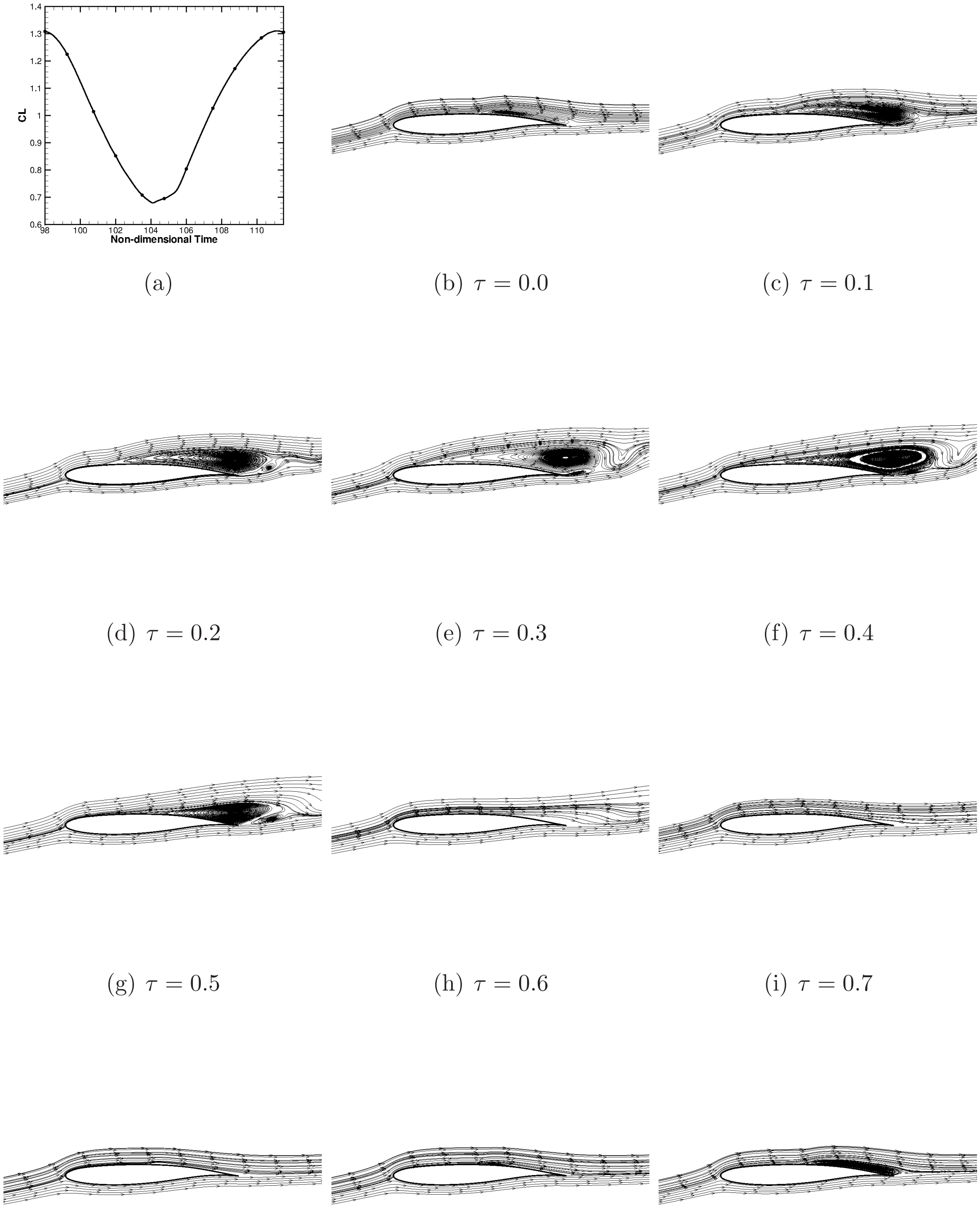

(a) (b) $\tau = 0.0$ (c) $\tau = 0.1$

(d) $\tau = 0.2$ (e) $\tau = 0.3$ (f) $\tau = 0.4$

(g) $\tau = 0.5$ (h) $\tau = 0.6$ (i) $\tau = 0.7$

(j) $\tau = 0.8$ (k) $\tau = 0.9$ (l) $\tau = 1.0$

Figure 5.25: Streamlines at different instants in time for one period of oscillation for angle of attack 6.97°

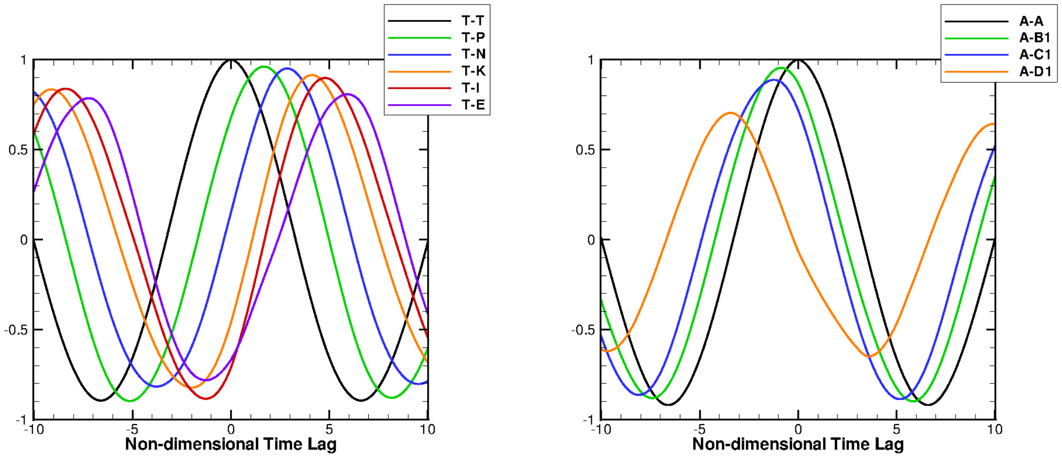

(a) Cross-covariance pressure taps (b) Cross-covariance upstream path 1

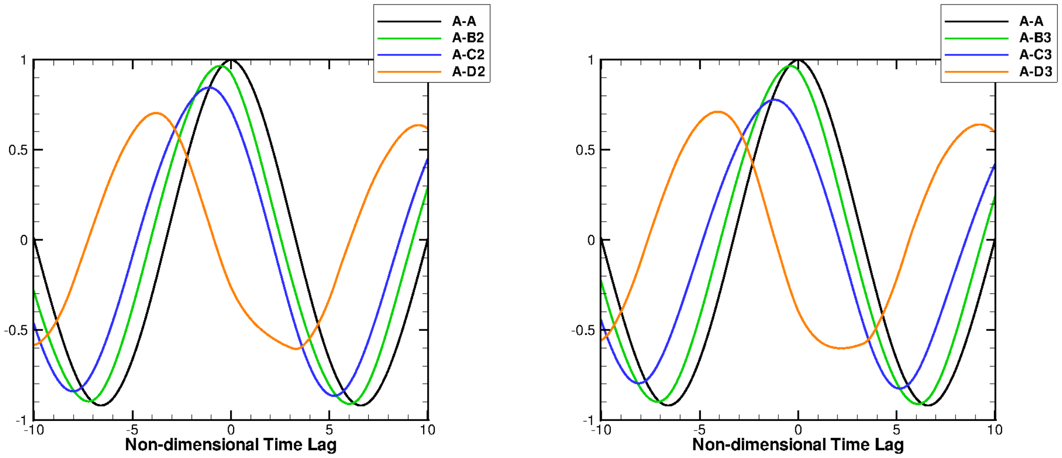

(c) Cross-covariance upstream path 2 (d) Cross-covariance upstream path 3

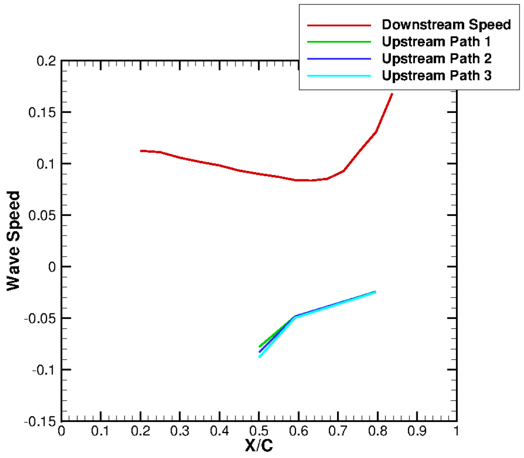

(e) Wave speeds

Figure 5.26: Cross-covariance and wave speed for angle of attack 6.97°

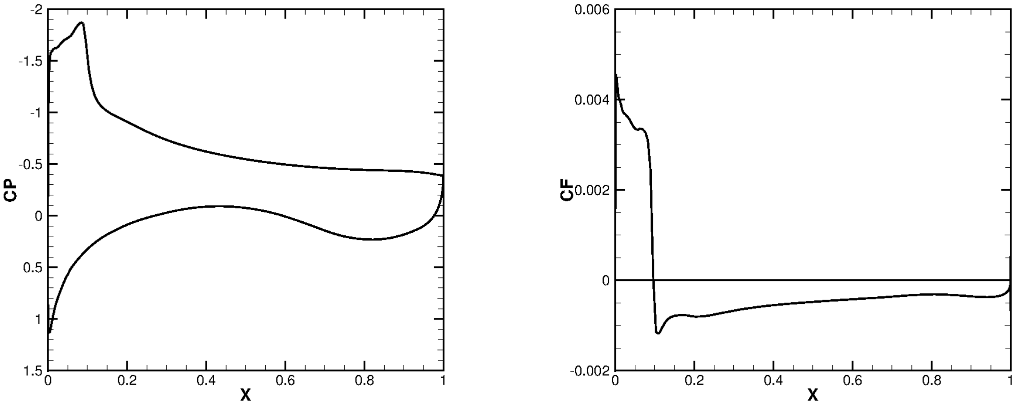

(a) Pressure distribution (b) Skin-friction distribution

Figure 5.27: BGK No. 1 angle of attack 9.0° results

Grid refinement, time step and pseudo step studies were completed with a time step of 120 steps per cycle using 1,000 pseudo steps on the medium grid proving to be adequate. The unsteady calculations gave more evidence of pressure waves travelling in the separated region and returning outside the separated region for the shock oscillation mechanism. This was achieved through the use of two point cross-covariances at various points in the flow field. The results obtained for the 4.905° angle of attack results showed reasonable agreement, but the results at 6.97° did not agree very well.

Chapter 6

Static Wing Aeroelasticity

6.1 Introduction

The aeroelastic research wing (ARW-2) was a full-scale right semispan wing, which was from part of the NASA Drones for Aerodynamic and Structural Testing (DAST) program [106]. The goals of DAST were to validate, 1) system synthesis and analysis developments for active control of aeroelastic response and 2) analysis techniques for aerodynamic loads prediction. The wing was designed for flight testing to investigate the use of active control systems to alleviate manoeuvre and gust loads as well as for flutter suppression. A series of windtunnel tests were carried out at NASA Langley Research Centre using the Langley Transonic Dynamics Tunnel (TDT) using heavy gas R-12 (also known as Dichlorodifluoromethane [107]) in the late 1980's and early 1990's. After the first set of tests were completed the planned flight test program was cancelled. As a result a second windtunnel test was performed to explore the region of large-amplitude response that had been uncovered by the first set of windtunnel tests.

The wing planform and dimensional data are presented in Figure 6.1 (a). The wing has an aspect ratio of 10.3 and a leading edge sweep angle of 28.8°. The wing was designed with supercritical aerofoil sections for a lift coefficient of 0.53 at Mach 0.8 with a cruise angle of attack of 1.53° at 46,800ft and dynamic pressure of 126.4psf. The wing has hydraulically driven trailing edge control surfaces, two inboard and one outboard, their locations are given in Figure 6.1 (b). For the windtunnel test the wing was instrumented with 182 pressure transducers, 10 accelerometers and strain gauges at the wing root to measure bending moments. The instrumentation locations are also shown in Figure 6.1 (b). The wing structure was designed iteratively taking into account the load and stiffness reduction benefits associated with the use of an active control system. This led to a more flexible wing than traditional designs. Due to this flexibility a jig shape was defined, which is the shape that the wing is manufactured to, so that at cruise the wing will deform into the desired aerodynamic shape. The first four modes in still air were first-bending (8.1Hz), second-bending (29.7Hz), in-plane (39.9Hz) and first-torsion (62.6Hz). The wing geometry is given in Sandford *et al.* [14] with the coordinates for the jig shape. This report also included data for the structural model that was generated with the mode shapes given on the upper surface of the wing.

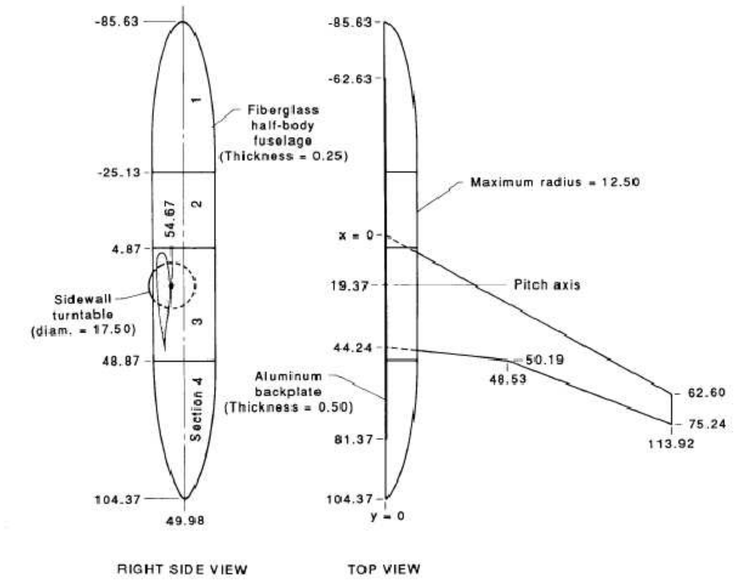

(a) Sketch of complete wind tunnel model (dimensions are in inches)

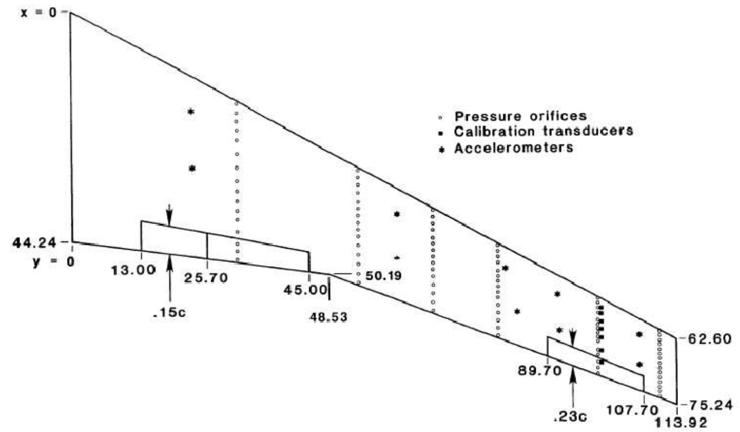

(b) Wing instrumentation (dimensions are in inches)

Figure 6.1: ARW-2 (from ref. [14])

The ARW-2 was found to have an instability in the Mach number range of 0.90 to 0.92 with a frequency that is very close to that of the first-bending mode. Buffet for the ARW-2 was found to be at its worst at Mach 0.92 with an angle of attack of -1° and a dynamic pressure of 325.6psf. At the test point the wing tip acceleration reached a peak of 32g. The remainder of the chapter discusses the previous work, the aerodynamic grid and structural model used in this work, followed by results of aeroelastic CFD calculations.

6.2 Previous Work

In 1987 Seidel *et al.* [108] presented experimental results from the first windtunnel test of the ARW-2 with the objective of providing an early assessment of the wing aeroelastic stability over a wide range of angles of attack. The experiment varied the Mach number between 0.6 to 0.9 at dynamic pressures of 50 to 300psf. The angle of attack was also varied in the range 0° to 2°. They found an unusual wing instability at a Mach number of 0.9 with a dynamic pressure of 100psf. Zero damping points where avoided to prevent damage to the wing, since it was expected to be flight tested. The instability had a frequency of 8.6Hz, which is very close to the first-bending mode frequency. The frequency of the instability was found to increase with dynamic pressure to 13Hz at the highest dynamic pressure tested and was found to be sensitive to angle of attack with minimum damping near zero degrees. A sustained limit amplitude oscillation at Mach 0.895 with the lowest dynamic pressure was discovered, however the wing became stable again at Mach 0.9.

Following the first windtunnel test the flight test program was cancelled, so a second windtunnel test was completed to firmly establish the existence of the instability that had been found and to gather data to help understand the mechanism forcing the wing oscillations. The results from this second test were published in a number of papers [23, 15, 109]. The second test did not find the instability predicted in the first windtunnel test, however a region of high dynamic wing response was found instead between Mach numbers 0.92 and 0.94. Eckstrom *et al.* [15] published a large amount of data from the second windtunnel test. This is a brief summary of the findings of the report. At Mach 0.80 there was little to no response, however there was a high frequency (40Hz) unsteady flow on the upper surface. At Mach 0.85 there was little response, but a strong shock was starting to form on the upper surface. There was also flow unsteadiness on both the upper and lower surfaces. At Mach 0.88 there was a moderate increase in motion for the medium dynamic pressure and a significant increase in motion for the high dynamic pressure. At this Mach number there was now a strong oscillating shock with a frequency of about 15Hz. At Mach 0.90 there was a significant increase in wing motion for all dynamic pressures. There was a strong shock on both the upper and lower surfaces and for some of the dynamic pressures the lower surface pressure was lower than the upper surface. This indicated that there was a strong upwards bending and, due to the wing sweep, a nose-down twist. There were also regions of separation on the lower surface. At Mach 0.92 the near maximum motion was achieved for all dynamic pressures and for the high dynamic pressure, at an angle of attack of -1°, wing-tip acceleration peaked at 32g. Some combinations of angle of attack and dynamic pressure were not tested due to concerns for the structural safety of the wing. There was a large region of separation on the lower surface and another region at the trailing edge of the upper surface. At Mach 0.94 there was a significant decrease in motion for the high dynamic pressure, whereas for the other dynamic pressures the motion remained at the same level. At Mach 0.96 for all dynamic pressures the wing motion decreased substantially. This is summarised in Figure 6.2, which shows the relative peak wing-tip response as the Mach number is increased. The mechanism for the response is related to the chordwise shock movement in conjunction with flow separation and reattachment on both the upper and lower surfaces of the wing. After a Mach number of 0.94 the wing response reduced, which was attributed to full flow separation downstream of the shockwaves with no reattachment. The wing-tip accelerometers show that the frequency of the response between 8 to 10Hz, which is near the first-bending mode. The amplitude of the dynamic wing response was found to increase with increasing dynamic pressure. It was also found to be angle of attack dependant with the maximum motion occurring near an angle of attack of zero degrees and as the angle of attack moved

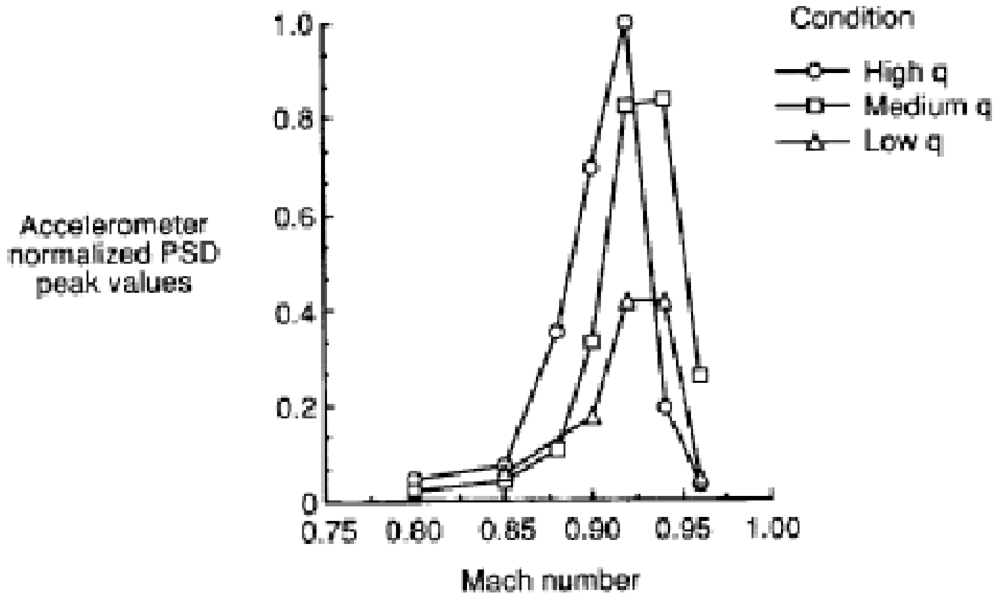

Figure 6.2: Maximum PSD peak response from front spar wing-tip accelerometer (from ref. [15])

from zero degrees, the maximum motion was shifted to Mach 0.94 at angles of attack of ±2°. Seidel *et al.* [23] tested two methods to reduce the buffet, the first was a mean control surface deflection of $-6°$ and the second was a lower surface spanwise fence. Both methods were found to significantly reduce the maximum wing response and reduce the Mach number of the peak wing response slightly.

In 1996 Farhangnia *et al.* [110] published CFD results and compared them with the experimental data. The calculations were done using ENSAERO which used the strong conservation-law form of the thin-layer Reynolds-averaged Navier-Stokes equations with the Baldwin-Lomax turbulence model and a modal approach for the structural solver. Pressure coefficient comparisons were presented for rigid, static and dynamic cases. An improvement in the results was shown as the aeroelasticity was taken into account. This paper says that the structural response is due to the upper shock oscillation.

6.3 Test Case Setup

6.3.1 CFD Grid

The geometry was built from the design coordinates from Sandford *et al.* [14] and a C-H type blocking was used to block the wing. The grid size is 2,333,940 nodes and is shown in Figure 6.3.

6.3.2 Structural Model

The structure and the mode shapes are given in Sandford *et al.* [14] in the form of coordinates and displacements at 100 points on the upper surface of their finite element model. A shell model (referred to as the shell model) was generated to replicate the shell model presented in Sandford *et al.* [14] (referred to as the report model). The resulting model is compared with the model [14] in both frequencies and mode shapes, with the frequencies given in Table 6.1.

Table 6.1: Comparison of the structural model frequencies

Mode	Model [14] (Hz)	Shell Model (Hz)
1	8.0935	8.0272
2	29.2299	29.0527
3	32.7980	32.6560
4	60.8920	61.4565

The frequencies are all within 1% of the model [14]. The mode shape comparison of the upper surfaces is shown in Figure 6.4. It can be seen that the shell

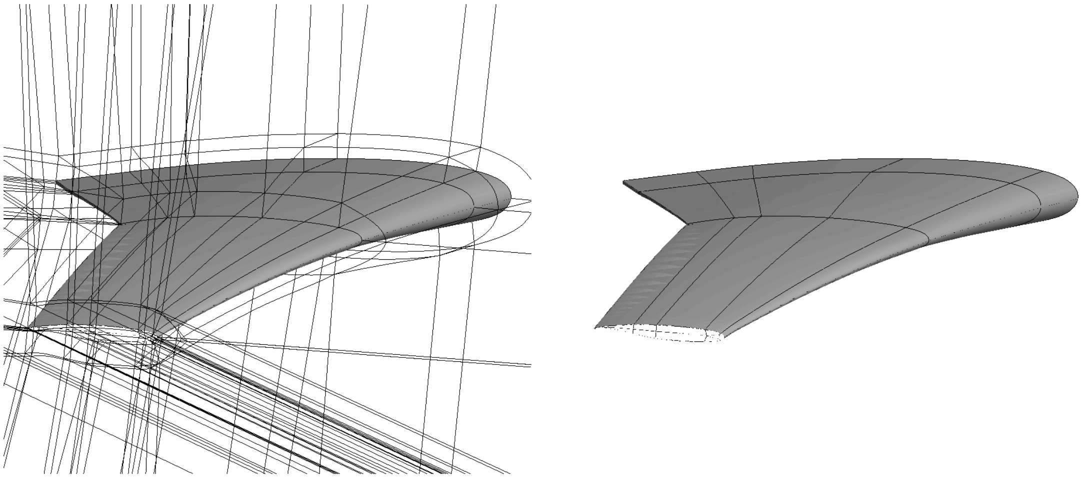

(a) Near wing blocking (b) Surface blocking

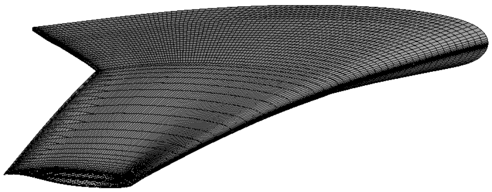

(c) Surface grid

Figure 6.3: ARW-2 grid details

model mode 4 has less torsion compared to the report model, however all the other modes are captured well.

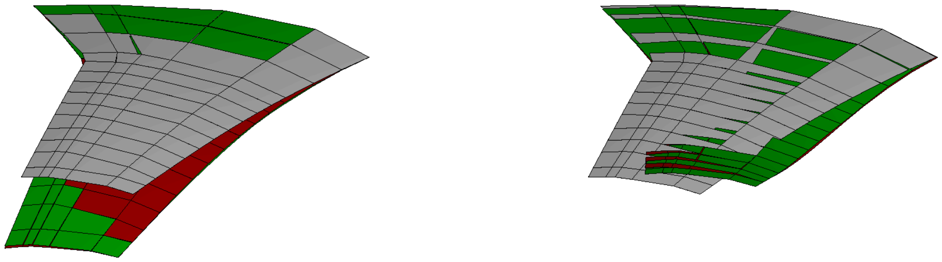

(a) Mode 1

(b) Mode 2

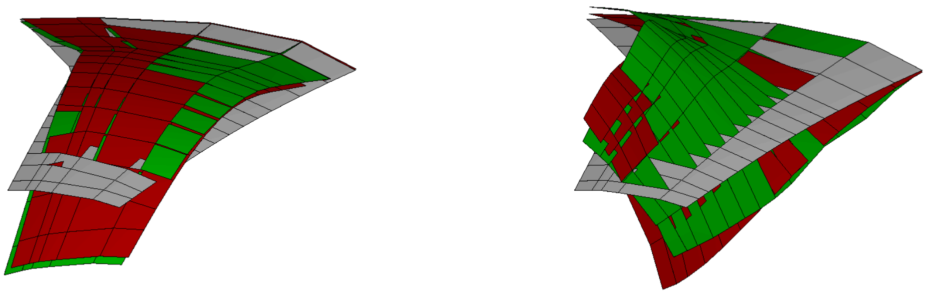

(c) Mode 3

(d) Mode 4

Figure 6.4: Comparison of the mode shapes. Grey - Undeformed shell model, Red - Report model mode shapes, Green - Shell model mode shapes

The shell model was converted into a beam model using the leading and trailing edge deflections. The mode shapes are almost exactly the same as the original data, except for the torsion mode. The torsion mode from the shell model has the section stretching which cannot be recreated using a beam model, however the wing is unlikely to stretch to the degree of the shell model, so this is believed to be an artifact of the finite element model that is presented in the reference and recreated by the shell model. This is backed up by the paper by Byrdsong *et al.* [111] that states that there was sufficient chordwise rigidity to prevent chordwise bending. The beam model along with a rigid direction that is parallel with the majority of the ribs was used to generate the mode shapes on the aerodynamic surface using the method discussed in Chapter 3. The mode shapes defined on the surface mesh are shown in Figure 6.5.

(a) Mode 1

(b) Mode 2

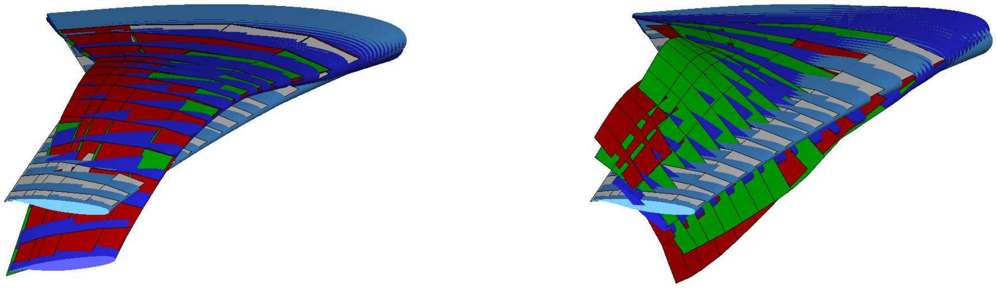

(c) Mode 3

(d) Mode 4

Figure 6.5: Comparison of the mode shapes with the beam model. Grey - Undeformed shell model, Red - Report model mode shapes, Green - Shell model mode shapes, Pale Blue - Undeformed CFD mesh, Blue - Beam model mode shapes on the CFD mesh

6.4 Results

A number of static calculations were performed to compare the aerodynamics and the static deflections. The flow conditions for the test cases are given in Table 6.2. The Reynolds number is based upon the mean aerodynamic chord. Each calculation was run for 500 explicit steps at a CFL of 0.4 followed by 40,000 implicit steps at a CFL of 2.0. The desired convergence is set to 1×10^{-5} using the SST turbulence model. Since the windtunnel data was collected using heavy gas R-12, the ratio of specific heats γ was set to 1.14 as per the data given in Cole and Rivera [107].

Table 6.2: ARW-2 test conditions

Case	Mach number	Angle of attack	Reynolds number	Dynamic pressure	Eckstrom *et al.* [15] tab	Byrdsong *et al.* [111, 112] tab
1	0.80	0.0°	2.41×10^6	123.6psf	91	82
2	0.85	1.0°	2.41×10^6	134.6psf	243	914
3	0.92	0.0°	2.60×10^6	152.5psf	98	-
4	0.92	2.0°	2.60×10^6	154.8psf	111	-

6.4.1 Case 1: Mach Number 0.80, Angle of Attack 0.0°

The experiments by Eckstrom *et al.* [15] showed that this test condition was free from buffet and there is experimental data for the static deflections from Byrdsong *et al.* [111, 112]. Byrdsong *et al.* did not record any results if the deflections were not static or quasi-static, implying that this test condition is static.

The pressure distributions are shown in Figure 6.6 for both the static and rigid cases. The effect of not taking the structural flexibility into account is considerable with a strong shockwave generated in the outboard sections. By taking into account the structural flexibility the pressure distributions match the experimental data better. The noticeable discrepancy is a large suction peak in the static results that are not shown in the experimental results. This improvement appears to be due a nose-down twist, however the lower surface is not matched as well as expected. This is likely to be due to an insufficient amount of twist being generated.

The Mach number contours for the rigid and static solutions are shown in Figure 6.7 side by side. The sections at 10% span are very similar, since the effect of the static deflections will have a minimal effect so close to the root of the wing. The section at 56% span has the static effects starting to show as the static section has risen slightly. There are also small differences appearing in the Mach contours. At 80% span the deflection of the static section is more pronounced and the shockwave seen in the rigid section has weakened significantly and shifted to the leading edge in the static solution. Finally in the 95% sections, again there is significant deflection in the static case. The Mach contours have a strong shock in the rigid case that has shifted forwards to the leading edge and weakens considerably in the static case. This implies that the large suction peak is possibly a weak shockwave.

The streamlines are shown in Figure 6.8 for both the rigid and static cases. For both the rigid and static cases, the flow over the entire span is attached. This is backed up by the experimental observations by Eckstrom *et al.* [15].

Figure 6.9 shows the 3D representation of the wing in its rigid and deflected states. The plots showing the front and rear spar deflections show a very good match with the experimental data of Byrdsong *et al.* [111, 112]. The twist angle is shown in Figure 6.10 along with the change in twist between the rigid and static cases. Although the deflections match the experimental values well, the twist does not match as well. The change in twist for the CFD follows a different profile to the experimental result as seen in Figure 6.10(b). This observation matches with the pressure distribution results, which appears to have insufficient nose down twist. This could be due to the errors introduced due to the modelling of the structure, both by Sandford *et al.* [14] and subsequently by the author. In the paper by Sandford *et al.* the frequencies of the structural model did not match those obtained by the experiment exactly. Then the shell model generated by the author was within 1% of the Sandford *et al.* model and mode 4 did not recreate the same level of twist as the Sandford *et al.* model. This could be the reason for the lack of agreement for the twist.

6.4.2 Case 2: Mach Number 0.85, Angle of Attack $1.0°$

The experimental results of Eckstrom *et al.* [15] report no large scale motion at these test conditions. There are also static deflection results available from Byrdsong *et al.* [111, 112], implying it is a static case.

The sectional results are shown in Figure 6.11. As seen before the rigid results produce a strong shockwave and much higher pre-shock levels. The static results are a significant improvement over the rigid results and match the experimental results well. Again this improvement is indicative of a nose-down twist.

The Mach number contours are shown in Figure 6.12 and a strong shockwave can be seen to have formed on the upper surface throughout the entire span for both rigid and static cases. However the shock weakens as the tip is approached for the static case, due to the deflection of the wing and the slight nose down twist.

The streamline plots are given in Figure 6.13. The rigid case does have regions of separated flow caused by the shock wave especially at the midspan. The static case shows no regions of separation for any spanwise station. The experiments by Eckstrom *et al.* [15] did not report any regions of separated flow, but did comment that there were regions of unsteady flow on both the upper and lower surfaces. It is not known whether this unsteadiness is due to shock oscillation or separated flow.

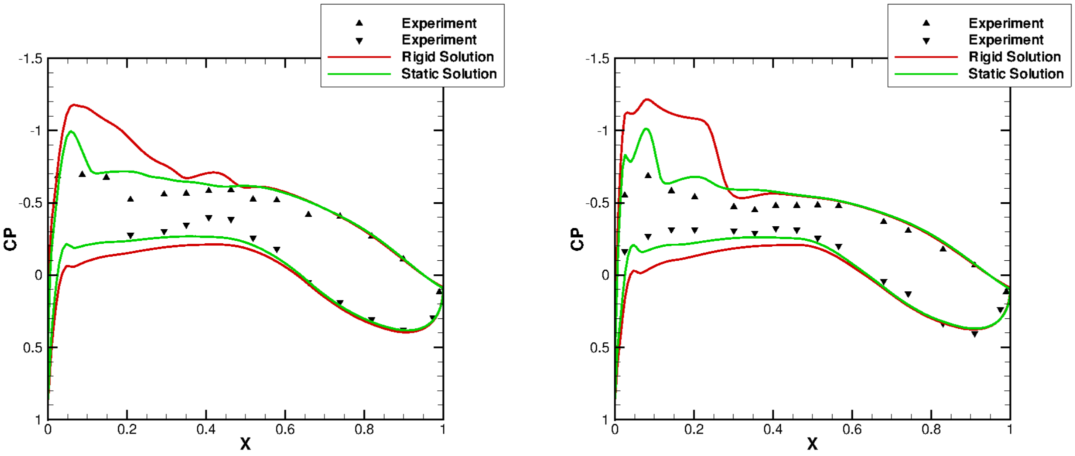

(a) 70.7% Section pressure distribution

(b) 87.1% Section pressure distribution

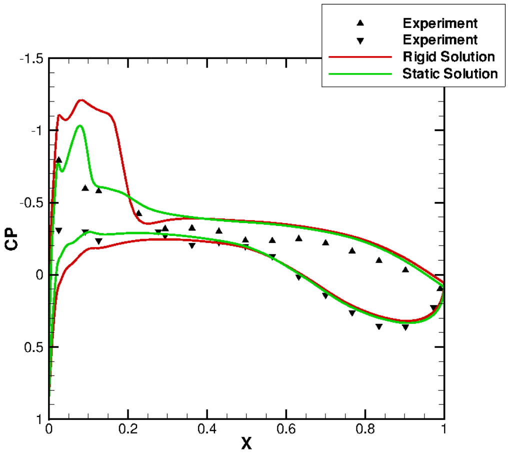

(c) 97.2% Section pressure distribution

Figure 6.6: Case 1: Sectional results

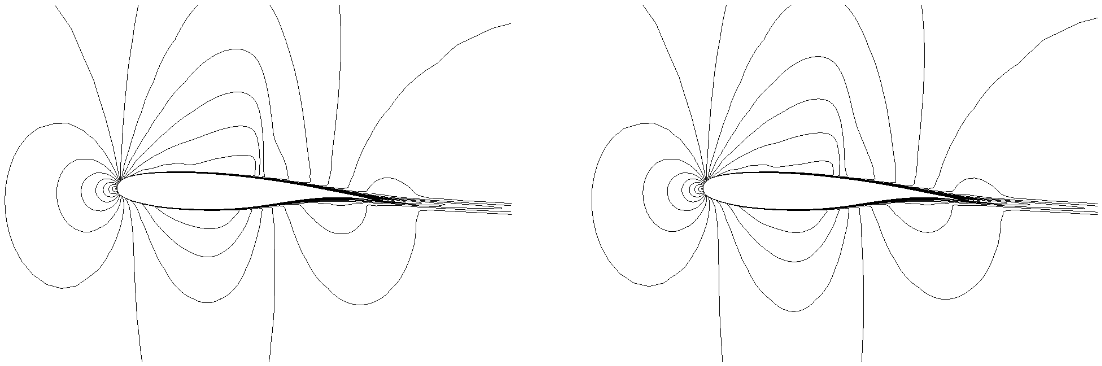

(a) 10% Section rigid solution (b) 10% Section static solution

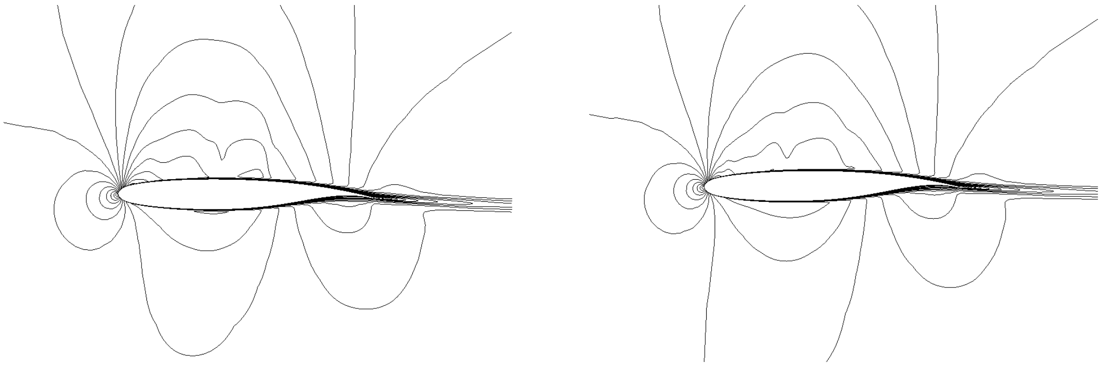

(c) 56% Section rigid solution (d) 56% Section static solution

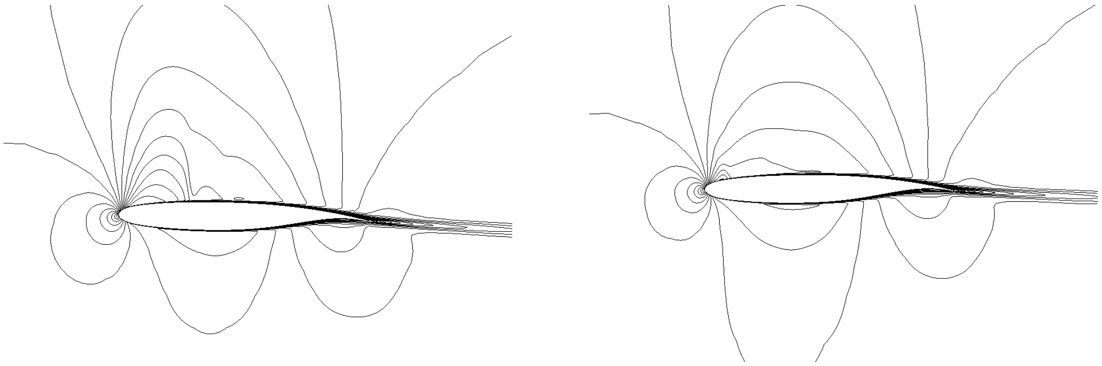

(e) 80% Section rigid solution (f) 80% Section static solution

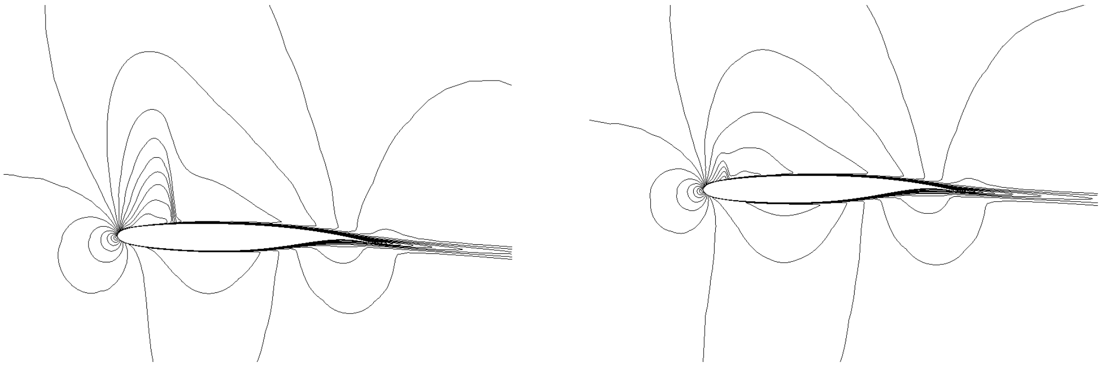

(g) 95% Section rigid solution (h) 95% Section static solution

Figure 6.7: Case 1: Mach number contours, $\Delta M = 0.045$

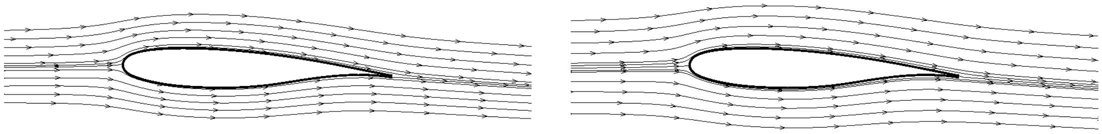

(a) 10% Section rigid solution

(b) 10% Section static solution

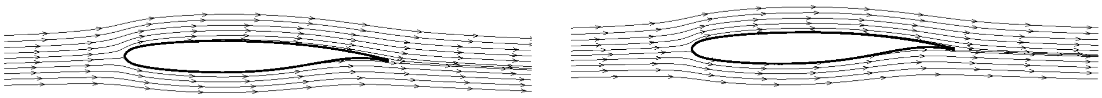

(c) 56% Section rigid solution

(d) 56% Section static solution

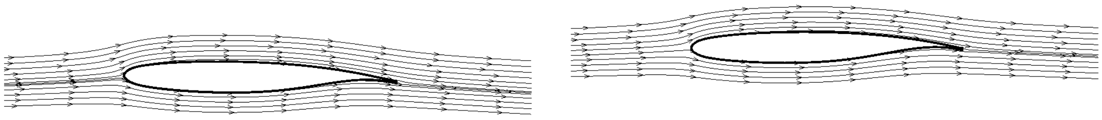

(e) 80% Section rigid solution

(f) 80% Section static solution

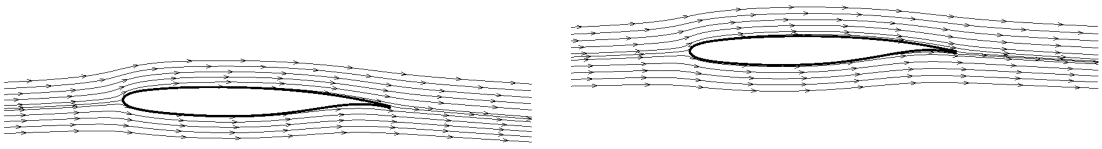

(g) 95% Section rigid solution

(h) 95% Section static solution

Figure 6.8: Case 1: Streamlines

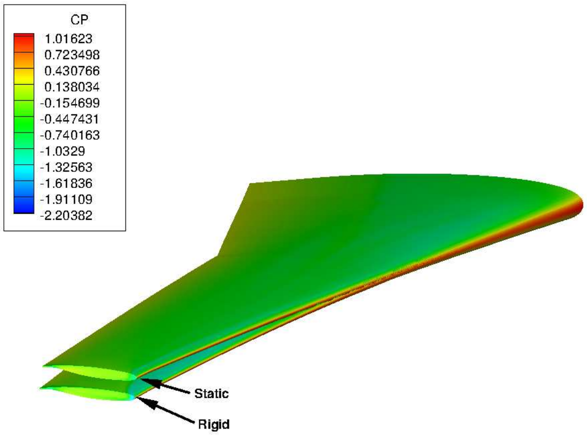

(a) Wing deflection comparison

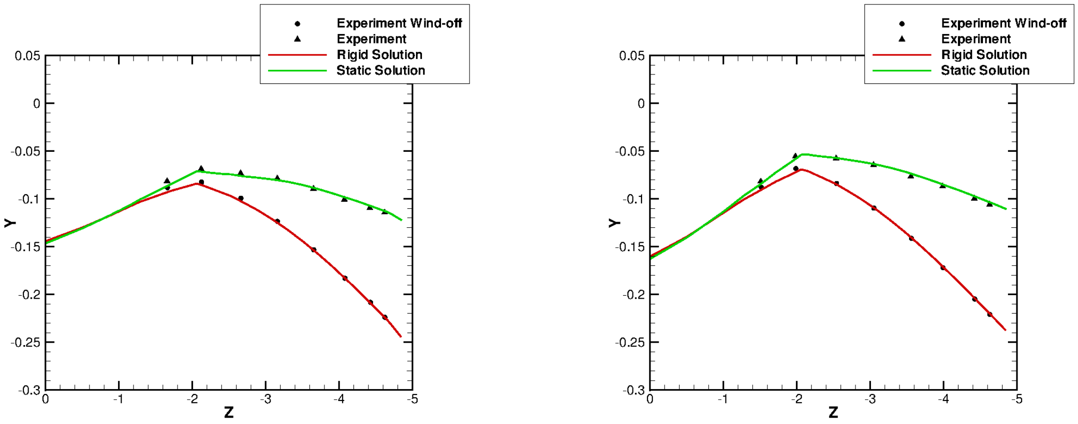

(b) Front spar

(c) Rear spar

Figure 6.9: Case 1: Spar deflections

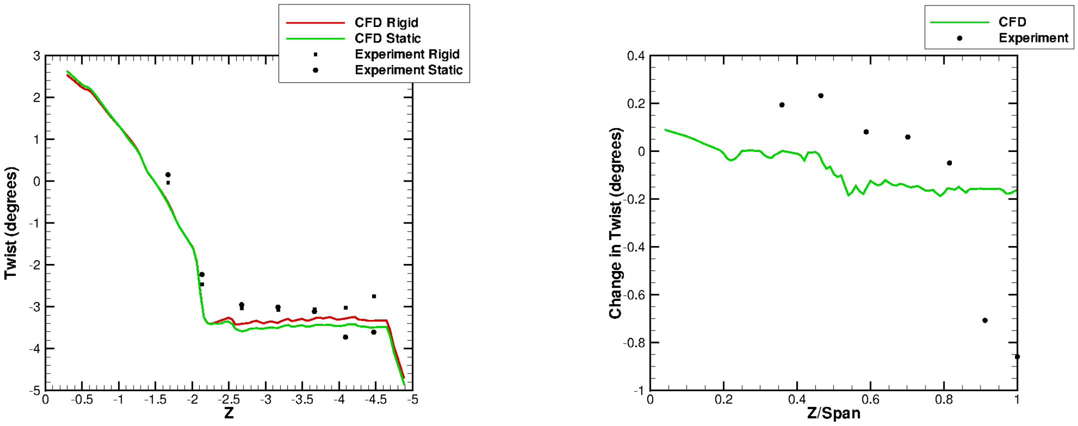

(a) Twist

(b) Change in twist between rigid and static cases

Figure 6.10: Case 1: Wing twist

The spar deflections in Figure 6.14 do not match the experimental data of Byrdsong *et al.* [111, 112] as well as the previous case. This is mainly due to the dynamic pressure used that matches the experimental data by Eckstrom *et al.* [15], but is about halfway between two of the dynamic pressures used to record the static deflections by Byrdsong *et al.*. As such it would be expected that the static deflections do not match.

The twist results are shown in Figure 6.15 again showing a discrepancy between the CFD and the experimental results. This will be due to the dynamic pressure used and the failure of the structural model to fully capture the amount of twist in mode 4.

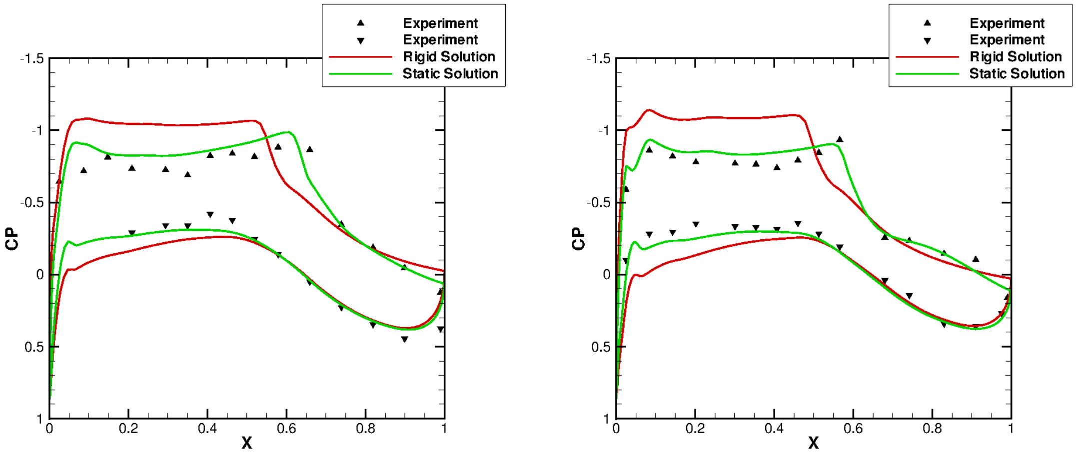

(a) 70.7% Section pressure distribution

(b) 87.1% Section pressure distribution

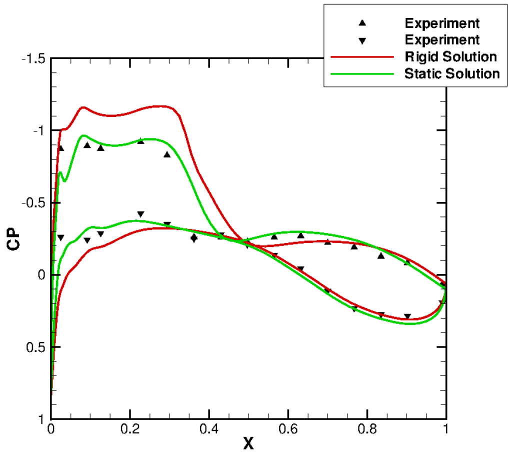

(c) 97.2% Section pressure distribution

Figure 6.11: Case 2: Sectional results

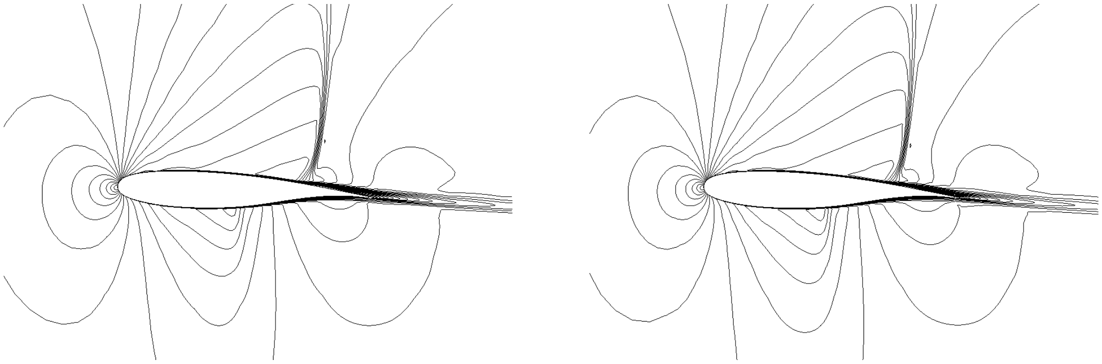

(a) 10% Section rigid solution (b) 10% Section static solution

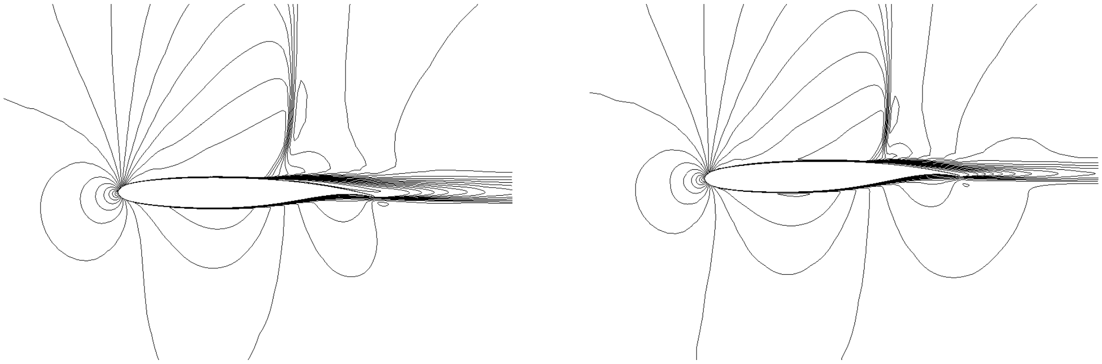

(c) 56% Section rigid solution (d) 56% Section static solution

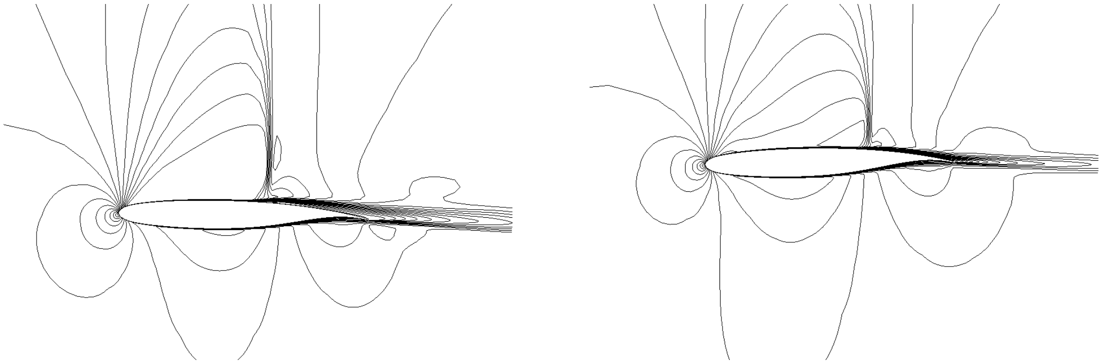

(e) 80% Section rigid solution (f) 80% Section static solution

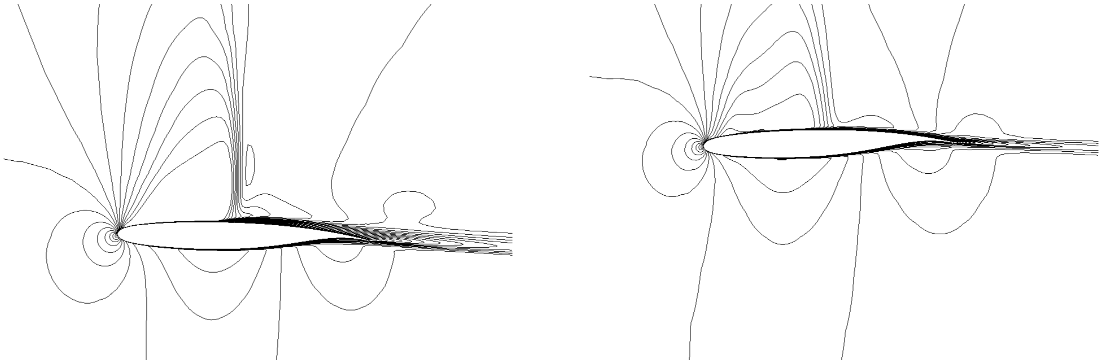

(g) 95% Section rigid solution (h) 95% Section static solution

Figure 6.12: Case 2: Mach number contours, $\Delta M = 0.045$

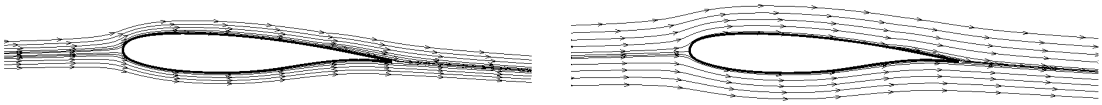

(a) 10% Section rigid solution (b) 10% Section static solution

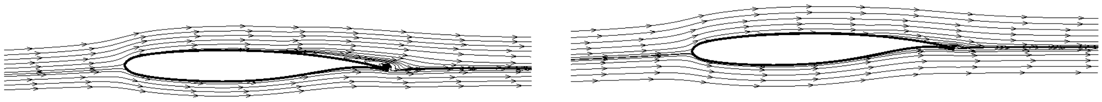

(c) 56% Section rigid solution (d) 56% Section static solution

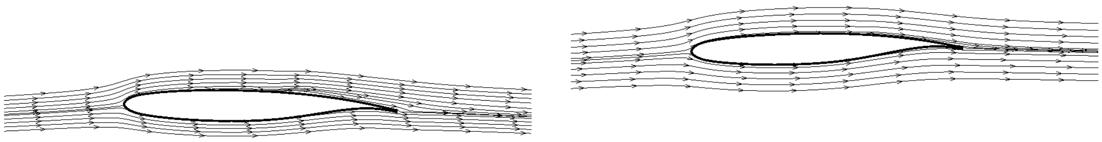

(e) 80% Section rigid solution (f) 80% Section static solution

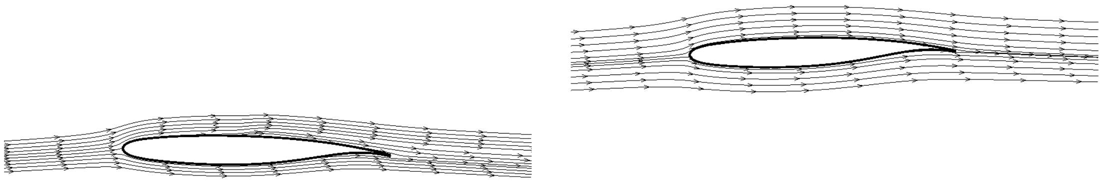

(g) 95% Section rigid solution (h) 95% Section static solution

Figure 6.13: Case 2: Streamlines

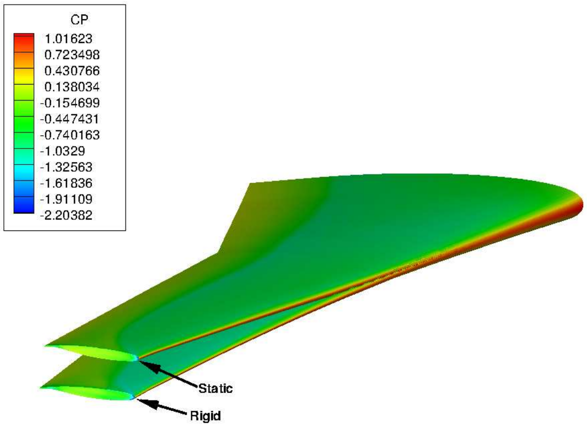

(a) Wing deflection

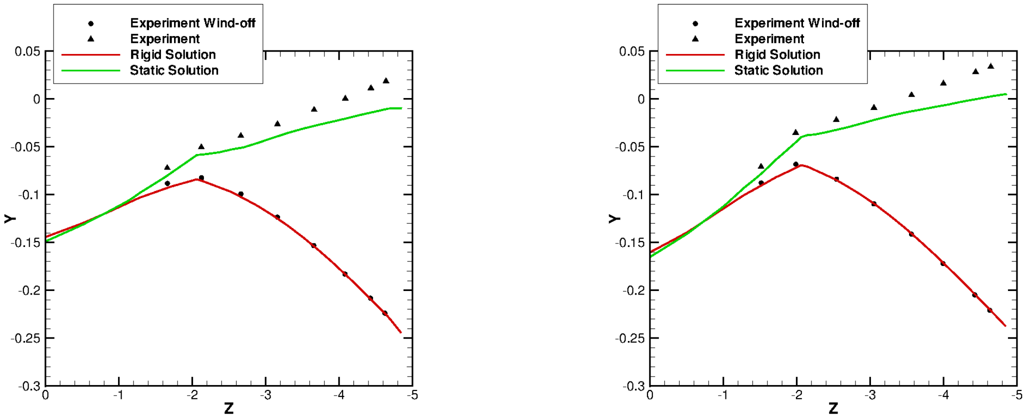

(b) Front spar

(c) Rear spar

Figure 6.14: Case 2: Spar deflections

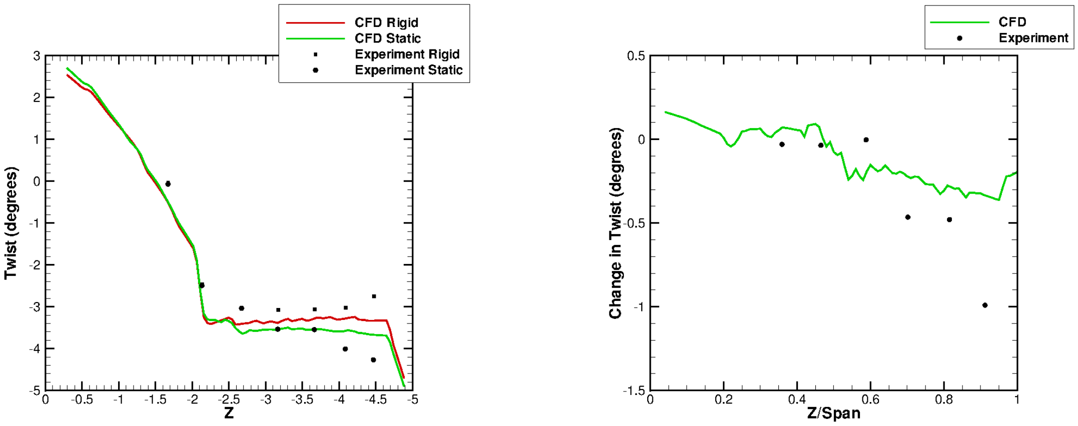

(a) Twist

(b) Change in twist between rigid and static cases

Figure 6.15: Case 2: Wing twist

6.4.3 Case 3: Mach Number 0.92, Angle of Attack 0.0°

This case did not produce static deflections in the experiments and had near maximum dynamic wingtip motions [15]. As such there are no static results to compare against by Byrdsong *et al.* [111, 112], since they did not record any dynamic deflections. The static calculation lift and residual histories are shown in Figure 6.16. These show that the calculation has not converged to a steady solution and is therefore is likely to be an unsteady case. The lift history shows oscillations that indicate a possible shock-oscillation.

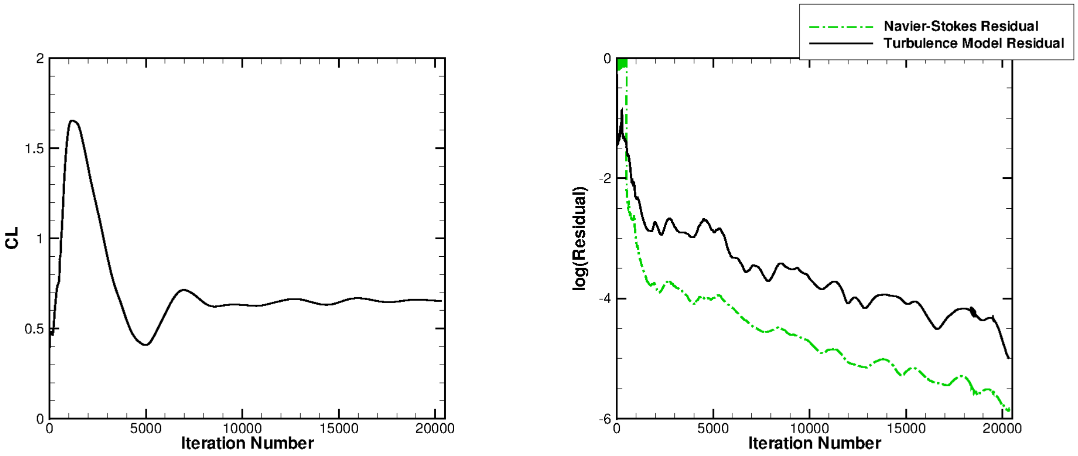

(a) Lift History (b) Residual History

Figure 6.16: Case 3: Convergence

6.4.4 Case 4: Mach Number 0.92, Angle of Attack 2.0°

This case like the last also has large dynamic wingtip motion in the experiment [15] and therefore has no static deflection results to compare with from Byrdsong *et al.* [111, 112]. This experimental observation is backed up by the calculation lift and residual histories in Figure 6.17. The lift history has an oscillation, which indicates a possible shock-oscillation. The residual history shows that the static calculation converges to about -4 and then converges no further, which also indicates that this case is unsteady.

6.4.5 Buffet Search

A similar search to the one performed for the BGK number one aerofoil was performed for the ARW-2 to find the most likely buffet cases using steady static calculations. The calculations were performed at angle of attack 0.0°, Reynolds number 2.5×10^6, dynamic pressure 150 psf and the Mach number was varied

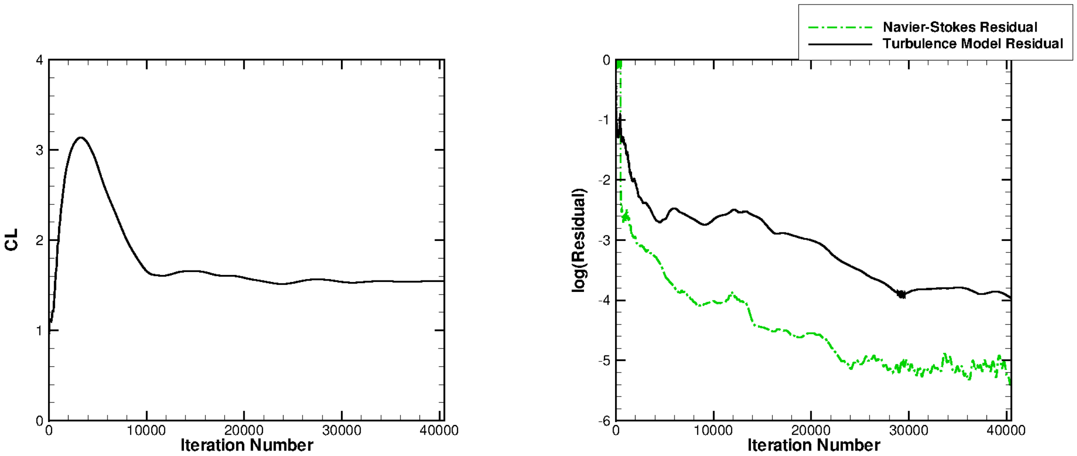

(a) Lift History

(b) Residual History

Figure 6.17: Case 4: Convergence

between 0.80 and 0.94. The results are shown in Figure 6.18. Mach 0.85 has a sudden jump due to the calculation being restarted, but it otherwise converged well. However if that case did not require restarting it is likely it would have converged before the Mach 0.88 case. The time history for the lift shows little variation unlike the BGK No. 1 aerofoil. However of the unsteady cases tested in the BGK No. 1 aerofoil case, one was obviously unsteady and the other was a more subtle case in the buffet search. As such the most likely candidates for unsteady cases are Mach 0.92 and Mach 0.94, since Mach 0.94 did not converge and Mach 0.92 converged much slower than the lower Mach numbers and the lift history shows oscillations.

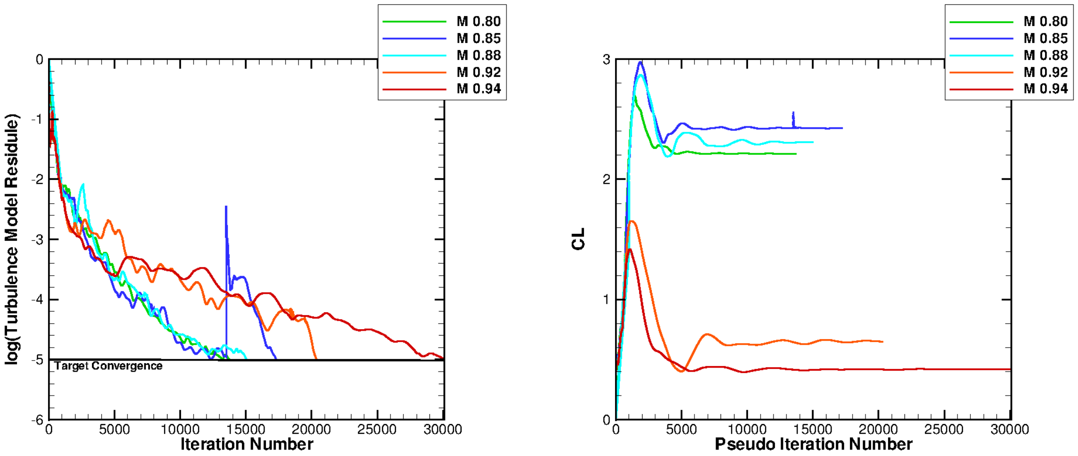

(a) Convergence history

(b) Lift history

Figure 6.18: Buffet search results

6.5 Summary

It was shown that for the static case the AMB solver matched the experiments well. However when the flow conditions where expected to lead to an unsteady result the solver was unable to match the experiment using steady static calculations. This is unsurprising and can be rectified by running computationally expensive unsteady calculations in the future. A buffet search was completed to find the most promising case for buffet calculations, leading to Mach 0.92 and 0.94 being the most likely candidates. Cases 3 and 4 are also promising candidates for buffet calculations as these also failed to converge and hint at shock-oscillation. Although all the preparation was completed for buffet calculations on the ARW wing, the actual unsteady calculation was not ran. This was because the calculation was unable to be ran in a reasonable time period on the computational resources available. To run this calculation in a reasonable time period more computational nodes are required and the grid needs to be split into more domains to allow it to be well load balanced on the increased number of nodes.

Chapter 7

Conclusions

7.1 Conclusions

The objective of this work was to investigate the influence of transformation methods on the flutter boundary and to consider the simulation of shock-induced buffet of a transport wing.

The formulation of the CFD, structural and Schur solvers was presented in Chapter 2.

The transformation problem was presented in Chapter 3, along with the different types of structural models and a number of transformation methods. A new method based on an assumption of beam stick models that the section perpendicular to the beam is rigid was presented. In this method the direction that is assumed to be rigid is defined. These rigid ribs should ideally be the same direction as the wing ribs and perpendicular to the beam, but can be varied to assess the effect of the transformation scheme on the predictions.

The transfer methods IPS, IIM, CVT and RBF were tested on the Goland and MDO wings in Chapter 4. Through the use of different structural models it was found that the in-plane component of a transformation method dominated the calculated displacements. It was also shown that the transformation methods are sensitive to the structural grid density, with only IIM relatively unaffected. The local method CVT suffers from discontinuities in slope at the structural element edges, due to the formulation only being C^0 continuous. The other local method tested, IIM, is also only C^0 continuous, but did not show any significant discontinuities. This is probably due to the higher order interpolation used. Both global methods tested suffered due to the coarse grids used and tended to introduce oscillations to the section shape. Another important consideration is to avoid transformation methods extrapolating, and wherever possible to do the extrapolation as a pre-processing step. This can be achieved in NASTRAN through the use of rigid bars (RBAR). A method was proposed for extrapolating beam stick models by specifying a direction for extrapolation and it was shown to perform as well as IIM. It was also shown that when the rigid direction was not close to perpendicular to the beam, the section shapes were worse.

The effect of the transformation methods on the flutter boundary of the Goland and MDO wings was also investigated in Chapter 4. It was shown that the local methods had less spread in their prediction of the flutter point as the structural model was varied than the global methods. More importantly there was more spread in the flutter point when the transformation methods extrapolated. This adds weight to the previous conclusion that the transfer methods should not extrapolate and that extrapolation should be done as a pre-processing step. It is important to stick to the structural model assumptions and extrapolate perpendicular to the beam, as this was shown to reduce the spread in the predicted flutter point. Since it was shown that the choice of transfer method can have a significant effect on the predicted flutter point, it is therefore advisable to use multiple transfer methods to build confidence in the results obtained.

To facilitate buffet calculations the AMB solver was verified for shock-induced buffet. This was completed using the BGK No. 1 aerofoil and a number of convergence studies in Chapter 5. A buffet search using steady state calculations was performed to estimate the buffet boundary. Two methods were used, the first was to use the lift history and the second was to use the calculation residual. The lift history method matched the experimental shock oscillation region very well, but performed less well against the experimental buffet onset. The residual method performed better at predicting buffet onset, but predicted a slightly larger region than the experiment. This did provide evidence that steady state calculations could be used to predict shock-oscillation cases and potentially buffet onset boundary. A number of unsteady calculations were used to check the results of the steady state predictions and covered the pre, post and shock-oscillation regimes. The results from these calculations matched the steady state predictions and the experimental data. For the two cases that proved to be unsteady, the mechanism behind the shock-oscillation was investigated. Through the use of cross-covariance and probes inside and outside the boundary-layer, pressure waves could be detected travelling downstream inside the boundary-layer and upstream outside the boundary-layer. The time lags of these pressure waves could be calculated and they correlated to the shock-oscillation period for the 4.905° angle of attack case.

Finally the static aeroelasticity of the ARW-2 wing was calculated to verify the AMB solver for static aeroelasticity in Chapter 6. For cases that had been shown to be static experimentally the solver produced good results providing reasonable agreement with experimental pressure distributions and wing deflections.

The results did not match as well as expected for wing twist, this is thought to be due to the structural model failing to capture the torsion mode well. The experimentally unsteady cases failed to converge when computed using steady state calculations. This led to a similar buffet search to the BGK No. 1 aerofoil, which predicted the Mach numbers 0.92 and 0.94 as the most likely candidates for unsteady cases for an angle of attack of zero degrees, Reynolds number 2.5×10^6 and dynamic pressure 150psf. This was consistent with the experimental data.

7.2 Future Work

Buffet calculations can now be performed on the ARW-2 wing. This would be a combination of the experience gained from the 2D aerofoil buffet calculations and the static aeroelastic work already preformed on the ARW-2 wing. It has already been commented that the literature indicates the buffet is due to shock-oscillation on the upper surface, but the mechanism behind it has not been studied. As such it would be interesting to investigate the buffet mechanism on the wing and see if it is the same as the aerofoil case with propagating pressure waves.

There has been a lot of work in recent years on the RBF transfer method for aeroelasticity and grid deformation. The most interesting development is the pointwise partition of unity and has been shown to localise the method. It would be an interesting extension of the current work to see how this would effect the extrapolation characteristics of RBF and if it prevents the oscillation in the section shapes that were be generated. The effect of the pointwise partition of unity on flutter prediction variability would also be an interesting study.

Although the rigid ribs transformation model was useful in testing how varying the direction of the ribs affects the flutter prediction, it requires extending for use with more complex geometries. This can be achieved in a similar way to that used for CVT, by using a hierarchy of components and blending functions.

An extension of the aerofoil buffet work would be to model the turbulence using DES or LES to investigate whether significant improvements could be made by using these more expensive options over URANS.

Bibliography

[1] Spalart P.R. Strategies for Turbulence Modelling and Simulations. *International Journal of Heat and Fluid Flow*, 21:252–263, 2000.

[2] Rendall T.C.S. and Allen C.B. Unified Fluid-Structure Interpolation and Mesh Motion using Radial Basis Functions. *International Journal for Numerical Methods in Engineering*, 74:1519–1559, 2008.

[3] Xiao Q., Tsai H.M., and Liu F. Numerical Study of Transonic Buffet on a Supercritical Airfoil. *AIAA Journal*, 44(3):620–628, March 2006.

[4] Canfield R.A., Morgenstern S.D., and Kunz D.L. Alleviation of Buffet-Induced Vibration using Piezoelectric Actuators. *Computers and Structures*, 86:281–291, 2008.

[5] NASA. Website, 1989. `http://www.dfrc.nasa.gov/Gallery/Photo/F-18HARV/HTML/EC89-`

[6] ESDU International plc. An Introduction to Aircraft Buffet and Buffeting. Technical Report 87012, ESDU International plc, 2006.

[7] Woodgate M.A., Badcock K.J., Rampurawala A.M., Richards B.E., Nardini D., and Henshaw M.J. de C. Aeroelastic Calculations for the Hawk Aircraft using the Euler Equations. *Journal of Aircraft*, 42(4):1005–1012, 2005.

[8] Fukushima C. and Westerweel J. Website, 2007. `http://en.wikipedia.org/wiki/File:Jet.jpg`.

[9] Wilcox D.C. *Turbulence Modelling for CFD*. DCW Industries, Inc., 3 edition, 2006.

[10] Rampurawala A.M. *Aeroelastic Analysis of Aircraft with Control Surfaces using CFD*. PhD thesis, University of Glasgow, 2006.

[11] Samareh J.A. and Bhatia K.G. A Unified Approach to Modelling Multidisciplinary Interactions. *AIAA Paper AIAA-2000-4704*, 2000.

[12] Lee B.H.K. Oscillatory Shock Motion Caused by Transonic Shock Boundary-Layer Interaction. *AIAA Journal*, 28(5):942–944, 1990.

[13] McDevitt J.B., Levy Jr. L.L., and Deiwert G.S. Transonic flow about a thick circular-arc airfoil. *AIAA Journal*, 14(5):606–613, 1976.

[14] Sandford M.C., Seidel D.A., and Spain C.V. Geometrical and structural properties of an aeroelastic research wing. Technical Report NASA TM 4110, NASA, Langley Research Center, Hampton, Virginia, 1989.

[15] Eckstrom C.V., Seidel D.A., and Sandford M.C. Measurements of unsteady pressure and structural response for an elastic supercritical wing. Technical Report NASA TP 3443, NASA, Langley Research Center, Hampton, Virginia, November 1994.

[16] Garrick I.E. and Reed III W.H. Historical Development of Aircraft Flutter. *Journal of Aircraft*, 18(11):897–912, 1981.

[17] Collar A.R. The First Fifty Years of Aeroelasticity. *Aerospace*, 5(2):12–20, February 1978.

[18] Wright J.R. and Cooper J.E. *Introduction to Aircraft Aeroelasticity and Loads*. Wiley, 2007.

[19] Walters J.M. and Sumwalt III R.L. *Aircraft Accident Analysis: Final Reports*. McGraw-Hill, 2000.

[20] Bunton R.W. and Denegri Jr. C.M. Limit Cycle Oscillation Characteristics of Fighter Aircraft. *Journal of Aircraft*, 37(5):916–918, 2000.

[21] Fung Y.C. *An Introduction to the Theory of Aeroelasticity*. Dover Publications Inc., 2002.

[22] Triplett W.E. Pressure Measurements in Twin Vertical Tails in Buffeting Flow. *Journal of Aircraft*, 20(11):920–925, 1983.

[23] Seidel D.A., Eckstrom C.V., and Sandford M.C. Transonic Region of High Dynamic Response Encountered on an Elastic Supercritical Wing. *Journal of Aircraft*, 26(9):870–875, 1989.

[24] Sheta EF. Alleviation of vertical tail buffeting of f/a-18 aircraft. *Journal of Aircraft*, 42(2):322–330, 2004.

[25] Wickramasinghe V.K., Chen Y., and Zimcik D.G. Experimental Evaluation of an Advanced Buffet System on Full-Scale F/A-18 Fin. *Journal of Aircraft*, 44(3):733–740, 2007.

[26] Breitsamter C. and Laschka B. Fin Buffet Pressure Evaluation Based on Measured Flowfield Velocities. *Journal of Aircraft*, 35(5):806–808, 1998.

[27] Breitsamter C. and Schmid A. Airbrake-Induced Fin-Buffet Loads on Fighter Aircraft. *Journal of Aircraft*, 45(5):1619–1630, 2008.

[28] Moses R.W. and Huttsell L. Fin Buffeting Features of an Early F-22 Model. *AIAA Paper AIAA 200-1695*, 2000.

[29] Anderson W.D., Patel S.R., and Black C.L. Low-Speed Wind Tunnel Buffet Testing on the F-22. *Journal of Aircraft*, 43(4):879–885, 2006.

[30] Pototzky A.S. and Moses R.W. A Tail Buffet Loads Prediction Method for Aircraft at High Angles of Attack. Technical Report 20050217424, NASA Langley Research Center, 2005.

[31] ESDU International plc. Fluctuating Loads and Dynamic Response of Bodies and Structures in Fluid Flows - Background Information. Technical Report 77032, ESDU International plc, 2007.

[32] Henshaw M.J de C., Badcock K.J, Vio G.A., Allen C.B., Chamberlain J., Kaynes I., Dimitriadis G., Cooper J.E., Woodgate M.A., Rampurawala A.M., Jones D., Fenwick C., Gaitonde A.L., Taylor N.V., Amor D.S., Eccles T.A., and Denley C.J. Nonlinear aeroelastic prediction for aircraft applications. *Progress in Aerospace Sciences*, 43:65–137, 2007.

[33] Bhatia K.G. Airplane Aeroelasticity: Practice and Potential. *Journal of Aircraft*, 40(6):1010–1018, 2003.

[34] Yurkovich R. Status of Unsteady Aerodynamic Prediction for Flutter of High-Performance Aircraft. *Journal of Aircraft*, 40(5):832–842, 2003.

[35] Dowel E.H., Thomas J.P., Hall K.C., and Denegri Jr. C.M. Theoretical Predictions of F-16 Fighter Limit Cycle Oscillations for Flight Flutter Testing. *Journal of Aircraft*, 46(5):1667–1672, 2009.

[36] Sobester A. and Keane A.J. Multidisciplinary design optimisation of UAV airframes. In *47th AIAA/ASME/ASCE/AHS/ASC Structures, Structural Dynamics and Materials Conference*, number 47, page 13, Newport, Rhode Island, May 2006. AIAA.

[37] MSC Software. *Aeroelastic Analysis User's Guide*, 2004.

[38] Farhat C., Geuzaine P., and Brown G. Application of a Three-Field Nonlinear Fluid-Structure Formulation to the Prediction of the Aeroelastic Parameters of an F-16 Fighter. *Computers and Fluids*, 32:3–29, 2003.

[39] Badcock K.J., Rampurawala A.M., and Richards B.E. Intergrid Transformation for Aircraft Aeroelastic Simulations. *AIAA Journal*, 42(9):1936–1939, 2004.

[40] Badcock K. J., Woodgate M. A., and Richards B. E. Direct Aeroelastic Bifurcation Analysis of a Symmetric Wing Based on the Euler Equations. *Journal of Aircraft*, 42(3):731–737, 2005.

[41] Badcock K.J. and Woodgate M.A. Prediction of Bifurcation Onset of Large Order Aeroelastic Models. In *AIAA-2008-1820 in the proceedings of the 49th Structural Dynamics and Materials Conference, AIAA, Schaumberg, Illinois*, 2008.

[42] Shang J.S. Computational Fluid Dynamics Application to Aerospace Science. *The Aeronautical Journal*, 113(1148):619–632, 2009.

[43] Batina J.T. Unsteady Euler Airfoil Solutions Using Unstructured Dynamic Meshes. *AIAA Journal*, 28(8):1381–1388, August 1990.

[44] Farhat C., Degand C., Koobus B., and Lesoinne M. Torsional Springs for Two-Dimensional Dynamic Unstructured Fluid Meshes. *Computational Methods in Applied Mechanics and Engineering*, 163:231–245, 1998.

[45] Blom F.J. Considerations on the Spring Analogy. *International Journal for Numerical Methods in Fluids*, 32:647–668, 2000.

[46] Dubuc L., Cantariti F., Woodgate M., Gribben B., Badcock K.J., and Richards B.E. A Grid Deformation Technique for Unsteady Flow Computations. *International Journal for Numerical Methods in Fluids*, 38:285–311, 2000.

[47] Chen P.C. and Jadic I. Interfacing of Fluid and Structural Models via Innovative Structural Boundary Element Method. *AIAA Journal*, 36(2):282–287, 1998.

[48] Liu X., Qin N., and Xia H. Fast Dynamic Grid Deformation based on Delaunay Graph Mapping. *Journal of Computational Physics*, 211:405–423, 2006.

[49] de Boer A., van der Schoot M.S., and Bijl H. Mesh Deformation based on Radial Basis Function Interpolation. *Computers and Structures*, 85:784–795, 2007.

[50] Rendall T.C.S. and Allen C.B. Parallel Efficient Mesh Motion using Radial Basis Functions with Application to Multi-Bladed Rotors. *International Journal for Numerical Methods in Engineering*, 81:89–105, 2009.

[51] Farhat C. and Lesoinne M. Two Efficient Staggered Algorithms for the Serial and Parallel Solution of Three-Dimensional Nonlinear Transient Aeroelastic Problems. *Computer Methods in Applied Mechanics and Engineering*, 182:499–515, 2000.

[52] Harder R.L. and Desmarais R.N. Interpolation Using Surface Splines. *Engineering Notes*, pages 189–191, February 1972.

[53] Menter F.R. Two-Equation Eddy-Viscosity Turbulence Models for Engineering Applications. *AIAA Journal*, 32(8):1598–1605, 1994.

[54] Menter F.R., Kuntz M., and Langtry R. Ten Years of Industrial Experience with the SST Turbulence Model. In Hanjalić K., Nagano Y., and Tummers M., editors, *Turbulence, Heat and Mass Transfer 4*. Begell House Inc., 2003.

[55] Badcock K.J., Richards B.E., and Woodgate M.A. Elements of Computational Fluid Dynamics on Block Structured Grids using Implicit Solvers. *Progress in Aerospace Sciences*, 36:351–392, 2000.

[56] Bekas C. and Saad Y. Computation of Smallest Eigenvalues using Spectral Schur Complements. *SIAM Journal on Scientific Computing*, 27(2):458–481, 2005.

[57] Guruswamy G.P. and Byun C. Direct Coupling of Euler Flow Equations with Plate Finite Element Structures. *AIAA Journal*, 33(2):375–377, 1995.

[58] Felker F.F. Direct Solution of Two-Dimensional Navier-Stokes Equations for Static Aeroelasticity Problems. *AIAA Journal*, 31(1):148–153, 1993.

[59] Hübner B., Walhorn E., and Dinkler D. A Monolithic Approach to Fluid-Structure Interaction using Space-Time Finite Elements. *Computer Methods in Applied Mechanics and Engineering*, 193:2087–2104, 2004.

[60] Smith M.J., Hodges D.H., and Cesnik C.E.S. An Evaluation Of Computational Algorithms to Interface Between CFD and CSD Methodologies. Technical Report WL-TR-96-3055, U.S. Air Force Research Lab., November 1995.

[61] Kamakoti R. and Shyy W. Fluid-Structure Interaction for Aeroelastic Applications. *Progress in Aerospace Science*, 40(8):535–558, 2004.

[62] Sadeghi M., Lui F., Lai K.L., and Tsai H.M. Application of Three-Dimensional Interfaces for Data Transfer in Aeroelastic Computations. In *22nd Applied Aerodynamics Conference and Exhibit*, number 2004-5376, August 2004.

[63] Done G.T.S. Interpolation of Mode Shapes: A Matrix Scheme using Two-Way Spline Curves. *Aeronautical Quarterly*, XVI:333–349, 1965.

[64] McNeal. NATRAN. Website. http://www.mscsoftware.com/products/msc_nastran.cfm?Q=131&Z

[65] ZONA Technology Inc. ASTROS. Website. http://www.zonatech.com/ASTROS.htm.

[66] Hardy R.L. Multiquadric Equations of Topography and Other Irregular Surfaces. *Journal of Geophysical Research*, 76(8):1905–1915, March 1971.

[67] Duchon J. Splines Minimising Rotational-Invariant Semi-Norms in Sobolev Spaces. In Schempp W. and Zeller K., editors, *Constructive Theory of Functions of Several Variables, Oberwolfach, 1976*, pages 85–100. Springer-Verlag, 1977.

[68] Franke R. Scattered Data Interpolation: Tests of Some Methods. *Mathematics of Computation*, 38(157), 1982.

[69] Murti V. and Valliappan S. Numerical Inverse Isoparametric Mapping in Remeshing and Nodal Quantity Contouring. *Computers and Structures*, 22(6):1011–1021, 1986.

[70] Appa K. Finite-Surface Spline. *Journal of Aircraft*, 26(5):495–496, 1989.

[71] Kansa E.J. Multiquadrics - A Scattered Data Approximation Scheme with Applications to Computational Fluid-Dynamics - I: Surface Approximations and Partial Derivative Estimates. *Computers and Mathematics with Applications*, 19(8/9):127–145, 1990.

[72] Pidaparti R.M.V. Structural and Aerodynamic Data Transformation Using Inverse Isoparametric Mapping. *Journal of Aircraft*, 29(3):507–509, 1992.

[73] Samareh J.A. Use of CAD Geometry in MDO. *AIAA Paper AIAA-96-3991*, 1996.

[74] Cebral J.R. and Löhner R. Conservative Load Projection and Tracking for Fluid-Structure Problems. *AIAA Journal*, 35(4):687–692, April 1997.

[75] Beckert A. and Wendland H. Multivariate Interpolation for Fluid-Structure-Interaction Problems using Radial Basis Functions. *Aerospace Science and Technology*, 5:125–131, 2001.

[76] Ahrem R., Beckert A., and Wendland H. A Meshless Spatial Coupling Scheme for Large-Scale Fluid-Structure-Interaction Problems. *Computer Modelling in Engineering and Sciences*, 12:121–136, 2006.

[77] Ahrem R., Beckert A., and Wendland H. Recovering Rotations in Aeroelasticity. *Journal of Fluids and Structures*, 23:874–884, 2007.

[78] Rendall T.C.S. and Allen C.B. Improved Radial Basis Function Fluid-Structure Coupling via Efficient Localised Implementation. *International Journal for Numerical Methods in Engineering*, 78:1188–1208, 2009.

[79] Goura G.S.L. *Time Marching Analysis of Flutter using Computational Fluid Dynamics*. PhD thesis, University of Glasgow, 2001.

[80] Burnett D.S. *Finite Element Analysis from Concepts to Applications*. Addison-Wesley Publishing Company, 1987.

[81] Smith M.J., Hodges D.H., and Cesnik C.E.S. Evaluation of Computational Algorithms Suitable for Fluid-Structure Interactions. *Journal of Aircraft*, 37(2):282–294, 2000.

[82] Samareh J.A. Aeroelastic Deflection of NURBS Geometry. In *6th International Conference on Numerical Grid Generation in Computational Field Simulation*, July 1998.

[83] Wendland H. Fast Evaluation of Radial Basis Functions: Method Based on Partition of Unity. *Approximation Theory X: Wavelets, Splines and Applications*, pages 473–483, 2002.

[84] Beran P.S., Khot N.S., Eastep F.E., Snyder R.D., and Zweber J.V. Numerical Analysis of Store-Induced Limit-Cycle Oscillation. *Journal of Aircraft*, 41(6):1315–1326, 2004.

[85] Girodroux-Lavigne P., Grisval J.P., Guillemot S., Henshaw M., Karlsson A., Selmin V., Smith J., Teupootahiti E., and Winzell B. Comparison of Static and Dynamic Fluid-Structure Interaction Solutions in the Case of a Highly Flexible Modern Transport Aircraft Wing. *Aerospace Science and Technology*, 7:121–133, 2003.

[86] Lee B.H.K. and Ohman L.H. Unsteady Pressure and Forces during Transonic Buffeting of a Supercritical Airfoil. *Journal of Aircraft*, 21(6):439–441, 1984.

[87] Lee B.H.K., Ellis F.A., and Bureau J. Investigation of the Buffet Characteristics of Two Supercritical Airfoils. *Journal of Aircraft*, 26(8):731–736, 1989.

[88] Lee B.H.K. Investigation of Flow Separation on a Supercritical Airfoil. *Journal of Aircraft*, 26(11):1032–1037, 1989.

[89] Lee B.H.K. Transonic Buffet on a Supercritical Aerofoil. *Aeronautical Journal*, pages 143–152, May 1990.

[90] Huang R.F. and Lee H.W. Turbulence Effect on Frequency Characteristics of Unsteady Motions in Wake of Wing. *AIAA Journal*, 38(1):87–94, 2000.

[91] Xiao Q., Tsai H.M., and Liu F. A Numerical Study of Transonic Buffet on a Supercritical Airfoil. In *42nd AIAA Aerospace Sciences Meeting and Exhibit, 5-8 January 2004, Reno, Nevada, AIAA 2004-1056*.

[92] Lee B.H.K. and Tang F.C. Characteristics of the Surface Pressures on a F/A-18 Vertical Fin due to Buffet. *Journal of Aircraft*, 31(1):228–235, 1994.

[93] Lee B.H.K. Self-Sustained Shock Oscillations on Airfoil at Transonic Speeds. *Progress in Aerospace Sciences*, 37:147–196, 2001.

[94] Levy Jr. L.L. Experimental and Computational Steady and Unsteady Transonic Flows about a Thick Airfoil. *AIAA Journal*, 16(6):564–572, 1978.

[95] McDevitt J.B. Supercritical Flow about a Thick Circular-Arc Airfoil. Technical Report 78549, NASA, 1979.

[96] Rumsey C.L., Sanetrik M.D., Biedrom R.T., Melson N.D., and Parlette E.B. Efficient and Accuracy of Time-Accurate Turbulent Navier-Stokes Computations. *Computations and Fluids*, 25(2):217–236, 1996.

[97] Prananta B.B. Two-Dimensional Transonic Aeroelastic Analysis using Thin-Layer Navier-Stokes Method. *Journal of Fluids and Structures*, 12:665–676, 1998.

[98] Raghunathan S., Gillan M.A., Cooper R.K., Mitchell R.D., and Cole J.S. Shock Oscillations on Biconvex Aerofoils. *Aerospace Science and Technology*, 1:1–9, 1999.

[99] Chen L.W., Xu C.Y, and Lu X.Y. Numerical Investigation of the Compressible Flow Past an Aerofoil. *Journal of Fluid Mechanics*, 643:97–126, 2010.

[100] Jacquin L., Molton P., Deck S., Maury B., and Soulevant D. Experimental Study of Shock Oscillation over a Transonic Supercritical Profile. *AIAA Journal*, 47(9):1985–1994, September 2009.

[101] Deck S. Zonal-Detached-Eddy Simulation of the Flow Around a High-Lift Configuration. *AIAA Journal*, 43(11):2372–2384, 2005.

[102] Garnier E. and Deck S. Large-Eddy Simulation of Transonic Buffet over a Supercritical Airfoil. In *Direct and Large-Eddy Simulation VII*, volume 13 of *ERCOFTAC*, pages 549–554. Springer Netherlands.

[103] Raghunathan S., Mitchell R.D., and Gillan M.A. Transonic shock oscillations on naca 0012 aerofoil. *Shock Waves*, 8:191–202, 1998.

[104] Iovnovich M. and Raveh D.E. Reynolds-Averaged Navier-Stokes Study of the Shock-Buffet Instability Mechanism. In *52nd AIAA/ASME/ASCE/AHS/ASC Structures, Structural Dynamics and Materials Conference*, number AIAA 2011-2078, 2011.

[105] Singh J.P. Estimation of Shock-Induced Buffet Onset. *Acta Mechanica*, 151:245–253, 2001.

[106] Murrow H.N. and Eckstrom C.V. Drones for Aerodynamic and Structural Testing (DAST) - A Status Report. *Journal of Aircraft*, 16(8):521–526, 1979.

[107] Cole S.R. and Rivera Jr. J.A. The New Heavy Gas Testing Capability in the NASA Langley Transonic Dynamics Tunnel. Technical Report NASA-TM-112702, NASA Langley Research Center, 1997.

[108] Seidel D.A., Sandford M.C., and Eckstrom C.V. Measured Unsteady Transonic Aerodynamic Characteristics of an Elastic Supercritical Wing. *Journal of Aircraft*, 24(4):225–230, April 1987.

[109] Eckstrom C.V., Seidel D.A., and Sandford M.C. Unsteady Pressure and Structural Response Measurements on an Elastic Supercritical Wing. *Journal of Aircraft*, 27(1):75–80, 1990.

[110] Farhangnia M., Guruswamy G., and Biringen S., editors. *Transonic-Buffet Associated Aeroelasticity of a Supercritical Wing*, number AIAA 96-0286 in 34th Aerospace Sciences Meeting and Exhibit, Reno, NV, January 1996.

[111] Byrdsong T.A., Adams R.R., and Sandford M.C. Close-Range Photogrammetric Measurement of Static Deflections for an Aeroelastic Supercritical Wing. Technical Report NASA TM 4194, NASA, Langley Research Center, Hampton, Virginia, 1990.

[112] Byrdsong T.A., Adams R.R., and Sandford M.C. Close-Range Photogrammetric Measurement of Static Deflections for an Aeroelastic Supercritical Wing. Technical Report Supplement to NASA TM 4194, NASA, Langley Research Center, Hampton, Virginia, 1990.

Appendix A

Infinite Plate Spline

This appendix will provide the derivation of the transformation matrix for infinite plate splines. The deflections normal to the plate surface due to N point forces F_i at given locations (x_i, y_i) on the plate can be written as

$$dz(x,y) = a_0 + a_1 x + a_2 y + \sum_{i=1}^{N} F_i r_i^2 \ln r_i^2 \tag{A.1}$$

where $r_i^2 = x_i^2 + y_i^2$. The unknowns, a_k and F_i are obtained from the equilibrium conditions

$$\sum_{i=1}^{N} F_i = \sum_{i=1}^{N} x_i F_i = \sum_{i=1}^{N} y_i F_i = 0 \tag{A.2}$$

and from the given deflections at the N nodes

$$dz_j = a_0 + a_1 x_j + a_2 y_j + \sum_{i=1}^{N} F_i r_{ij}^2 \ln r_{ij}^2 \tag{A.3}$$

where $r_{ij}^2 = (x_i - x_j)^2 + (y_i - y_j)^2$. By applying Equations A.2 and A.3 to both the structural and aerodynamic points the following equations are obtained, expressed in matrix form as

$$\mathbf{dx}_s = R_s \mathbf{a} + Z_s \mathbf{F}_s \tag{A.4}$$

$$\mathbf{dx}_a = R_a \mathbf{a} + Z_{as} \mathbf{F}_s \tag{A.5}$$

and Equation A.4 is subject to

$$R_s^T \mathbf{F}_s = 0 \tag{A.6}$$

where

$$R_s = \begin{bmatrix} 1 & x_{s_1} & y_{s_1} \\ 1 & x_{s_2} & y_{s_2} \\ \vdots & \vdots & \vdots \\ 1 & x_{s_N} & y_{s_N} \end{bmatrix}$$

and

$$R_a = \begin{bmatrix} 1 & x_{a_1} & y_{a_1} \\ 1 & x_{a_2} & y_{a_2} \\ \vdots & \vdots & \vdots \\ 1 & x_{a_N} & y_{a_N} \end{bmatrix}$$

and where Z_s and Z_{as} contain the elements

$$Z_{s_{ij}} = \left[\left(x_{s_i} - x_{s_j}\right)^2 + \left(y_{s_i} - y_{s_j}\right)^2\right] \ln \left[\left(x_{s_i} - x_{s_j}\right)^2 + \left(y_{s_i} - y_{s_j}\right)^2\right]$$

$$Z_{as_{ij}} = \left[\left(x_{a_i} - x_{s_j}\right)^2 + \left(y_{a_i} - y_{s_j}\right)^2\right] \ln \left[\left(x_{a_i} - x_{s_j}\right)^2 + \left(y_{a_i} - y_{s_j}\right)^2\right]$$

which are effectively matrices of the basis function $(r_{ij}^2 \ln r_{ij}^2)$. Given that

$$\mathbf{dx}_a = T\mathbf{dx}_s \tag{A.7}$$

where T is the transformation matrix and from the principle of virtual work

$$\mathbf{F}_s = T^T\mathbf{F}_a \tag{A.8}$$

The transformation matrix T can be derived as

$$T = \left[R_a Y_s^{-1} R_s^T + Z_{as}\left[I - Y_s^{-1} R_s^T Z_s^{-1} R_s\right]\right] Z_s^{-1} \tag{A.9}$$

where $Y_s = R_s^T Z_s^{-1} R_s$ and I is an identity matrix.

Appendix B

Inverse Isoparametric Mapping

This appendix will provide the derivation of the transformation matrix for Inverse Isoparametric Mapping. The same shape functions N_i are used for both the aerodynamic grid points and the structural deformation

$$x_a = \sum_{i=1}^{n} N_i(\xi, \eta) x^e_{s_i} \tag{B.1}$$

$$y_a = \sum_{i=1}^{n} N_i(\xi, \eta) y^e_{s_i} \tag{B.2}$$

where n is the number of nodes for the element. The element is assumed to lie in the $x - y$ plane and the superscript e indicates the structural node is a member of that element. The shape function for a quadrilateral element[80] is given by

$$\begin{gathered} N_1(\xi, \eta) = (1 - \xi)(1 - \eta)/4 \\ N_2(\xi, \eta) = (1 + \xi)(1 - \eta)/4 \\ N_3(\xi, \eta) = (1 + \xi)(1 + \eta)/4 \\ N_4(\xi, \eta) = (1 - \xi)(1 + \eta)/4 \\ \xi, \eta \in [-1, 1] \end{gathered} \tag{B.3}$$

The implementation shown here is based upon the implementation by Smith[60]. First Equation B.1 is expanded and using Equation B.3 one can get

$$x_a = a_{x_1}\xi\eta + a_{x_2}\xi + a_{x_3}\eta + a_{x_4} \tag{B.4}$$

where

$$\begin{aligned} a_{x_1} &= (x^e_{s_1} - x^e_{s_2} + x^e_{s_3} - x^e_{s_4})/4 \\ a_{x_2} &= (-x^e_{s_1} + x^e_{s_2} + x^e_{s_3} - x^e_{s_4})/4 \\ a_{x_3} &= (-x^e_{s_1} - x^e_{s_2} + x^e_{s_3} + x^e_{s_4})/4 \\ a_{x_4} &= (x^e_{s_1} + x^e_{s_2} + x^e_{s_3} + x^e_{s_4})/4 \end{aligned} \tag{B.5}$$

The same is true for y

$$y_a = a_{y_1}\xi\eta + a_{y_2}\xi + a_{y_3}\eta + a_{y_4} \tag{B.6}$$

where

$$\begin{aligned} a_{y_1} &= (y^e_{s_1} - y^e_{s_2} + y^e_{s_3} - y^e_{s_4})/4 \\ a_{y_2} &= (-y^e_{s_1} + y^e_{s_2} + y^e_{s_3} - y^e_{s_4})/4 \\ a_{y_3} &= (-y^e_{s_1} - y^e_{s_2} + y^e_{s_3} + y^e_{s_4})/4 \\ a_{y_4} &= (y^e_{s_1} + y^e_{s_2} + y^e_{s_3} + y^e_{s_4})/4 \end{aligned} \tag{B.7}$$

Rearranging Equation B.6 for η

$$\eta = \frac{y_a - a_{y_4} - a_{y_2}\xi}{a_{y_1}\xi + a_{y_3}} \tag{B.8}$$

This can be substituted into Equation B.4 and rearranged into the form

$$A\xi^2 + B\xi + C = 0 \tag{B.9}$$

where

$$\begin{aligned} A &= a_{x_2}a_{y_1} - a_{x_1}a_{y_2} \\ B &= a_{y_1}(a_{x_4} - x_a) + a_{x_1}(y_a - a_{y_4}) + a_{x_2}a_{y_3} - a_{x_3}a_{y_2} \\ C &= a_{y_3}(a_{x_4} - x_a) + a_{x_3}(y_a - a_{y_4}) \end{aligned} \tag{B.10}$$

If $a_{y_1}\xi + a_{y_3} = 0$ then use

$$\eta = \frac{x_a - a_{x_4} - a_{x_2}\xi}{a_{x_1}\xi + a_{x_3}} \tag{B.11}$$

to substitute into Equation B.6, this leads to

$$\begin{aligned} A &= a_{y_2}a_{x_1} - a_{y_1}a_{x_2} \\ B &= a_{x_1}(a_{y_4} - y_a) + a_{y_1}(x_a - a_{x_4}) + a_{y_2}a_{x_3} - a_{y_3}a_{x_2} \\ C &= a_{x_3}(a_{y_4} - y_a) + a_{y_3}(x_a - a_{x_4}) \end{aligned} \tag{B.12}$$

Equation B.9 can be solved as a normal quadratic, there will be one solution of the equation inside the bounds $[-1, 1]$. Then η can be solved for using either Equation B.8 or B.11. Once the local coordinates for the aerodynamic grid points have been calculated the shape functions can be calculated using Equation B.3. Then the displacements can be calculated using

$$dx_a = \sum_{i=1}^{n} N_i(\xi, \eta) dx^e_{s_i} \tag{B.13}$$

This can be expanded assuming $n = 4$

$$dx_a = N_1 dx^e_{s_1} + N_2 dx^e_{s_2} + N_3 dx^e_{s_3} + N_4 dx^e_{s_4} \tag{B.14}$$

and then written in matrix format

$$\mathbf{dx}_a = T\mathbf{dx}^e_s \tag{B.15}$$

where T is the local transformation matrix. This then allows the forces to be calculated using

$$\mathbf{F}^e_s = T^T\mathbf{F}_a \tag{B.16}$$

from the principle of virtual work and therefore satisfies conservation of energy.

Appendix C

Radial Basis Functions

This appendix will provide the derivation of the transformation matrix for radial basis functions. The radial basis function interpolant [2] has the form

$$s(\mathbf{x}) = \sum_{i=1}^{N} \alpha_i \phi(\|\mathbf{x} - \mathbf{x}_i\|) + p(\mathbf{x}) \tag{C.1}$$

where $s(\mathbf{x})$ is the function to be evaluated at $\mathbf{x}$, ϕ is the basis function, the index i identifies the centres for the RBF and $\mathbf{x}_i$ is the location of that centre. The linear polynomial $p(\mathbf{x})$ is used to ensure that translations and rotations are recovered. The coefficients α_i are found by requiring the exact recovery of the structural node positions. The polynomial in the x-direction is given by

$$p_x(\mathbf{x}) = \gamma_{x0} + \gamma_{xx}x + \gamma_{xy}y + \gamma_{xz}z \tag{C.2}$$

When the polynomials are included in the system, the additional requirement is also required

$$\sum_{i=1}^{N} \alpha_i q(\mathbf{x}) = 0 \tag{C.3}$$

for all polynomials $q(\mathbf{x})$ with degree less than or equal to $p(\mathbf{x})$. For ease of computation the exact recovery of centres gives using up to linear polynomial terms

$$\mathbf{X}_s = C_{ss}\mathbf{a}_x \tag{C.4}$$

$$\mathbf{Y}_s = C_{ss}\mathbf{a}_y \tag{C.5}$$

$$\mathbf{Z}_s = C_{ss}\mathbf{a}_z \tag{C.6}$$

where

$$\mathbf{X}_s = \begin{pmatrix} 0 \\ 0 \\ 0 \\ 0 \\ \mathbf{x}_s \end{pmatrix}, \mathbf{x}_s = \begin{pmatrix} x_{s_1} \\ \vdots \\ x_{s_{n_s}} \end{pmatrix}, \mathbf{a}_x = \begin{pmatrix} \gamma_{x0} \\ \gamma_{xx} \\ \gamma_{xy} \\ \gamma_{xz} \\ \alpha_{xs_1} \\ \vdots \\ \alpha_{xs_{n_s}} \end{pmatrix} \tag{C.7}$$

There are analogous definitions for $\mathbf{Y}_s$, $\mathbf{Z}_s$, $\mathbf{a}_y$ and $\mathbf{a}_z$.

$$C_{ss} = \begin{bmatrix} 0 & 0 & 0 & 0 & 1 & 1 & \dots & 1 \\ 0 & 0 & 0 & 0 & x_{s_1} & x_{s_2} & \dots & x_{s_{n_s}} \\ 0 & 0 & 0 & 0 & y_{s_1} & y_{s_2} & \dots & y_{s_{n_s}} \\ 0 & 0 & 0 & 0 & z_{s_1} & z_{s_2} & \dots & z_{s_{n_s}} \\ 1 & x_{s_1} & y_{s_1} & z_{s_1} & \phi_{s_1 s_1} & \phi_{s_1 s_2} & \dots & \phi_{s_1 s_{n_s}} \\ \vdots & \vdots & \vdots & \vdots & \vdots & \vdots & \ddots & \vdots \\ 1 & x_{s_{n_s}} & y_{s_{n_s}} & z_{s_{n_s}} & \phi_{s_{n_s} s_1} & \phi_{s_{n_s} s_2} & \dots & \phi_{s_{n_s} s_{n_s}} \end{bmatrix} \tag{C.8}$$

where $\phi_{s_1 s_2} = \phi\left(\|\mathbf{x}_{s_1} - \mathbf{x}_{s_2}\|\right)$ and s indicating a structural node. An analogous matrix C_{aa} where a indicates an aerodynamic node. To locate the aerodynamic surface points the following matrix must be formed

$$A_{as} = \begin{bmatrix} 1 & x_{a_1} & y_{a_1} & z_{a_1} & \phi_{a_1 s_1} & \phi_{a_1 s_2} & \dots & \phi_{a_1 s_{n_s}} \\ \vdots & \vdots & \vdots & \vdots & \vdots & \vdots & \ddots & \vdots \\ 1 & x_{a_{n_a}} & y_{a_{n_a}} & z_{a_{n_a}} & \phi_{a_{n_a} s_1} & \phi_{a_{n_a} s_2} & \dots & \phi_{a_{n_a} s_{n_s}} \end{bmatrix} \tag{C.9}$$

The positions of the aerodynamic surface points given by the the vectors $\mathbf{x}_a$, $\mathbf{y}_a$ and $\mathbf{z}_a$ analogous to $\mathbf{x}_s$ in Equation C.7 is given by

$$\begin{pmatrix} \mathbf{x}_a \\ \mathbf{y}_a \\ \mathbf{z}_a \end{pmatrix} = \begin{bmatrix} T & 0 & 0 \\ 0 & T & 0 \\ 0 & 0 & T \end{bmatrix} = \begin{pmatrix} \mathbf{X}_s \\ \mathbf{Y}_s \\ \mathbf{Z}_s \end{pmatrix} \tag{C.10}$$

where $T = A_{as} C_{ss}^{-1}$. Since the matrix C_{ss} has a zero block, the matrix can be subdivided as shown below

$$C_{ss} = \begin{bmatrix} 0 & P \\ P^T & M \end{bmatrix} \tag{C.11}$$

The vectors $\mathbf{a}_x$, $\mathbf{a}_y$ and $\mathbf{a}_z$ are split into the parts which multiply the RBF (superscript RBF) and polynomial (superscript PLY)terms,

$$\mathbf{a}_x^{PLY} = M_p P M^{-1} \mathbf{x}_s \tag{C.12}$$

$$\mathbf{a}_x^{RBF} = \left(M^{-1} - M^{-1} P^T M_p P M^{-1}\right) \mathbf{x}_s \tag{C.13}$$

where $M_p = \left(P M^{-1} P^T\right)^{-1}$. Forming the transformation matrix is now straight forward

$$T = A_{as} \begin{bmatrix} M_p P M^{-1} \\ M^{-1} - M^{-1} P^T M_p P M^{-1} \end{bmatrix} \tag{C.14}$$